

# Plasmon-enhanced nonlinear optics for applications in sensing and biology

A thesis presented

by

Eric David Diebold

to

The School of Engineering and Applied Sciences

in partial fulfillment of the requirements

for the degree of

Doctor of Philosophy

in the subject of

Applied Physics

Harvard University

Cambridge, Massachusetts

May 2010

©2010 by Eric David Diebold

All rights reserved.

**Plasmon-enhanced nonlinear optics for applications in  
sensing and biology**

Eric Mazur

Eric David Diebold

ABSTRACT

In this thesis, we present the results of three experiments that combine techniques from the fields of ultrafast nonlinear optics and plasmonics, with the aim of developing tools for improved surface-enhanced Raman spectroscopy and biological cell transfection. We first describe the use of femtosecond laser pulses to generate large areas of a nanostructured silicon surface which is used as a new type of substrate for surface-enhanced Raman scattering (SERS). We perform spectroscopic characterization of this substrate and find its Raman cross-section enhancement factor to be on the order of  $10^7$ . This large, spatially-uniform, and reproducible enhancement factor is nearly constant across the near-infrared spectral region. In a second experiment, we develop a technique to spatially isolate the “hot spots” on SERS substrates. This technique leverages the plasmonic near field enhancement of metallic nanostructures to preferentially expose a commercial photoresist using femtosecond laser pulses. By isolating the hot spots, analyte molecules adsorb only to the regions of largest electromagnetic enhancement. Compared to an unprocessed substrate covered with a sub-monolayer of benzenethiol molecules, a processed substrate shows a 27-fold improvement in its average Raman cross-section enhancement factor. Finally, we present a proof-of-principle experiment which demonstrates high-throughput ultrafast laser transfection of biological cells using large-area plasmonic substrates. Utilizing the field localization properties of a substrate fabricated using photolithography, wet

etching, and template stripping, we demonstrate the introduction of silence RNA (siRNA) molecules into cells with an efficiency of approximately 50% after exposure to femtosecond laser pulses.

# Table of Contents

<i>Abstract</i>	<i>iii</i>
<i>Table of Contents</i>	<i>v</i>
<i>List of Figures</i>	<i>viii</i>
<i>Acknowledgements</i>	<i>x</i>
<i>Citations to Published Work</i>	<i>xvi</i>
<b>1 Introduction</b>	<b>1</b>
1.1 Organization of the thesis . . . . .	1
1.2 Scientific introduction . . . . .	2
<b>2 Theoretical background</b>	<b>6</b>
2.1 Introduction . . . . .	6
2.2 Localized surface plasmon resonance: fields scattered by a subwavelength sphere . . . . .	7
2.2.1 Dielectric function result from the Drude model of electrons in a metal . . . . .	11
2.3 Raman scattering . . . . .	13
2.4 Surface-enhanced Raman scattering . . . . .	20
2.5 Multiphoton transitions . . . . .	24
<b>3 Femtosecond laser-nanostructured SERS substrates</b>	<b>29</b>
3.1 Abstract . . . . .	29
3.2 Introduction . . . . .	30
3.3 Experimental details . . . . .	32
3.3.1 SERS substrate fabrication . . . . .	32
3.3.2 Raman spectroscopy measurements . . . . .	36
3.4 Results . . . . .	38

---

3.5	Discussion . . . . .	43
3.5.1	SERS substrate morphology . . . . .	43
3.5.2	Calculation of the SERS enhancement factor . . . . .	47
3.5.3	Silver deposition . . . . .	52
3.5.4	Substrate uniformity . . . . .	53
3.5.5	Excitation profiling . . . . .	54
3.5.6	Substrate temporal stability . . . . .	55
3.6	Conclusion . . . . .	56
3.7	Acknowledgements . . . . .	57
<b>4</b>	<b>Isolating SERS hot spots using multiphoton lithography</b>	<b>58</b>
4.1	Abstract . . . . .	58
4.2	Introduction . . . . .	59
4.3	Experimental . . . . .	60
4.4	Results . . . . .	61
4.5	Discussion . . . . .	62
4.6	Conclusion . . . . .	68
4.7	Acknowledgements . . . . .	69
<b>5</b>	<b>Plasmon-enhanced ultrafast laser cell transfection</b>	<b>70</b>
5.1	Abstract . . . . .	70
5.2	Introduction . . . . .	71
5.3	Experimental . . . . .	75
5.3.1	Fabrication of plasmonic substrates for cell transfection . . . . .	75
5.3.2	Femtosecond laser system . . . . .	78
5.3.3	Characterization of plasmonic enhancement of femtosecond laser pulses . . . . .	79
5.3.4	Cell culture . . . . .	82
5.3.5	Electron microscopy of cells . . . . .	83
5.3.6	Laser parameter optimization . . . . .	83
5.3.7	Plasmon-enhanced laser cell transfection using siRNA . . . . .	85
5.4	Results . . . . .	86
5.4.1	Laser parameter optimization . . . . .	86
5.4.2	Plasmon-enhanced laser cell transfection using siRNA . . . . .	89
5.5	Discussion . . . . .	93
5.5.1	Laser parameter optimization . . . . .	93
5.5.2	Plasmon-enhanced laser cell transfection using siRNA . . . . .	95
5.6	Conclusion . . . . .	98
5.7	Acknowledgements . . . . .	99
<b>6</b>	<b>Conclusions and outlook</b>	<b>101</b>

---

<b>A Soft lithography “replication” of SERS substrates</b>	<b>107</b>
<b>B Custom-built tunable CW titanium:sapphire laser system</b>	<b>111</b>
<b>References</b>	<b>114</b>

# List of Figures

2.1	Subwavelength sphere irradiated by a plane wave at frequency $\omega_0$ . . .	8
2.2	Sphere in a static, uniform electric field, illustrating the result of the quasi-static approximation. . . . .	9
2.3	Example of a molecular vibrational mode which is not Raman active.	18
2.4	Typical Raman spectrum taken from a $\beta$ -barium borate crystal . . .	20
3.1	Schematic of the laser nano-structuring setup used to fabricate the silicon-based SERS substrates . . . . .	33
3.2	Photograph of 1 cm <sup>2</sup> sized areas of silicon, nanostructured in an aqueous environment, using 400-nm femtosecond laser pulses. . . . .	34
3.3	Scanning electron and helium microscope images of SERS substrate .	36
3.4	SERS and normal Raman spectra of benzenethiol . . . . .	40
3.5	Silver deposition dependence of the SERS enhancement factor . . . .	41
3.6	Raman map and intensity histogram from SERS substrate . . . . .	42
3.7	Excitation profile of mercaptobenzoic acid on laser-nanostructured SERS substrate . . . . .	43
3.8	Cartoon schematic of the surface area model . . . . .	48
3.9	Experimental determination of a Gaussian beam waist . . . . .	51
3.10	Typical axial collection efficiency function of a confocal Raman microscope . . . . .	52
4.1	Helium ion microscope image and schematic of the hot spot isolation process . . . . .	61
4.2	SERS signal as a function of femtosecond laser exposure fluence . . .	63
4.3	Comparison of hot spot isolation-processed substrate with unprocessed substrate . . . . .	64
4.4	Multiphoton-induced luminescence spectrum and resist absorption spectrum . . . . .	65
4.5	CW and femtosecond laser spectra . . . . .	66
4.6	Hot spot isolation resist exposure as a function of exposure laser fluence	67

---

5.1	SEM of typical pyramidal pits formed after KOH etching . . . . .	76
5.2	Schematic of the template stripping process used to create the inverse structure of the pyramidal pits. . . . .	77
5.3	SEM of polymeric pyramids coated with 25 nm of gold . . . . .	78
5.4	Layout of the laser system used to expose cells to plasmon-enhanced femtosecond laser pulses . . . . .	80
5.5	Two-photon polymerization of photoinitiator-monomer resin on polymer pyramidal substrate coated with 20 nm of gold. The dark polymer covering the tips of the pyramids is indicative of the spatial distribution of the square of the optical field intensity. . . . .	82
5.6	Example scanning electron microscope image of human breast carcinoma cells seeded onto a gold-coated pyramidal substrate with 10 $\mu\text{m}$ pitch. Cell adhesion, spreading, and proliferation on the substrate is indicative of its bio-compatibility. . . . .	84
5.7	Optical microscope images of cells stained with FM1-43 . . . . .	85
5.8	Human thymus epithelial cells in FM1-43 after exposure to plasmon-enhanced femtosecond laser pulses . . . . .	88
5.9	Fluorescence and brightfield image of cells producing GFP after exposure to plasmon-enhanced femtosecond laser pulses . . . . .	90
5.10	Fluorescence and brightfield image of defective region of a seeded substrate exposed to plasmon-enhanced femtosecond laser pulses . . . . .	91
5.11	Fluorescence image of the same defective region of the substrate shown in Figure 5.10, taken 48 hours after laser exposure. . . . .	92
5.12	Fluorescence image and 2-color histogram of cells transfected with siRNA . . . . .	94
A.1	SERS spectrum taken from a negative mold of a laser-nanostructured silicon wafer, coated with 80 nm of silver . . . . .	109
B.1	Cavity layout for the tunable CW titanium:sapphire laser . . . . .	112

# Acknowledgements

Growing up as the son of a chemistry professor, I had many opportunities to meet my father's graduate students. Up until my senior year in college, I was determined to never become a graduate student myself. I always had enjoyed learning science and engineering in school (and at home), but I had no interest in working long hours in a lab for 6 years, only to graduate looking for a job. However, after finishing a summer internship working as an electrical engineer, I immediately decided to apply to graduate school and opt for the 6 years of lab work. In retrospect, I probably could not have made a better decision. The time I have spent here at Harvard have been some of the best years of my life. The people I have met, friends I have made, and colleagues I have worked with are some of the most talented, interesting, and unique people I have ever known. I am deeply indebted to them for making graduate school such a great experience for me.

Firstly, I would like to thank my advisor, Eric Mazur, for giving me such incredible freedom and responsibility as a graduate student in his group. I really think that Eric's group is a great place for students and postdocs to learn to do research, as he has created an extremely supportive and friendly environment in which people can explore and develop their own scientific ideas while receiving expert guidance from

a great mentor. I certainly enjoyed and benefitted from this aspect of his group, and I think that many of the results of my research are direct consequences of this freedom to explore new ideas. Without the freedom to explore new ideas and ask the question what if we tried ... ?, many of the most exciting experiments that have come out of our research would never be possible. An advisor with the confidence to let his students try out their own new ideas combined with a lab full of extensive and experimentally flexible facilities truly has been a blessing for me. I cannot thank Eric enough for helping me grow as both a scientist and a person.

Secondly, I would like to thank all of the other members of the Mazur group for working with, as well as teaching me, throughout graduate school. When I first visited the group during the departmental open house, I met Jim Carey, who I was immediately impressed by. Jim has been an inspiration for me throughout graduate school. During the first two years of my time in the Mazur group, when we overlapped, Jim taught me a great deal of things in the lab. Over the years, Jim has also given me much invaluable advice from his experiences, both personally and professionally, which I will always remember. A truly great friend of mine, I am sure that he will continue on his path of great successes in both science, business, and life. Rafael Gattass was a senior graduate student in the Mazur group when I joined. His incredible knowledge of physics was, and still is, an inspiration to me. Rafael perhaps taught me the most about experimental physics of any one single person, and I hope that I have been able to teach some of the younger students in the group half as much as Rafael has taught me. Another great friend, teacher, and teammate (especially on the volleyball court), Rafael was always willing to listen to ideas that I had for new

---

experiments, no matter how crazy they were, and give me constructive, thoughtful criticism. I hope to work with Rafael again some day. I have to thank Brian Tull for also being a great mentor of mine. Brian started me out in the lab, showing me how to run the first femtosecond laser system I ever used. He also introduced me to the black silicon project, and really helped me to get started in both the group's labs and in the clean room facilities. Outside of the lab, Brian and his wife Ruby became great friends of mine, and were sorely missed when they left Cambridge. Geoff Svacha was my "next door" office neighbor for several years, who always was willing to talk about science or the past weekend. Geoff showed me that it was indeed possible to have a good time outside of the lab as well as inside it. I am also grateful to the other members of the group during my first few years for giving me feedback and advice on all things graduate school-related: Tommaso Baldacchini, Maria Kandyla, Iva Maxwell, Prakriti Tayalia, Loren Cerami, Sam Chung, and Mike Sheehy. The other members of my class, Jessica Watkins, Tina Shih, and Mark Winkler, have become great friends of mine as well. It has been both fun and exciting to go through the graduate school process alongside all of you, and I am certain you will have great success in your careers and in life. I want to thank Jessica for being such a great friend over these years, as she has always has been a fun person to talk with in the office. Even though she possesses the fatal flaw of being a University of Maryland basketball fan, she has always been a good sport about it :) Tina's infectious laugh and enthusiasm was always great to have around the lab, in addition to her vast knowledge of Adobe software. I particularly would like to thank her for helping make several great halloween costumes for me. Mark was an incredible person to share a

lab with. I have never met such a well rounded, talented person. Perhaps one of my biggest contributions to the Mazur group was to help convince Eric Mazur to take Mark on as a graduate student (although it didn't take very much convincing). It has been a pleasure to work with Paul Peng, a postdoc that joined the group towards the end of my graduate school career. I have benefited greatly from working closely with him, as he infused me with a new sense of enthusiasm for the projects we were working on, and taught me many invaluable things about chemistry. The results of chapters 4 and 5 would not have been possible without his contributions. I would also like to thank another new postdoc, Valeria Nuzzo, for her contributions to the work in Chapter 5, and for sharing and helping maintain the RegA laser system and microscope used in both Chapters 4 and 5.

It has been a pleasure to get to know and work with the next generation of graduate students in the group. Kevin Vora, Renee Sher, Chris Evans, Jason Dowd, Sally Kang, Yuting Lin, Michael Moebius, and Kasey Phillips are the future of the Mazur group. I know you all will do great work and have success in your research, but I hope that you all also take time to enjoy your graduate school experience outside of the lab as well.

Perhaps the best part of graduate school for me has been the opportunity to make some of the best friends of my life. I was fortunate enough to meet Rico Rojas, Hobie Hoffmann, and Drew Koh my first year, living in Conant dormitory. We all became great friends almost instantly, and have remained so ever since. Some of the best times of my life were had in the past few years with you guys - the list of which is far too long for this document. The adventures that we have been on and the incredible

times we had together since that first year has created lifelong bonds between us that will never be broken. Viren Jain became a part of this close group of friends over the past few years as well. Although seemingly inconsequential, I am specifically indebted to Viren for helping me get the L<sup>A</sup>T<sub>E</sub>X formatting of this thesis working. I am sure that graduate school would not have been nearly as enjoyable as it was for me without all of you.

I would like to thank Professors Federico Capasso and Ken Crozier for serving on my thesis committee. In addition to offering invaluable advice on my research and career, Federico taught my favorite course that I took at Harvard. His enthusiasm for science is inspiring, and I cannot help but feel excited about research after hearing him talk. I have had the pleasure of working with Ken Crozier on the DARPA SERS program. His excellent leadership and organization skills served as a great example to me of how to effectively manage a group comprised of people with different areas of expertise. Additionally, Ken posed the question "how can we get molecules to reside only in the hot spots of a SERS substrate?" to me when we were putting the DARPA proposal together, which eventually led to the results presented in Chapter 4.

Finally, I would like to thank my parents for all of their support and generosity during my Ph.D. Whenever I needed advice, help, or just someone to talk to about anything, they have been there for me. I am fortunate to have such loving people in my life. Their unconditional support and belief in me has given me the self-confidence

that has enabled me to complete this thesis.

*Eric Diebold  
Cambridge, Massachusetts  
May, 2010*

### **Acknowledgement of Financial Support**

This thesis is based on work supported by the Defense Advanced Research Projects Agency (DARPA) under Contract FA9550-08-1- 0285, the National Defense Science and Engineering Graduate (NDSEG) fellowship, and the Center for Nanoscale Science at Harvard University.

# Citations to Published Work

Parts of this dissertation cover research reported in the following articles:

- [1] E. D. Diebold, N. H. Mack, S. K. Doom, and E. Mazur, “Femtosecond laser-nanostructured substrates for surface-enhanced Raman scattering,” *Langmuir*, vol. 25, no. 3, pp. 1790–1794, 2009.
- [2] E. D. Diebold, P. Peng, and E. Mazur, “Isolating surface-enhanced Raman scattering hot spots using multiphoton lithography,” *Journal of the American Chemical Society*, vol. 131, no. 45, pp. 16356–16357, 2009.
- [3] R. L. Aggarwal, L. W. Farrar, E. D. Diebold, and D. L. Polla, “Measurement of the absolute Raman scattering cross section of the  $1584\text{-cm}^{-1}$  band of benzenethiol and the surface-enhanced Raman scattering cross section enhancement factor for femtosecond laser-nanostructured substrates,” *Journal of Raman Spectroscopy*, vol. 40, no. 9, pp. 1331–1333, 2009.
- [4] E. D. Diebold, P. Peng, A. Koh, V. Nuzzo, M. Schomaker, A. Heisterkamp, and E. Mazur, “Plasmon-enhanced ultrafast laser delivery of siRNA into cells,” *In preparation*, 2010.

*To* MY PARENTS, WHO HAVE SUPPORTED ME IN EVERYTHING I HAVE EVER DONE

*Just play. Have fun. Enjoy the game.*

MICHAEL JORDAN

# Chapter 1

## Introduction

### 1.1 Organization of the thesis

This thesis is organized into five main sections. The first chapter introduces some of the relevant subjects of the fields of plasmonics and ultrafast laser applications, as they apply to the work presented in the later chapters. Chapter 2 covers the main results of the theory describing the various physical phenomena discussed in Chapters 3, 4, and 5. This theoretical background section is presented such that reader can understand the physical principles behind the results of the following experimental sections. Finally, Chapter 6 will conclude the thesis, and present a summary of future directions for the research.

## 1.2 Scientific introduction

Despite the fact that the laser was invented 50 years ago [1], femtosecond laser pulses were only first demonstrated in the mid-1970's [2]. This significant development and subsequent improvements on femtosecond modelocked lasers have enabled revolutionary scientific achievements across the fields of chemistry, physics, and biology. The incredible impact of these laser sources can be attributed to two distinct and unique features of femtosecond optical pulses: short time duration and high peak power. Since femtoseconds ( $10^{-15}$  sec.) represent a fundamental timescale in nature of many atomic and electronic processes, these short laser pulses can be used as a strobe to observe events such as chemical reaction dynamics [3], phase changes in highly excited solid state materials [4], and electron dynamics in semiconductors [5]. In the case of chemical reaction dynamics, the advances made possible by the short time duration of these pulses have been so revolutionary that a Nobel prize in chemistry was awarded in 1999 for the development of femtosecond laser techniques that enabled an understanding of the fundamental processes and pathways that chemical reactions take. The second unique feature of femtosecond laser pulses is their large ratio of peak power to pulse energy. This ratio implies that the effect of sample heating can effectively be avoided, enabling one to study the response of a system to a large applied electric field. In fact, optical fields of magnitude significantly greater than that of the atomic binding strength (approximately  $10^{10}$  V/m) are generated routinely today using only nano-Joules of energy, using commercially-available tabletop laser systems and focusing lenses. This aspect of femtosecond laser pulses allows us to generate nonlinear optical effects in materials, without depositing a large amount

of energy into the system. As a result of this, femtosecond laser pulses can be used to evoke nonlinear effects in materials or systems that would ordinarily not be able to withstand the thermal load of longer laser pulses of similar peak intensity. This fact has enabled researchers to perform feats such as sub-cellular nanosurgery [6, 7] or two-photon excitation fluorescence microscopy [8] on biological specimens, without appreciable thermal damage.

The high peak power associated with femtosecond laser pulses is not the only requirement for many nonlinear effects, such as harmonic generation, multiphoton absorption, nonlinear pulse propagation, etc., to occur. Almost all nonlinear effects scale proportionately with the optical intensity (or some higher power of the intensity). Since an optical pulse's power is related to its intensity by

$$P \propto I \cdot A \quad (1.1)$$

where  $P$  is the peak power of the optical pulse,  $I$  is the spatially-averaged instantaneous intensity and  $A$  is the cross-sectional area of the pulse, the focusing of femtosecond laser pulses is critical for generating nonlinear effects in materials. One option to generate these high intensities is to use conventional refractive or reflective focusing optics. Due to the diffraction limit, this type of focusing can confine light to transverse dimensions of approximately

$$d \approx \frac{\lambda}{2 \cdot \text{NA}} \quad (1.2)$$

where  $d$  is the radius of the diffraction-limited spot,  $\lambda$  is the wavelength of the light, and NA is the numerical aperture of the focusing lens or mirror. For visible light, it is difficult to achieve  $d$  less than about 200 nm, even when using the highest-NA microscope objective lenses available today. Since this fundamental diffraction

limit is imposed on light focused to the far-field in free space, we must take advantage of other physical mechanisms to reduce this spot size, and confine light further.

With the advent of modern nanofabrication tools and techniques, the ability to fashion materials into precise features at the nanoscale has become progressively simpler and more available to researchers. This has led to a great deal of research progress in the field known as plasmonics [9]. Plasmonics is a subset of optical physics, in which the collective charge oscillations in metals (plasmons) are utilized to manipulate light on length scales much smaller than its free-space wavelength [10]. As we will show in Chapter 2, the electric (and hence, magnetic) fields associated with these charge oscillations can be confined to regions of subwavelength dimension. This confinement generates field amplitudes enhanced relative to their unconfined free-space values by potentially several orders of magnitude. Since this field confinement near metallic nanostructures can enhance the local optical intensity, we should also expect an enhancement of intensity-dependent phenomena in this region as well. As we will show, the use of femtosecond laser pulses in combination with plasmonic nanostructures represents an attractive opportunity to create highly confined optical fields of extreme intensities for the manipulation of matter on nanometer length scales.

Chapter 3 discusses the fabrication and characterization of a nanostructured surface used to enhance these local fields, within the context of surface-enhanced Raman scattering. In Chapter 4, we use this nanostructured surface to explore the enhancement of nonlinear absorption, with the end goal of improving surface-enhanced Raman scattering from adsorbed molecules. Finally, in Chapter 5, we will explore the possibility of using plasmon-enhanced nonlinear absorption to optically generate transient

pores in biological cells, with the goal of developing a high-throughput method for the introduction of silence ribonucleic acid molecules into cells.

# Chapter 2

## Theoretical background

### 2.1 Introduction

In preparation for discussion of the experiments presented later in this thesis, we will first review some of the theory of the various physical phenomena that will be encountered. First, we present some of the pertinent results from the electromagnetic theory of scattering from a subwavelength-sized spherical particle. This result describes some of the underlying physics of localized plasmon resonances, as well as motivates the surface-enhanced phenomena that will be discussed throughout this thesis. Next, we present a classical picture description of spontaneous Raman scattering. We will then extend this discussion to the topic of surface-enhanced Raman scattering (SERS), which will be the fundamental topic covered in Chapters 3 and 4. Finally, we will cover the physics of multiphoton transitions, a central phenomenon employed in the experiments described in Chapters 4 and 5. The aim of this theoretical background section is to provide the reader with sufficient details to understand

the experimental results presented in the later chapters of this thesis. For more extensive theoretical treatments of these topics, the author will suggest appropriate external references within each section.

## 2.2 Localized surface plasmon resonance: fields scattered by a subwavelength sphere

Plasmons are collective electron oscillations driven coherently by an oscillating external electric field. While there are examples of both localized and propagating plasmons, we will limit our theoretical discussion to localized plasmon resonances, as they are relevant to the work presented later in this thesis. As we will show in this section, these collective charge oscillations can enable a localized enhancement of the electric field, as compared to the driving field. The region of enhanced electric field is typically confined to a surface, with spatial extent much smaller than the wavelength of the driving field. Because of this enhancement and its associated spatial confinement to surfaces, certain linear and nonlinear light-matter interactions (scattering, absorption, emission, frequency conversion, etc.) can be enhanced relative to their free-space interaction probability when occurring in close proximity to the surface of structures that exhibit plasmon resonances. To examine this localized field enhancement in a simple system, we will derive the electric potential and field scattered by a spherical particle under plane wave illumination.

To calculate the electrodynamics of a monochromatic plane wave of electric field amplitude  $E_0$  and frequency  $\omega_0$  interacting with a polarizable spherical particle placed

at the origin, we consider the situation shown in Figure 2.1. In the current example, we will analyze the situation in which the sphere size is small compared to the wavelength of the incident plane wave ( $r_{sphere} < 0.05\lambda$ ). This is a convenient example to choose for two reasons. Firstly, this situation is relevant to most of the experimental work described in Chapters 3 and 4, in which we will be discussing the interaction of laser light with metallic nanoparticles. Secondly, the fact that the sphere is much smaller than the wavelength of the plane wave, allows us to assume that the electric field is homogeneous across the extent of the sphere. This will permit us to solve for the potential and field around the sphere using the quasi-static approximation. We will solve the associated electrostatic problem of a sphere in a homogeneous electric field, and assume that the resulting scattered fields will oscillate with the same frequency as the driving field,  $\omega_0$ . In practice, this approximation is usually valid for spheres with radii smaller than 5% of the incident wavelength.

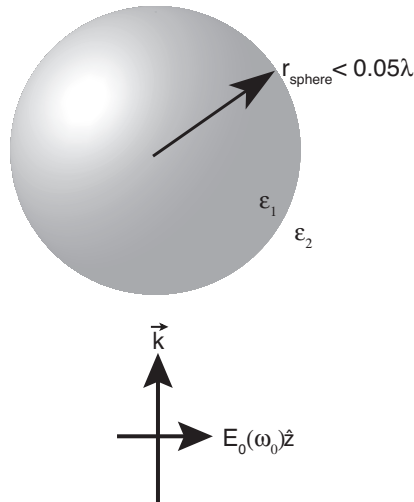


Figure 2.1: Subwavelength sphere irradiated by a plane wave at frequency  $\omega_0$ .

As shown in Figure 2.1, a plane wave propagating in the direction of its wavevector

$\vec{k}$  with its polarization in the  $\hat{z}$  direction is incident upon a sphere. Using the quasi-static approximation, we can now assume that a static electric field of amplitude  $E_0$  is applied in the  $\hat{z}$  direction, such that  $\vec{E} = E_0\hat{z}$ . A schematic of this approximation is shown in Figure 2.2.

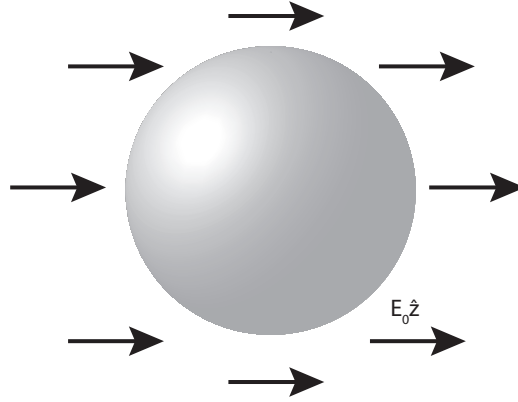


Figure 2.2: Sphere in a static, uniform electric field, illustrating the result of the quasi-static approximation.

To solve for the static fields both inside and outside the sphere, we can analytically solve for the scalar potential,  $\Phi$ , using the Laplace equation [11],

$$\nabla^2\Phi = 0 \quad (2.1)$$

in the absence of any free charges. To solve this equation, we must impose boundary conditions at the surface of the sphere, such that the tangential component of the electric field is continuous across the boundary,

$$\frac{\partial\Phi_1}{\partial\theta} = \frac{\partial\Phi_2}{\partial\theta} \quad (2.2)$$

and the normal component of the electric displacement,

$$\epsilon_1 \frac{\partial\Phi_1}{\partial r} = \epsilon_2 \frac{\partial\Phi_2}{\partial r} \quad (2.3)$$

is continuous across the boundary at  $r = r_{sphere}$ , where the subscripts 1 and 2 refer to quantities inside and outside the sphere, respectively. We also require that in the limit of  $r \rightarrow \infty$ , the potential outside the sphere,  $\Phi_2$ , is equal to the applied potential,  $-E_0z$ . From these boundary conditions, we can solve for the electrostatic potentials inside and outside the sphere:

$$\Phi_1 = -\frac{3\epsilon_2}{\epsilon_1 + 2\epsilon_2}E_0r \cos \theta \quad (2.4)$$

$$\Phi_2 = -E_0r \cos \theta + \frac{\epsilon_1 - \epsilon_2}{\epsilon_1 + 2\epsilon_2}r_{sphere}^3 E_0 \frac{\cos \theta}{r^2}. \quad (2.5)$$

To calculate the corresponding electric fields, we take the negative gradient of the potentials ( $\vec{E} = -\nabla\Phi$ ), to give

$$\vec{E}_1 = \frac{3\epsilon_2}{\epsilon_1 + 2\epsilon_2}(\hat{r}E_0 \cos \theta - \hat{\theta}E_0 \sin \theta) = \frac{3\epsilon_2}{\epsilon_1 + 2\epsilon_2}E_0\hat{z} \quad (2.6)$$

and

$$\vec{E}_2 = \hat{r}E_0 \cos \theta - \hat{\theta}E_0 \sin \theta + \frac{\epsilon_1 - \epsilon_2}{\epsilon_1 + 2\epsilon_2} \frac{r_{sphere}^3}{r^3} E_0(\hat{r}2 \cos \theta + \hat{\theta} \sin \theta) \quad (2.7)$$

$$= E_0\hat{z} + \frac{\epsilon_1 - \epsilon_2}{\epsilon_1 + 2\epsilon_2} \frac{r_{sphere}^3}{r^3} E_0(\hat{r}2 \cos \theta + \hat{\theta} \sin \theta). \quad (2.8)$$

There are several things to note about this result. First, the field inside the sphere is constant, and is polarized along the  $\hat{z}$  axis. Second, if we examine equation 2.8, we can see that at the point on the  $\hat{z}$  axis where  $r = r_{sphere}$ , the quantity  $E_2$  is related to  $E_0$  by the factor

$$\left| \frac{\vec{E}_2}{E_0} \right| = 2 \frac{\epsilon_1 - \epsilon_2}{\epsilon_1 + 2\epsilon_2}. \quad (2.9)$$

If we set  $\epsilon_2 = 1$ , as in the case of air, we can see that the denominator will equal zero if  $\epsilon_1 = -2$ . In this case, the denominator will vanish, giving rise to a pole

in the dielectric function. At this condition, the scattered field will be optimally enhanced relative to the driving field. We will briefly discuss the dielectric function of metals in the following section, where we will state the conditions for this optimum enhancement. Finally, the scattered field distribution has the same form as that of an ideal electric dipole located at the center of the sphere with dipole moment

$$\vec{p} = \alpha \cdot \vec{E} = 4\pi r_{sphere}^3 \frac{\epsilon_1 - \epsilon_2}{\epsilon_1 + 2\epsilon_2} E_0 \hat{z}. \quad (2.10)$$

In this case, the dipole polarizability,  $\alpha$  has the form

$$\alpha = 4\pi r_{sphere}^3 \frac{\epsilon_1 - \epsilon_2}{\epsilon_1 + 2\epsilon_2}. \quad (2.11)$$

This polarizability is important for describing surface-enhanced Raman scattering, which will be discussed in section 2.4. For a more detailed description of scattering of light by subwavelength particles, the author recommends reference [12].

### 2.2.1 Dielectric function result from the Drude model of electrons in a metal

The response of metals to optical frequency electromagnetic fields in the linear regime is often described by the somewhat simple, but useful Drude model. This model approximates a metal as a collection of immobile ions, surrounded by a sea of free, non-interacting electrons. These electrons are assumed to be neutral particles that scatter off of the ions with a probability per unit time,  $\frac{1}{\tau}$ . This gives the average time between electron-ion scattering events to be  $\tau$ . For metals such as gold or silver at room temperature, this characteristic time is on the order of  $10^{-14}$  to  $10^{-15}$  seconds [13]. This simple model can be used to approximate the dielectric function of

metals such as silver and gold in the visible frequency range, which can be expressed as

$$\epsilon(\omega) = \epsilon' + i\epsilon'' \quad (2.12)$$

where

$$\epsilon'(\omega) = 1 - \frac{\omega_p^2}{\omega^2} \quad (2.13)$$

and

$$\epsilon''(\omega) = \frac{\omega_p^2 \gamma}{\omega^3}. \quad (2.14)$$

The plasma frequency  $\omega_p$  is expressed as

$$\omega_p^2 = \frac{4\pi n e^2}{m} \quad (2.15)$$

where the quantities  $n$ ,  $e$ , and  $m$  correspond to the electron density, electronic charge, and the effective mass of the electrons in the metal, respectively. In equation 2.14,  $\gamma$  represents a non-zero damping constant associated with the electron motion. From equation 2.13, we can see that when  $\omega = \omega_p/\sqrt{3}$ , the field enhancement factor in equation 2.9 is maximized. This field enhancement remains finite, however, due to the non-vanishing imaginary component of the dielectric function,  $\epsilon''$ . This pole in equation 2.8 and the corresponding peak in field enhancement corresponds to the physical phenomenon of *localized surface plasmon resonance*, in which the displacement of the sea of free electrons in the metal is  $90^\circ$  out of phase with the driving field, and the amplitude of this displacement is maximized. For silver or gold metallic nanoparticles, these resonances typically occur in the visible portion of the electromagnetic spectrum, and the peak field enhancements at the surface are typically on the order of 5 or 10.

## 2.3 Raman scattering

Raman scattering was discovered in 1928 [14] by Sir Chandrasekhara Venkata Raman, for which he was awarded the Nobel prize in physics in 1930. In this section, we will describe spontaneous Raman scattering: the inelastic photon-phonon scattering process which enables the identification of vibrational modes of a molecule. Because of its simpler mathematical description, here we present the mathematics and physics of the Raman scattering process in a classical formulation, as opposed to a quantum mechanical formulation. While there are several limitations of the classical description, it does give insight into the basic physics of the process, and is easier incorporated with the theory from the previous section to describe surface-enhanced Raman scattering, which will be the subject of section 2.4.

The derivation in this section is based on that contained in Ref. [15]. To analyze the inelastic electromagnetic scattering from a molecule, we calculate the frequency-dependent linear polarization, or electric dipole moment

$$\vec{p} = \alpha \cdot \vec{E} \quad (2.16)$$

where  $\alpha$  is the molecular polarizability tensor, and  $\vec{E}$  is the electric field vector of the incident monochromatic electric field at frequency  $\omega_0$ . The polarizability tensor, in general, is a function of the generalized nuclear normal coordinate  $Q$ , and thus is also a function of the vibrational frequencies of the molecule. As the molecule vibrates, the instantaneous polarizability will also change, due to the fluctuating internuclear distances in the molecule. This yields the polarizability tensor a function of the generalized coordinate  $Q$ . If we consider a single molecule, free to vibrate but not

to rotate (the nuclei of the molecule are allowed to vibrate about their equilibrium positions), we can express the variation of the molecular polarizability with respect to the molecular vibration as a Taylor series in  $Q$ :

$$\alpha_{\rho\sigma} = (\alpha_{\rho\sigma})_0 + \sum_k \left( \frac{\partial \alpha_{\rho\sigma}}{\partial Q_k} \right)_0 Q_k + \frac{1}{2} \sum_{k,l} \left( \frac{\partial^2 \alpha_{\rho\sigma}}{\partial Q_k \partial Q_l} \right)_0 Q_k Q_l + \dots \quad (2.17)$$

where  $(\alpha_{\rho\sigma})_0$  is the polarizability tensor element at the molecule's equilibrium configuration,  $Q_k$ ,  $Q_l$  are the normal coordinates associated with molecular vibrational frequencies  $\omega_k$ ,  $\omega_l$ , and the derivatives of the polarizability tensor elements are taken at the equilibrium configurations. For this derivation, we need only keep the first order term in  $Q_k$ , and we can consider only one mode of vibration. The polarizability tensor then becomes

$$(\alpha_{\rho\sigma})_k = (\alpha_{\rho\sigma})_0 + (\alpha'_{\rho\sigma})_k Q_k \quad (2.18)$$

where

$$(\alpha'_{\rho\sigma})_k = \left( \frac{\partial \alpha_{\rho\sigma}}{\partial Q_k} \right)_0 \quad (2.19)$$

where we can then simplify our notation, such that we generalize for all values of the tensor

$$\alpha_k = \alpha_0 + \alpha'_k Q_k. \quad (2.20)$$

Under a monochromatic plane wave driving field

$$E(t) = E_0 \cos(\omega_0 t) \quad (2.21)$$

the solution to the equation of motion for the generalized nuclear coordinate  $Q_k$  is given by

$$Q_k = Q_{k0} \cos(\omega_k t + \delta_k) \quad (2.22)$$

where  $Q_{k0}$  is the amplitude of the vibration, and  $\delta_k$  is an additional phase term. We can combine equations to yield the polarizability tensor for the  $k^{th}$  vibrational normal mode of the molecule

$$\alpha_k = \alpha_0 + \alpha'_k Q_{k0} \cos(\omega_k t + \delta_k). \quad (2.23)$$

When substituted into the form of the induced linear electric dipole moment, we find

$$p = \alpha_0 E_0 \cos(\omega_0 t) + \alpha'_k E_0 Q_{k0} \cos(\omega_k t + \delta_k) \cos(\omega_0 t). \quad (2.24)$$

We use the trigonometric identity

$$\cos(A)\cos(B) = \frac{1}{2}\{\cos(A+B) + \cos(A-B)\} \quad (2.25)$$

to rearrange the second term in the induced dipole moment expression to yield a polarization in the frequency domain of the form

$$p(\omega) = p(\omega_0) + p(\omega_0 - \omega_k) + p(\omega_0 + \omega_k) \quad (2.26)$$

where the polarizations at the three different frequency components are

$$p(\omega_0) = \alpha_0 E_0 \cos(\omega_0 t) \quad (2.27)$$

$$p(\omega_0 - \omega_k) = \frac{1}{2} \alpha'_k E_0 Q_{k0} \cos[(\omega_0 - \omega_k)t - \delta_k] \quad (2.28)$$

$$p(\omega_0 + \omega_k) = \frac{1}{2} \alpha'_k E_0 Q_{k0} \cos[(\omega_0 + \omega_k)t + \delta_k] \quad (2.29)$$

Here we can see that the dipole moment now has frequency components other than the frequency of the incident driving field,  $\omega_0$ . This polarization acts as a source term in Ampere's Law,

$$\nabla \times \vec{H} = \epsilon_0 \frac{\partial \vec{E}}{\partial t} + \frac{\partial \vec{p}}{\partial t} \quad (2.30)$$

where  $H$  is the magnetic field. This polarization produces electromagnetic fields at frequencies  $\omega_0$ , and  $\omega_0 \pm \omega_k$ . The electromagnetic fields radiated at the frequencies  $\omega_0$ ,  $\omega_0 - \omega_k$ , and  $\omega_0 + \omega_k$  are known as the Rayleigh, Stokes, and anti-Stokes scattered field components, respectively. All three of these fields are proportional in amplitude to the driving field amplitude,  $E_0$ . This implies that the three scattering processes are linear. Examining equation 2.27, we can write

$$p(\omega_0) = p_0^{Rayleigh}(\omega_0) = \alpha_0 E_0 \cos(\omega_0 t) \quad (2.31)$$

such that we can define the so-called Rayleigh polarizability as

$$\alpha^{Rayleigh} = \alpha_0. \quad (2.32)$$

We can also show

$$p(\omega_0 \pm \omega_k) = p_{k0}^{Raman} \cos[(\omega_0 \pm \omega_k)t \pm \delta_k] \quad (2.33)$$

where the Raman polarization can be expressed as

$$p_{k0}^{Raman} = \alpha_k^{Raman} \cdot E_0 \quad (2.34)$$

such that we can define the so-called Raman polarizability as

$$\alpha_k^{Raman} = \frac{1}{2} \alpha'_k Q_k. \quad (2.35)$$

Thus, the so-called  $k^{th}$  Raman polarizability,  $\alpha_k^{Raman}$ , is proportional to the derivative of the  $k^{th}$  polarizability with respect to the generalized nuclear coordinate,  $Q_k$ . This has implications that determine the Raman activity of certain vibrational modes in molecules. The derivative of the molecular polarizability at the equilibrium position,

$$\alpha'_k = \left( \frac{\partial \alpha_k}{\partial Q_k} \right)_0 \quad (2.36)$$

must be nonzero for the  $k^{\text{th}}$  vibrational mode to be “Raman active.” This, in a sense, is the definition of the selection rule for the  $k^{\text{th}}$  vibrational mode of a molecule to participate in a Raman scattering event. As an example, we will consider a few simple cases of molecular vibrations to illustrate this point. In homonuclear diatomic molecules, denoted by  $A_2$ , there is only one mode of vibration. Due to the charge distribution symmetry about the center of the molecule, there is no permanent dipole moment associated with the molecule. The dipole moment is always zero during small vibrations, and thus the derivative of the dipole moment with respect to  $Q_k$  is zero. However, the *polarizability* of an  $A_2$  molecule changes slightly with a varying  $Q_k$ , and the derivative of the polarizability is non-zero at the equilibrium position. This means the  $A_2$  molecule has at least one Raman active mode, and it will produce sidebands in its light scattering spectrum. In the diatomic molecule, denoted by AB, there will always be a permanent dipole moment as it vibrates. In addition, the molecule’s polarizability will vary with molecular vibration, yielding it Raman active as well. These two cases differ with respect to infrared absorption spectroscopy. Due to quantum mechanical selection rules imposed on infrared optical transitions, a non-zero dipole moment is required for the molecule to be “infrared active,” or absorb infrared light in a direct transition from its ground state to an excited vibrational state. Classically, this means the derivative of the molecule’s dipole moment with respect to  $Q_k$  is non-zero. Thus we see that Raman scattering is often a complementary process to infrared absorption spectroscopy for performing vibrational spectroscopy. As an example of a vibrational mode that does not have a non-zero Raman polarizability, we consider a linear ABA molecule. In the case shown

in Figure 2.3 for a linear, antisymmetric stretching mode, the molecule does not have a non-zero derived polarizability at its nuclear equilibrium position.

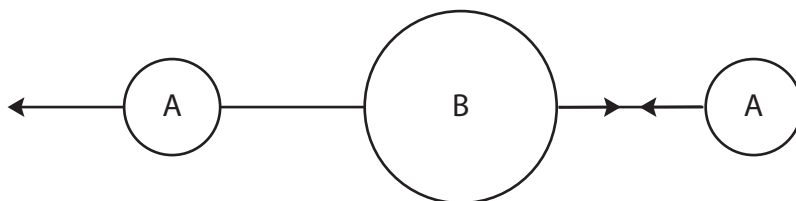


Figure 2.3: Example of a molecular vibrational mode which is not Raman active.

Different vibrational modes in a molecule will exhibit different Raman polarizabilities, and thus, Raman intensities. For example, a  $C = C$  double bond has delocalized electrons, due to the  $\pi$ -bond. This greatly increases the bond's polarizability, which yields a much larger Raman intensity. Compared to an  $A_2$  molecule with only one  $s$ -bond, the  $C = C$  double bond vibrational mode will Raman scatter light much more efficiently.

This classical analysis of an oscillating electric field interacting with a vibrating molecule provides a simple argument to explain the sidebands exhibited in the light scattering spectrum of molecules. While this classical analysis does not provide insight into the relative amplitudes of the Stokes and anti-Stokes scattered fields or the  $\omega^4$  scattered field intensity dependence on the frequency of the driving field, it does give a simple argument that enables a physical understanding of the Raman scattering process. Akin to amplitude modulation in RF electronics, Raman scattering is also a frequency mixing process in a nonlinear system. However, by measuring the frequency shift of these Raman sidebands from the driving field frequency  $\omega_0$ , the unique set of vibrational frequencies  $\omega_k$  can be determined for a given molecule. In practice, these

frequency shifts (measured in wavenumbers, with unit  $\text{cm}^{-1}$ ) are usually calculated from a measured wavelength shift, as described by equation 2.37.

$$\Delta\nu(\text{cm}^{-1}) = \frac{1}{\lambda_{\text{driving}}} - \frac{1}{\lambda_{\text{scattered}}} \quad (2.37)$$

An example of a typical Raman spectrum from a solid-state sample is shown in Figure 2.4. By collecting and analyzing the Raman scattered light, the intensities and frequencies of the various spectral sidebands give insight into the Raman active vibrational modes of a molecule. Since each molecule has a unique set of vibrational modes, the Raman spectrum can be used as a type of molecular fingerprint to identify the scattering molecular species. In practice, this is often performed by exciting the sample using a narrow-linewidth continuous wave laser source, typically in the visible wavelength range. Light scattering from the sample is collected, and spectrally dispersed by a monochromator. By analyzing the output of the monochromator with a detector, these spectral sidebands can be observed.

For a more complete picture of Raman scattering, especially to include effects of electronic resonances, a quantum mechanical description of the process is required. However, for our purposes of providing a background to the experiments described in this thesis, we only need results from the classical description. For a more thorough description of the quantum mechanical picture of Raman scattering, the author suggests reference [15].

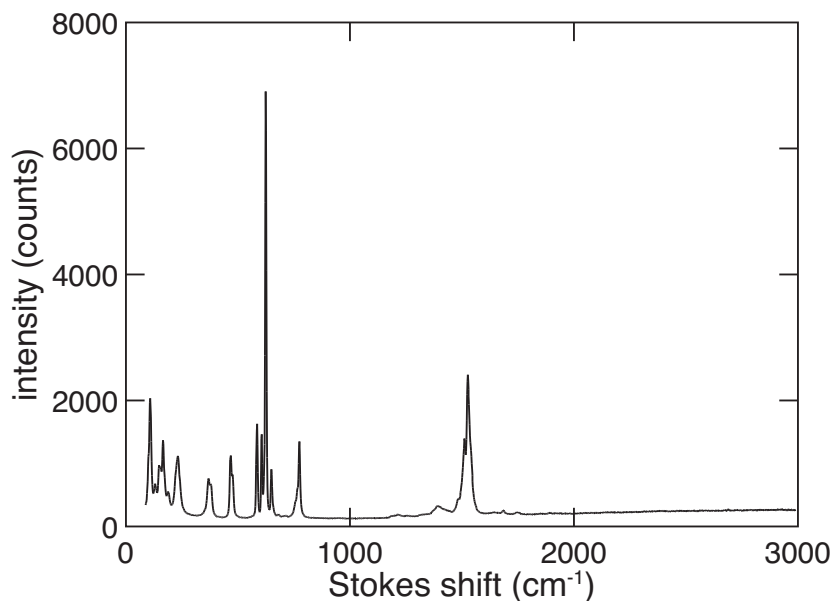


Figure 2.4: Typical Raman spectrum taken from a  $\beta$ -barium borate crystal, using 632.8 nm laser excitation. Zero wavenumbers corresponds to the driving field frequency, and increasing Stokes shift (wavenumbers) corresponds to higher frequency (energy) vibrational modes of the sample.

## 2.4 Surface-enhanced Raman scattering

Despite being a very convenient technique for analyzing the vibrational modes of a sample, the Raman scattering process is extremely inefficient. The probability of a molecule undergoing a Raman-scattering process (in a quantum mechanical picture of the process) is described in terms of its Raman scattering cross-section, or  $\sigma_{Raman}$ . Classically speaking, the Raman scattering process is always occurring, and the cross section simply is a measure of the ratio of the Raman scattered light intensity to the excitation light intensity. To give an example for comparison, the cross-section of a typical organic fluorescent molecule, such as Rhodamine 6G, is on the order of  $10^{-16}\text{cm}^2$ . However, the typical non-resonant Raman scattering cross section of that

same molecule is on the order of  $10^{-30}\text{cm}^2$ . This difference of 14 orders of magnitude between typical fluorescence and Raman scattering cross-sections makes fluorescence a much more sensitive detection technique than Raman scattering. However, for applications in which information about a sample is desired, Raman scattering has the significant advantage of providing a specific, unique spectroscopic fingerprint, as opposed to a broad, ambiguous fluorescence emission spectrum. Because of the additional information provided by a Raman spectrum, there is great interest in finding ways to improve effective Raman scattering cross sections. Since its discovery in the 1970's [16, 17], the enhancement of Raman scattering cross sections of molecules adsorbed to nanostructured metallic surfaces has been researched quite heavily. Here we will discuss the electromagnetic enhancement mechanism of surface-enhanced Raman scattering, and point out some of its important aspects, as it applies to the experiments discussed in this thesis.

To increase the efficiency of the Raman scattering process, we must increase the Raman cross section, or effective Raman cross section, of the molecules being probed. Since the induced Raman polarization, and hence the Raman scattered field, scales linearly with the incident electric field, the intensity of the scattered radiation will be proportional to the intensity of the incident field. Due to this linearity, simply increasing the irradiance on the molecule will not increase its effective cross section. An alternative is to passively enhance the electric field intensity a molecule experiences, by placing it in the near field of a metallic object (such as a metallic nanostructure) that exhibits a surface plasmon resonance. This surface enhancement of the electric field via surface plasmon excitation in the nanostructure will increase the intensity of

the light scattered from the molecule via two processes: enhanced coupling of free-space excitation fields to the molecule, and enhanced out-coupling of the scattered field from molecule's polarization at the Raman frequency. These enhancement processes will increase the effective Raman cross section of the molecule non-linearly with the surface electric field enhancement factor, as we show below.

A molecule placed at the  $\hat{z}$ -axis on the surface of the sphere shown in Figure 2.1 will experience an enhancement of its polarization (including its polarization at the Raman frequency) relative to its free-space polarization, by an amount equal to the electric field enhancement factor, when the sphere is irradiated by a field  $E_0(\omega_0)\hat{z}$ . As the Raman scattering process is linear, a polarization at the Raman frequency is generated, enhanced by this same field enhancement factor relative to the free-space situation. Since this molecular polarization is in close proximity to a sphere, the sphere will become polarized at the Raman frequency, proportional to the sphere polarizability, given by equation 2.11. This re-polarization of the sphere at the Raman scattering frequency involves a few subtle details. As opposed to the case of the sphere being polarized by a plane wave, we cannot treat the electromagnetic problem of a polarized molecule located at the surface of a polarizable sphere in the quasi-static limit. Thus, the polarized molecule can excite an infinite number of multipoles in the sphere. This is due to the fact that the Raman scattered field emanating from the polarized molecule, is not a plane wave in the near field ( $r \ll \lambda_{Raman}$ ), and the sphere does not experience a uniform electric field. However, due to the fact that the sphere is significantly smaller than the wavelength of the Raman scattered light, only the induced dipole polarization in the sphere will radiate [18]. These coupling processes

combined yield a new effective Raman scattering cross section, or SERS cross section:

$$\sigma_{SERS} \approx \sigma_{Raman} \left| \frac{\epsilon_1(\omega_0) - \epsilon_2}{\epsilon_1(\omega_0) + 2\epsilon_2} \right|^2 \left| \frac{\epsilon_1(\omega_{Raman}) - \epsilon_2}{\epsilon_1(\omega_{Raman}) + 2\epsilon_2} \right|^2 \left( \frac{r_{sphere}}{r_{sphere} + r} \right)^{12}. \quad (2.38)$$

It is important to note that the first field enhancement factor (generating the enhanced polarization of the molecule) occurs at the incident field frequency, while the second factor (generating the polarization of the sphere after Raman scattering from the molecule) occurs at the Raman frequency. These two frequencies, while typically close (separated by the molecular vibrational frequencies, typically in the THz range), are not equal to each other. Relative to the frequency of the incident field,  $\omega_0$ , this difference is small, and can be ignored to yield

$$\sigma_{SERS} \approx \sigma_{Raman} \left| \frac{\epsilon_1(\omega_0) - \epsilon_2}{\epsilon_1(\omega_0) + 2\epsilon_2} \right|^4 \left( \frac{r_{sphere}}{r_{sphere} + r} \right)^{12}. \quad (2.39)$$

This is the classic “ $E^4$ ” SERS enhancement factor result. In approximation, the SERS cross section of a molecule adsorbed to a metallic nanostructure is enhanced by an amount that scales with the fourth power of the local field enhancement. In practice, however, high-frequency Raman bands of molecules adsorbed to metallic nanostructures often experience a lesser enhancement, as the nanostructure’s field enhancement is not constant over an infinite bandwidth, and this  $E^4$  approximation breaks down. The second factor in equation 2.39 is a consequence of the  $\frac{1}{r^3}$  dependence of the field enhancement outside the sphere, described in equation 2.8. Truly a surface effect, the electromagnetic SERS enhancement decays drastically, with approximately a  $\frac{1}{r^{12}}$  dependence, as the molecule resides further from the metallic nanostructure surface.

Molecules adsorbed to spherical nanoparticles of gold or silver should theoretically experience a peak SERS enhancement (due to electromagnetic effects) on the

order of  $10^3$  or  $10^4$ . In experiments with SERS, however, the situation of molecules adsorbed to single spherical metallic nanostructures is not often encountered. When two or more metallic nanoparticles reside close to each other, they can exhibit collective plasmon resonances, in which the local electric fields can be much larger than in the single particle case. For example, several theoretical and experimental studies have shown that random aggregates of metallic nanoparticles or metal island films can exhibit collective plasmon resonances that generate field enhancements at certain points that can reach factors on the order of  $10^3$  [19–24]. These regions of extraordinary enhancement in the interstices of multiple metallic nanostructures are known as “hot spots.” It is these hot spots that will play an important role in the experiment described in Chapter 4.

The author would like to acknowledge that the electromagnetic enhancement mechanism is not the only effect responsible for the SERS enhancements observed in experiments. The so-called chemical enhancement mechanism relies on the modified polarizability of a molecule adsorbed to a metallic surface [25]. This mechanism, however, is somewhat specific to both the metal surface and the adsorbed molecule. For the sake of designing a general SERS substrate useful for many molecules, the experiments in this thesis ignore the chemical enhancement mechanism as a design parameter.

## 2.5 Multiphoton transitions

In both Chapters 4 and 5, the experiments involve excitation of metallic nanostructures with near-infrared ultrafast laser pulses. Considering the intensities generated

by the nanoscale field localization of laser pulses with peak power of order  $10^7$  W, the probability that electrons in either the metal, surrounding material, or both, absorbs more than one photon at a time becomes non-negligible. Two or more photons can be absorbed by an electron simultaneously, exciting the material to an energetic state with the difference between the final and ground state energies equal to the sum of the photon energies. Simultaneous absorption of two or more photons is known as a multiphoton transition, and the probability of this type of event occurring scales nonlinearly with the incident light intensity. We will discuss the physics and implications of these transitions as they apply to the systems in Chapters 4 and 5.

If a beam of light comprised of photons with energy  $\hbar\omega$  is incident upon a material of bandgap  $E_g$ , no photons will be absorbed (effectively) if the condition  $E_g > \hbar\omega$  is met, as energy is not conserved. However, if  $E_g < n\hbar\omega$ , where  $n$  is an integer greater than 1, an electron can be promoted to a higher-lying state in the material if the intensity of the light is high enough. If we consider Fermi's golden rule:

$$W = \frac{2\pi}{\hbar} \sum_f |\langle f | \mathbf{H}_{ED} | i \rangle|^2 \delta(\omega_f - \omega_i) \quad (2.40)$$

which describes the transition rate per unit time  $W$  between states  $|i\rangle$  and  $|f\rangle$  when an oscillating electric field, or photon, is interacting with the system. The electric dipole interaction hamiltonian  $H_{ED} = \mu \cdot \vec{E}$  is the dot product of the dipole moment operator  $\mu$  with the electric field  $\vec{E}$ . The delta function imposes energy conservation in the transition. We can see that the direct transition rate between initial and final states is proportional to  $|\vec{E}|^2$ , which is proportional to the field intensity,  $I$ . Thus, the probability per unit time of a single photon transition scales linearly with optical intensity. If we extend our derivation of Fermi's golden rule to include second order

processes, or “two-photon” transitions, we have [26]:

$$W = \frac{2\pi}{\hbar} \sum_f \left| \langle f | H_{ED} | i \rangle + \frac{1}{\hbar} \sum_l \frac{\langle f | \mathbf{H}_{ED} | l \rangle \langle l | \mathbf{H}_{ED} | i \rangle}{\omega_i - \omega_l} \right|^2 \delta(\omega_f - \omega_i). \quad (2.41)$$

where the intermediate state  $|l\rangle$  does not necessarily have to be an eigenstate of the system. The transition from state  $|i\rangle$  to state  $|l\rangle$  does not have to conserve energy; only the overall transition from  $|i\rangle$  to  $|f\rangle$  must conserve energy. For example, if the incident photon energy  $\hbar\omega$  is equal to  $\hbar(\frac{\omega_f - \omega_i}{2})$ , the transition between  $|i\rangle$  and  $|f\rangle$  is not resonant with the incident photons, and the first term effectively vanishes. The second term describes a transition requiring two photons, which occurs through the intermediate state  $|l\rangle$ . If the energies of the states  $|i\rangle$  and  $|l\rangle$  are not equal, the denominator of this term reduces its contribution to the overall transition rate. This implies that the transition rate will be small if  $|l\rangle$  is a virtual state separated from the initial state  $|i\rangle$  by the photon energy  $\hbar\omega$ . This term also has a numerator that is proportional to  $|\vec{E}|^4$ , which is itself proportional to the square of the field intensity,  $I^2$ . From this analysis of transition rates, we can extract the notion that the probability per unit time of a direct transition involving two photons is small, but is proportional to the field intensity squared, as opposed to the intensity, as in the case of a single photon transition. This analysis can be extended to higher order transitions, such that we can arrive at the relationship

$$W^{(n)} \propto \sigma_n I^n \quad (2.42)$$

where  $W^{(n)}$  is the rate of  $n$ -photon transitions in a system per unit time under illumination by a time-varying electric field,  $\sigma_n$  is the  $n$ th-order transition cross-section, and  $I^n$  is the  $n$ th power of the intensity of the field. The transition cross-section,

$\sigma_n$  accounts for the various dipole matrix elements between the states involved in the transition, such that we can simplify our analysis. Typically the higher order cross sections for these multiphoton transitions decrease by several orders of magnitude with each increase in transition order, and become increasingly unlikely to occur. Equation 2.42 states that the probability of a  $n$ th-order transition occurring is proportional to the field intensity to the  $n$ th power, which means for higher-order transitions ( $n > 1$ ), the intensity must be large for the transition rate to become non-negligible.

The above analysis implies that for a multiphoton transition to occur in a system without any resonances between the intermediate and initial or final states, we must use large electric field intensities. In the work presented in this thesis, we make use of femtosecond laser pulses. The average intensity of a laser pulse is given approximately by

$$I \propto \frac{E}{\tau \cdot A} \quad (2.43)$$

where  $E$  is the pulse energy,  $\tau$  is the pulse duration, and  $A$  is the cross-sectional area of the beam. In practice, since femtosecond laser pulses are typically on the order of  $10^{-13}$  seconds, even pulse energies in the nano-Joule range can create enormous intensities ( $10^{12}$ W/cm<sup>2</sup>) if they are focused to small areas. This large intensity can generate multiphoton transitions in materials, as we will discuss in Chapters 4 and 5. In Chapter 4, a two-photon electronic interband transition in silver nanoparticles results in multiphoton-induced luminescence [27], which is used to expose a photoresist. In Chapter 5, a multiphoton absorption process is used to generate a low-density plasma of free electrons in the membrane of biological cells, for the pur-

pose of generating sub-micron sized membrane pores [6]. In both of these cases, a metallic nanostructure is employed to increase the local electric field intensity of a femtosecond laser pulse to further increase the probability of a multiphoton transition occurring.

# Chapter 3

## Femtosecond laser-nanostructured SERS substrates

### 3.1 Abstract

We present a new type of surface-enhanced Raman scattering (SERS) substrate that exhibits extremely large and uniform cross-section enhancements over a macroscopic (greater than 25 mm<sup>2</sup>) area. The substrates are fabricated using a femtosecond laser nanostructuring process, followed by thermal deposition of silver. SERS signals from adsorbed molecules show a spatially uniform enhancement factor of approximately  $10^7$ . We discuss the physical formation mechanisms of these substrates, and describe the experimental techniques used to characterize their SERS enhancement factor. Spectroscopic characterization of these substrates suggests their potential for use in few or single-molecule Raman spectroscopy.

## 3.2 Introduction

In this chapter, we present a new type of SERS substrate, based on a fabrication technique that uses a femtosecond laser to generate large, uniform areas of nanostructures on a silicon wafer. We will cover the experimental aspects of this fabrication process, and describe in detail, the techniques used to characterize the SERS performance of this substrate. Additionally we will describe some of the experimental instruments used to make these characterization measurements. Much of the text in this chapter is adapted from [28].

Since its discovery in the 1970's [16, 17, 29], SERS has provided a glimpse into the future of high throughput single-molecule detection and analysis. The wealth of vibrational spectroscopic information offered by Raman spectroscopy makes it ideal for highly multiplexed bio-assays and label-free analyte detection schemes that are not possible using the current state-of-the-art molecular dye and quantum dot based fluorescence techniques. Ordinarily, the cross section for a molecular Raman transition is extremely small, but nanostructured SERS substrates can enhance Raman signals to a level that is competitive with well-established fluorescence techniques. For example, using nanoparticle-based SERS substrates, single-molecule detection has been reported [21, 22]. Despite this achievement, the current dearth of reliable and reproducible substrates with both large-scale uniformity and large enhancement factors has severely limited the use of SERS in most applications. Metallic nanoparticles, patterned on solid substrates or aggregated from colloidal solutions, exhibit large SERS enhancement factors [20, 30, 31]. While nanoparticle-based systems are often difficult to control in terms of signal homogeneity and particle stability, and

are not typically appropriate for use in large area assays, they offer insight into the requirements for a suitable SERS substrate. The giant signal enhancements observed in these nanoparticle systems are typically dominated by the large electric fields generated in so-called ‘hot spots’ that exist in the regions between two (or more) adjacent particles [32,33]. By optimizing the number, density, and field intensity enhancement of these hot spots, SERS substrates can provide large, easily detectable signals for trace detection and identification using Raman spectroscopy. To overcome the physical limitations inherent to nanoparticle-based SERS systems, attempts have been made to use highly roughened substrates of bulk solid-state materials. For example, metallized porous silicon exhibits SERS properties after proper chemical etching treatment [34]. However, the practicality of these substrates is limited by the mechanical stability [35] of highly porous silicon, making them difficult to integrate into higher-order structures, such as microfluidics-based analytical devices. Here, we report a technique for fabrication of large area, planar silicon based SERS substrates that overcomes these physical obstacles. Using a femtosecond laser to nanostructure a silicon surface, we produce SERS substrates that exhibit reproducible and spatially uniform enhancement factors of approximately  $2 \times 10^7$  at an excitation wavelength of 632.8 nm. This enhancement decreases slowly with increasing excitation wavelengths, maintaining significant enhancement (about  $10^6$ ) out to 900 nm. In addition to the large enhancement factor, these substrates can easily be patterned in a variety of form factors over large areas.

## 3.3 Experimental details

### 3.3.1 SERS substrate fabrication

All substrates were fabricated from n-type, single crystal (100) silicon wafers ( $\rho = 0.005 - 0.020 \Omega \cdot \text{cm}$ ) using a femtosecond laser structuring process. In this process, a regeneratively-amplified titanium:sapphire laser is used to generate an 800-nm center wavelength, 100-fs pulse train at a repetition rate of 1 kHz. This pulse train was frequency-doubled to a center wavelength of 400 nm using a thin (0.5 mm) type-1 critically phase-matched  $\beta$ -barium borate (BBO) crystal (NewLight Photonics). A 2:1 Galilean down-collimating telescope is used to reduce the beam diameter to approximately 5 mm before entering the BBO crystal. By optimizing the angle-tuning of this crystal along with the 800-nm pulse compression, second harmonic conversion efficiencies of approximately 28% can be achieved in this system. The second harmonic pulse width exiting the crystal is less than 200 fs. The duration of this pulse is determined by the thickness and group velocity dispersion of the BBO crystal, as opposed to its phase-matching bandwidth, considering the input pulse duration of 100 fs. Theoretically, we could compress these pulses to shorter durations after the BBO crystal, but for their use in this experiment, the pulses only need be in the sub-picosecond regime. The frequency-doubled laser pulses are loosely focused with a plano-convex lens to achieve an average fluence of  $10 \text{ kJ/m}^2$  at the surface of a silicon wafer fastened to the inside a 10-mm deep cuvette filled with deionized water. The cuvette is mounted on a computer controlled two-axis translation stage and raster-scanned at an appropriate speed such that each point on the silicon wafer

is subjected to approximately 500 pulses. A basic schematic of this structuring setup is shown in Figure 3.1.

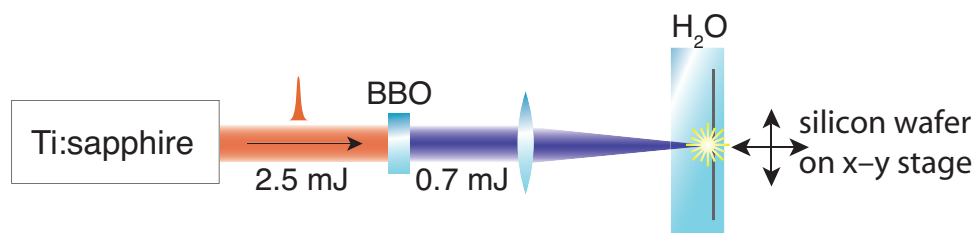


Figure 3.1: Schematic of the laser nano-structuring setup used to fabricate the silicon-based SERS substrates

Additionally, we can use a galvanometric scan mirror system that is capable of structuring silicon wafers in a similar fashion, although the experiments described in this Chapter were performed using the setup shown in Figure 3.1. With the scan mirror system, instead of moving the wafer back and forth with respect to a fixed beam location, we can hold the wafer in a fixed position, and raster the beam, nanostructuring the surface in the same fashion. This system enables us to scan areas of the wafer at higher speeds than with the translation stage method, allowing us to fabricate samples more quickly. It should also be noted that we can use a custom-designed telecentric scan lens (anti-reflection coated at both 400 nm and 800 nm) with the galvanometric scan mirror system, which is designed to keep the laser pulses at perpendicular incidence relative to the sample. This is in contrast to an F-theta scan lens, which has a flat focal plane, but does not preserve this perpendicular incidence condition at the focus.

Once the silicon wafers have been structured using the laser process, they are removed from the cuvette, and rinsed with deionized water. An example of a sample generated using the translation stage system is shown in Figure 3.2, although samples

generated using the galvanometric scan mirror system look identical.

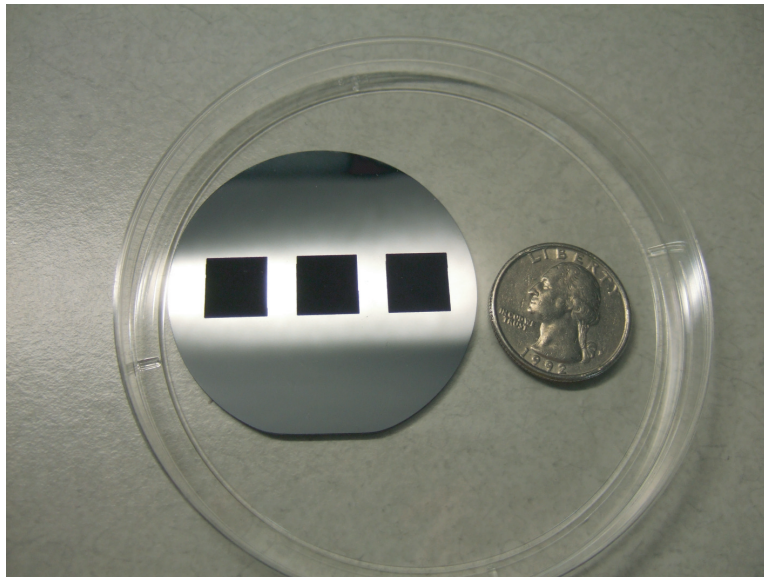


Figure 3.2: Photograph of  $1 \text{ cm}^2$  sized areas of silicon, nanostructured in an aqueous environment, using 400-nm femtosecond laser pulses.

The spot size of the laser is measured at the sample by placing a pickoff (held by a flip mount) in the beam path after the focusing lens, and a CCD camera is placed in this path. The CCD camera is positioned such that it and the sample are equidistant from the pickoff. With knowledge of the laser spot size (full width at half maximum, FWHM) at the sample, we can determine both the laser fluence at the sample, as well as the step size for the raster pattern of the translation stages. Because of the Gaussian nature of the laser beam, we typically set the raster pattern to step one half of the spot size during each pass. When using the scan mirror system, better sample uniformity results when we use a higher translation speed, and smaller step size. We can express this speed difference in terms of a multiplicative factor. To demonstrate the use of this multiplicative factor in calculating the scan speeds and step sizes, we will consider an example set of fabrication parameters. For example, if

our laser spot size at the sample is  $100\ \mu\text{m}$ , the repetition rate of the laser is 1 kHz, and we wish to deliver 500 pulses to each area of the sample, we would normally use a horizontal stage velocity of  $200\ \mu\text{m}\cdot\text{s}^{-1}$ , and a vertical step of  $50\ \mu\text{m}$ . Using the scan mirror system to obtain better uniformity, we would use a multiplicative factor of 128 (this factor was chosen empirically, considering the minimum step size and maximum linear velocity of the galvanometric scan mirror system). This multiplicative factor means that we would use a horizontal velocity of  $25.6\ \text{mm}\cdot\text{s}^{-1}$ , and a step size of  $0.391\ \mu\text{m}$ . These values are obtained by multiplying the horizontal speed and dividing the vertical step by the multiplicative factor. Due to the fact that the scan mirror pattern is not phase-locked to the 1 kHz laser pulse train, this multiplicative factor approach to fabricating samples effectively is randomly irradiating the silicon wafer with pulses such that each point on the surface is subjected to, on average, the same amount of laser energy. The difference in spatial uniformity of the samples is clearly evident when observing samples fabricated using different multiplicative factors under an optical microscope in a reflective brightfield configuration.

To render these nanostructured surfaces SERS-active, we thermally evaporate silver onto the structured silicon. Using a quartz crystal microbalance to measure the thickness of a planar continuous film, we fabricated substrates with 10 nm, 30 nm, 60 nm, 80 nm, 100 nm and 200 nm of deposited silver. All films were thermally evaporated at a rate of 0.15 nm per second, with no heating or cooling applied to the substrate during deposition. Figure 3.3 shows scanning electron microscope and helium ion microscope images of a substrate with 80 nm of silver deposited.

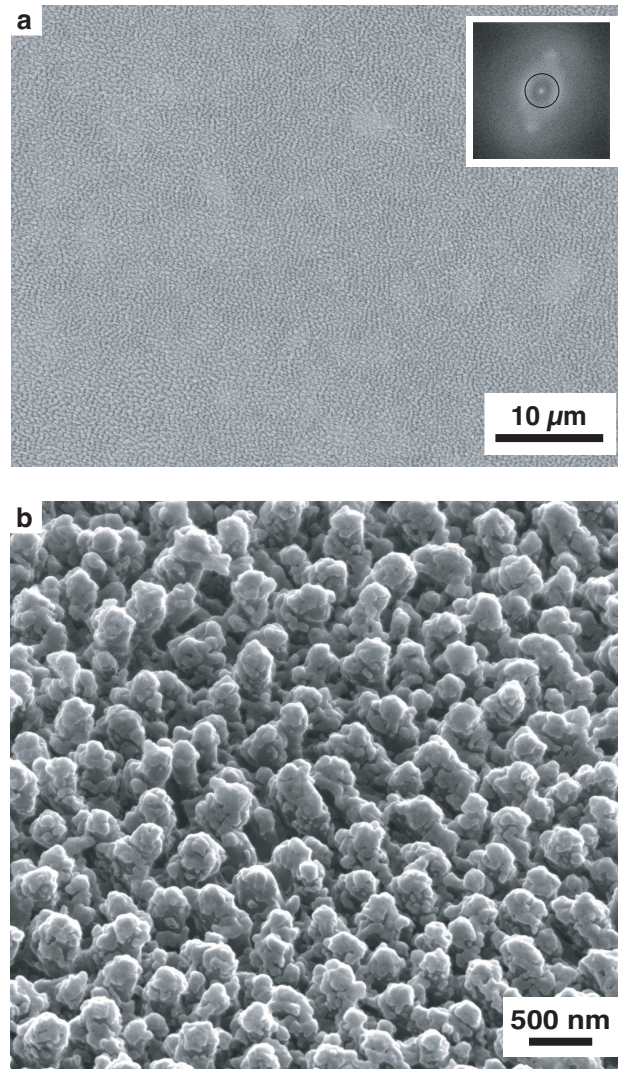


Figure 3.3: Scanning electron microscope (a) and helium ion microscope (b) images of the nanostructured substrate coated with 80 nm of silver. (a) Normal and (b) side ( $45^\circ$ ) views of the surface. Insets: (a) Fast Fourier transform (FFT) of the normal image. The black ring indicates the peak position in the FFT intensity, which corresponds to a spatial period of 505 nm. The author would like to note that these samples exhibit high aspect ratio features, and the helium ion microscope is a preferred tool, when compared with a standard scanning electron microscope, to obtain high resolution images at high sample tilt angles.

### 3.3.2 Raman spectroscopy measurements

Characterization of the Raman cross section enhancement factor of SERS substrates requires a careful quantification of several experimental factors. We are in-

interested in obtaining the ratio of two optical signals,  $I_{SERS}$  and  $I_{Raman}$ , normalized by the number of molecules contributing to each. The average Raman cross-section enhancement factor will thus be defined as

$$EF = \frac{I_{SERS} N_{Raman}}{I_{Raman} N_{SERS}} \quad (3.1)$$

where  $N_{SERS}$  and  $N_{Raman}$  are the number of molecules probed in the SERS and reference samples, respectively. In order to quantify the number of molecules probed in the SERS substrate case, we dose the laser-nanostructured substrates with a self-assembled monolayer (SAM) of either benzenethiol or mercaptobenzoic acid. To apply the SAMs, we submerge the silver-coated substrates in 4-mM solutions made with ethanol for 1 hr and gently rinse them in neat ethanol for 1 min, finally drying them under a stream of nitrogen. Reference samples of benzenethiol are made by placing a drop (approximately 20  $\mu\text{L}$ ) of the neat liquid between a glass microscope slide and a microscope coverslip. A 500- $\mu\text{m}$  thick silicone spacer is used to separate the two pieces of glass. Benzenethiol and mercaptobenzoic acid are chosen as analytes for the experiments discussed here as they are non-resonant with the Raman excitation sources used in this work, and readily form uniform self-assembled monolayers with known packing densities on clean silver surfaces.

Multiple Raman setups were used to characterize the SERS properties of these substrates in these experiments. Enhancement factor estimates as well as point-to-point variations in intensity over the patterned area were measured on a micro-Raman apparatus (upright optical microscope coupled to laser excitation sources and a dispersive CCD-based spectrometer). Using a 5-mW, s-polarized 632.8-nm HeNe laser, spectra were recorded through a 10 $\times$  microscope objective (0.25 NA) and projected onto a

thermo-electrically cooled CCD array using a 1200-gr/mm diffraction grating. Individual spectra were recorded from both single spots (approximately 1.6- $\mu\text{m}$  diameter) on the substrate, and from a 500- $\mu\text{m}$  thick cell of neat benzenethiol for normalization. The same apparatus was used to measure the SERS uniformity over a 500  $\mu\text{m} \times 600 \mu\text{m}$  area from points on the substrate spaced 5  $\mu\text{m}$  apart using a 0.5-s integration time per spectrum. Raman spectra were also collected using a second micro-Raman apparatus, which employed a 10-mW s-polarized 785-nm laser diode, 20 $\times$  microscope objective (0.40 NA), 1200-gr/mm diffraction grating, and thermo-electrically cooled CCD array. Additionally, Raman excitation profiling was accomplished using a tunable continuous-wave titanium:sapphire laser in a backscattering configuration. The incident beam was focused onto the sample through a 10-cm focal length lens to yield a spot size of approximately 20  $\mu\text{m}$  diameter. The incident laser wavelengths were varied from 700 – 900 nm in 5-nm increments with the power held constant at 15 mW, as measured at the sample. The SERS signal was collected through a triple monochromator and then recorded on a back illuminated, deep depletion CCD array. The excitation profile intensities for the 1075  $\text{cm}^{-1}$  mercaptobenzoic acid peak were corrected for instrument response using the nearby 1105  $\text{cm}^{-1}$  peak from the normal (unenhanced) Raman spectrum of 4-acetamidophenol taken under identical conditions.

### 3.4 Results

The laser-nanostructuring procedure results in a quasi-uniform distribution of raised features on the silicon surface. Although the cones protrude above the surface

of the silicon by as much as 1  $\mu\text{m}$ , the underlying silicon wafer is left intact and structurally unchanged [36]. After deposition of a silver thin film, the surface of the substrate is covered with highly non-uniform silver nanoparticles, whose dimensions are typically on the order of 50–100 nm, as observed in Figure 3.3(b). These silver particles provide an appropriate surface on which to form a self-assembled monolayer of either benzenethiol or mercaptobenzoic acid. We obtained the SERS spectra shown in Figure 3.4 from a benzenethiol self-assembled monolayer on a substrate coated with 80 nm of silver at two different excitation wavelengths (632.8 nm and 785 nm).

Spectra recorded under identical conditions from a region of the silicon wafer that was not laser structured (i.e. a flat silver substrate) result in no observable signal (data not shown). The SERS signal shows no discernable dependence on the sample orientation with respect to the excitation laser polarization. In both Figures 3.4(a) and 3.4(b), the absence of Raman peaks at  $917\text{ cm}^{-1}$  and  $2567\text{ cm}^{-1}$  (S-H in-plane bending and S-H stretching modes, respectively) indicates that a single monolayer of benzenethiol is adsorbed on the surface [37]. For comparison, unenhanced Raman spectra, obtained from a neat solution of benzenethiol in a glass cell, are also shown in Figures 3.4(a) and 3.4(b). Based on these data the average SERS cross-section enhancement factor for the  $1572\text{ cm}^{-1}$  normal mode is approximately  $2 \times 10^7$  and  $1 \times 10^6$  for 632.8 nm and 785 nm excitation, respectively. The SERS intensity depends on the amount of silver deposited on the structured silicon surface. Figure 3.5 shows the integrated intensity of the  $1572 \pm 10\text{ cm}^{-1}$  (C=C stretch) Raman band from a self-assembled monolayer of benzenethiol applied to different substrates with varying silver thicknesses. Each data point shown is the average of 10 randomly sampled

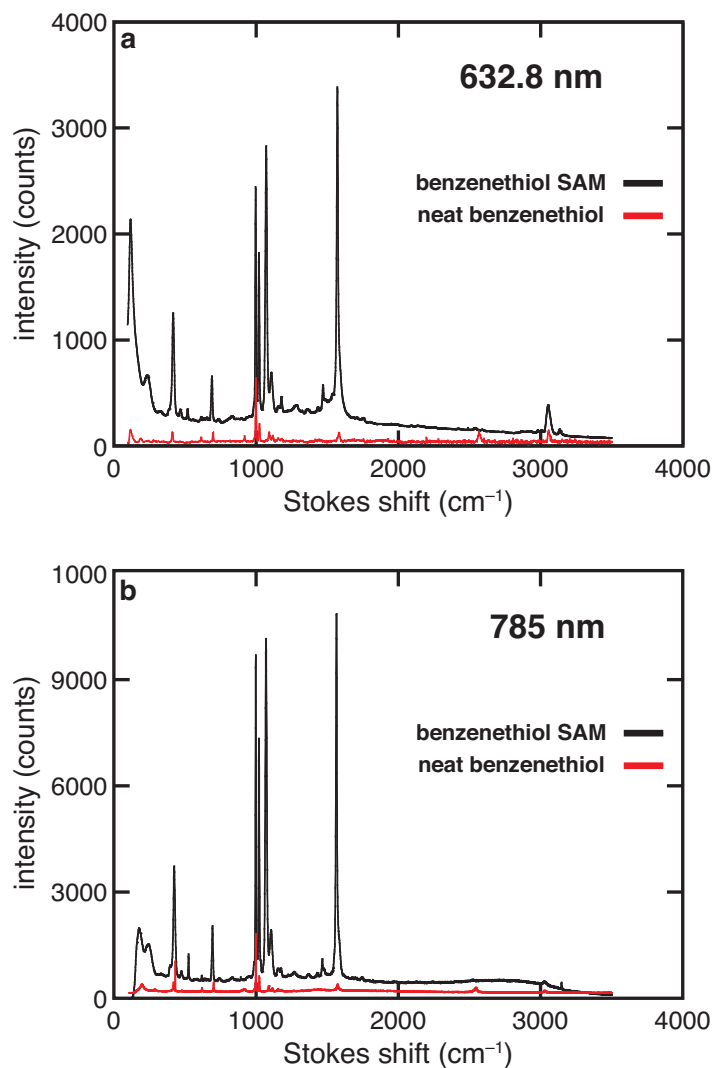


Figure 3.4: Raman spectra of benzenethiol taken with (a) 5-mW 632.8-nm excitation, and (b) 10-mW 785-nm excitation. The SERS spectra (black) in both (a) and (b) were taken from a self assembled monolayer adsorbed on a substrate with an 80-nm silver film applied. The corresponding unenhanced Raman spectra (red) of neat benzenethiol are shown for comparison. All spectra were recorded with an integration time of 1 second.

locations on each substrate. Under otherwise identical conditions, with 632.8 nm excitation and a  $10\times$  (0.25 NA) microscope objective, the SERS intensity is greatest for substrates with 80 nm of silver. The enhancement factor of the sample with an

80-nm film is roughly a factor of 2 greater than that of the samples with 10 nm and 200 nm thick films.

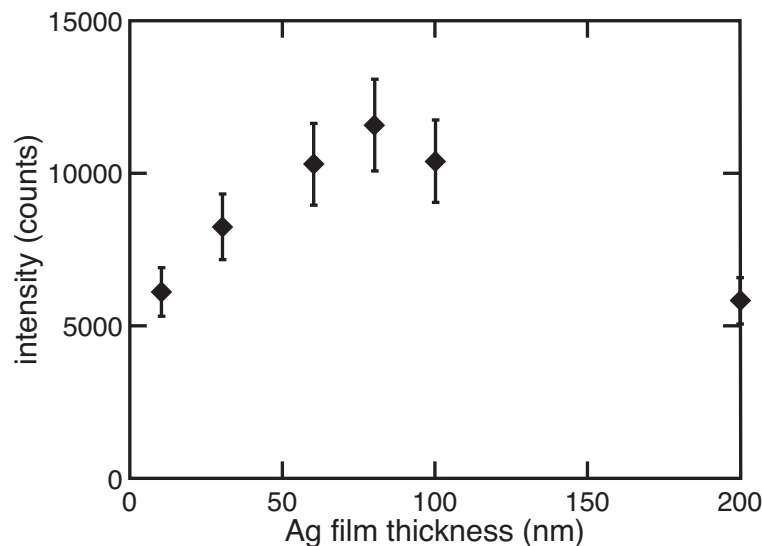


Figure 3.5: Dependence of the integrated intensity of the  $1572 \pm 10 \text{ cm}^{-1}$  band of benzenethiol on the deposited silver film thickness. The values shown are the average of the integrated Raman intensity collected with 5-mW 632.8-nm excitation for 1 second from 10 randomly chosen locations on each  $2 \text{ mm} \times 2 \text{ mm}$  sample.

We measured the uniformity of the SERS intensity over a large area of the substrate coated with 80 nm of silver using 632.8-nm excitation. We created a Raman map (Figure 3.6(a)) using the integrated intensity of the  $1572 \pm 10 \text{ cm}^{-1}$  Raman band of benzenethiol. The greatest deviation from the point of maximum signal is  $-4.3 \text{ dB}$ , with a standard deviation of 0.125 (map intensity normalized to its mean). This uniformity is reproducible from substrate-to-substrate, as demonstrated by the SERS signal intensities from 42 different samples. Using the same experimental setup, a single Raman spectrum was taken from a randomly chosen location on each  $2 \text{ mm} \times 2 \text{ mm}$  sample. The integrated intensity of the  $1572 \pm 10 \text{ cm}^{-1}$  band in these 42

spectra has a standard deviation of 0.129 (distribution normalized to its mean). Histograms of the intensities of both the SERS map and the 42 individual samples are shown in Figure 3.6(a) and 3.6(b). An F-test of the standard deviations of the two distributions indicates that their difference is not statistically significant ( $p = 0.88$ ).

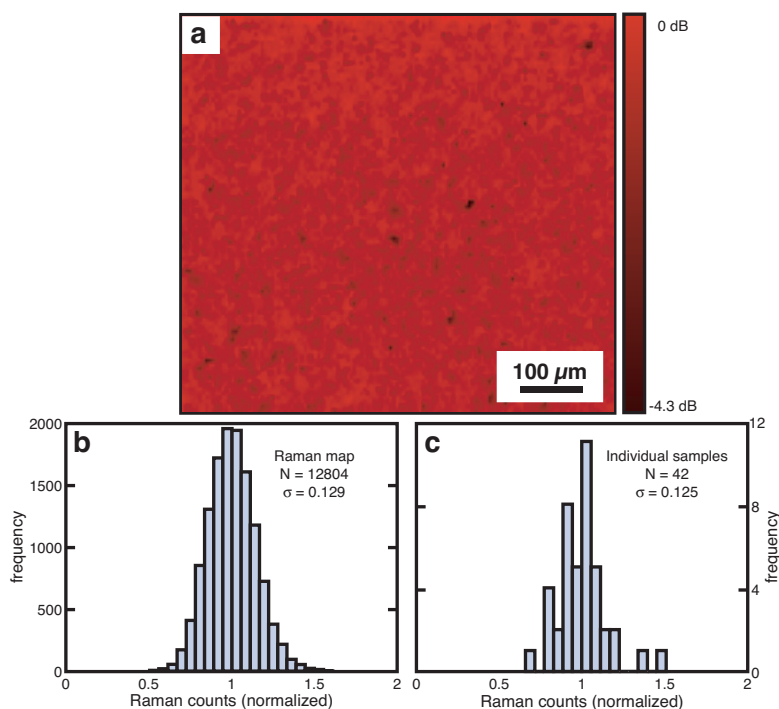


Figure 3.6: (a) Raman map of a  $500 \mu\text{m} \times 600 \mu\text{m}$  area of a substrate with an 80-nm silver film. The map is obtained from the integrated intensity of the  $1572 \pm 10 \text{ cm}^{-1}$  band of a benzenethiol self-assembled monolayer adsorbed on the substrate. Each point in the map was taken using 5-mW 632.8-nm excitation with a 0.5 s integration time. (b) Histogram of the intensity from the map shown in (a). (c) Histogram of the SERS intensities recorded from randomly chosen locations on 42 different  $2 \text{ mm} \times 2 \text{ mm}$  samples using 1 second integration times.

The SERS enhancement observed from these substrates is remarkably constant with respect to excitation wavelength. Figure 3.7 shows the integrated intensity of the  $1075 \text{ cm}^{-1}$  band of mercaptobenzoic acid over a range of excitation wavelengths using a substrate with an 80-nm silver film. A fast Fourier transform filter removed

high frequency noise and smoothed the data. Within the experimental excitation wavelength range (700–900 nm), the maximum SERS enhancement occurs near 750 nm. However, the maximum is not exceptionally pronounced, as the signal at 750 nm is only 30% greater than the signal at 850 nm.

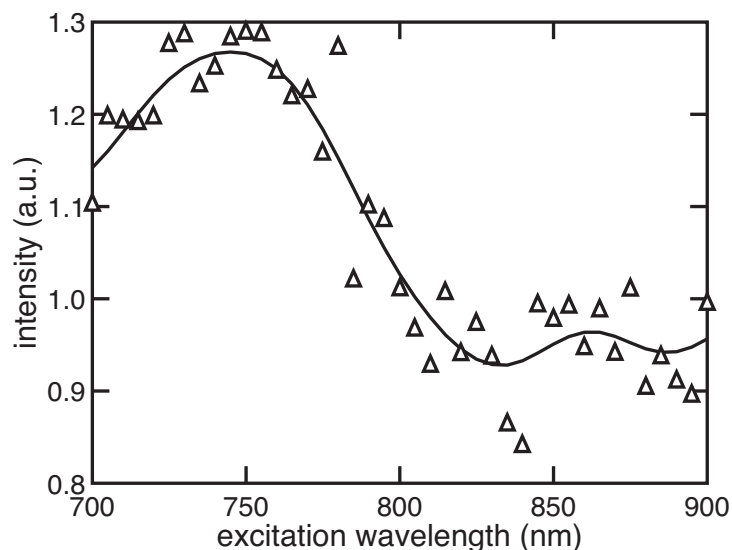


Figure 3.7: Relative integrated intensity of the  $1075 \pm 10 \text{ cm}^{-1}$  band of a mercaptobenzoic acid self-assembled monolayer deposited on a sample with an 80-nm silver coating, as a function of excitation wavelength. Spectra taken at each wavelength were collected with 15-mW excitation for an integration time of 2 min. The curve shown is a FFT smoothing of the data.

## 3.5 Discussion

### 3.5.1 SERS substrate morphology

The Fourier transform of the image in Figure 3.3(a) shows a peak in the spatial frequencies of the substrate, which corresponds to a period of 505 nm. The higher frequency lobes in the FFT image correspond to the shapes of the cones themselves,

as their angular position in the FFT is dependent on the rotational orientation of the sample. From this analysis, we deem these substrates a quasi-ordered array of cones that cover the surface. This periodicity can be explained in terms of a capillary wave resolidification process. Since the femtosecond laser pulse intensity at the silicon surface is on the order of  $10^{12}$  W/cm<sup>2</sup>, the interaction of the laser pulse with the surface is highly modified compared to interactions involving lower intensities. At these high intensities, the electron-hole plasma generated in the first few nanometers by linear absorption of the leading portion of the laser pulse is so dense that it acts as a reflecting surface to the trailing portion of the laser pulse [38]. Because the 200 fs pulse is significantly shorter than the electron-phonon thermalization time (on the order of 1 ps) [39, 40], the plasma generated in this thin layer does not have a chance to dissipate its energy into the silicon lattice before the transient laser pulse is gone. This effect results in a plasma-induced melting of a surface layer thinner than the skin depth of silicon at that wavelength (82 nm at  $\lambda = 400$  nm [41]) [42]. When the electrons do thermalize by coupling to phonons in the lattice, it results in the rapid melting of only the thin layer, while the underlying silicon substrate remains in the solid phase. Due to the picosecond timescale of this melting process, the resulting thermal gradients are much larger than in the case of nanosecond laser melting of silicon, for example. We can describe the heat flow from this molten silicon layer to the surrounding environment using the differential form of Fourier's 1-D heat conduction equation,

$$\vec{q} = -k \frac{dT}{dx} \quad (3.2)$$

where  $q$  is the heat flux in the  $x$ -direction,  $T$  is the temperature at a given position  $x$ , and  $k$  is the thermal conductivity. We see that heat flux is proportional to both the negative of the temperature gradient and the thermal conductivity. Since the laser pulse energy is deposited completely within this thin molten silicon layer, the boundary between liquid and solid silicon has an extreme temperature gradient, which enables fast cooling and resolidification of the molten silicon. To further enhance the cooling rate of the molten silicon layer, we perform the laser nanostructuring process in a water environment, as water has a much higher thermal conductivity than most gases [43].

In a thin liquid layer on top of a solid substrate, shallow capillary waves can be excited. These waves are a result of fluctuations in the surface tension of the liquid, which follow the dispersion relation [44]

$$\tau_{liq.}^2 k^4 = \frac{(2\pi)^2 \rho}{\sigma d} \quad (3.3)$$

where  $\tau_{liq.}$  is the lifetime of the molten layer,  $k$  is the wavevector ( $2\pi/\lambda$ ) of the capillary wave,  $\rho$  is the density of the molten silicon,  $\sigma$  is the surface tension of the molten silicon, and  $d$  is the melt depth. By approximating the density and surface tension of molten silicon using their literature values near the melting temperature of silicon, and using melt depths in the range of 10-100nm and a capillary wavelength of 505 nm, the lifetime of the molten silicon layer can be extracted to be on the order of 5 to 10 ns. This result, although somewhat qualitative, follows in agreement with lifetimes calculated from femtosecond laser structured surfaces fabricated in gaseous environments. A gaseous environment provides a lower heat conductivity than water, and correspondingly capillary wavelengths approximately an order of

magnitude longer are observed [45]. Experiments using nanosecond laser pulses to structure the surface of silicon wafers also exhibit even larger quasi-periodic features, as a result of heat diffusion into the bulk during the laser pulse. This diffusion of heat on nanosecond time scales creates a smaller thermal gradient than in the femtosecond case, and thus a larger melt depth and longer capillary wavelengths [46].

It should be noted, that after several laser pulses, these quasi-periodic silicon surfaces, which have been frozen into place after each individual laser pulse, will affect the distribution of optical energy at the surface during future pulses. These periodic modulations in the surface height can cause non-uniform optical field distributions through diffraction, refraction, and self-interference of the laser pulses, which generate non-homogenous heating of the surface. Additionally, laser ablation during this process influences the final surface morphology, but we ignore this effect here to focus on the origin of the surface periodicity. By no means is the model we have described here complete; we have simply outlined the basic phenomenon by which these quasi-periodic structures form under repeated femtosecond laser irradiation.

Previous measurements on these surfaces using X-ray photoelectron spectroscopy reveals that the cones are covered by a thin layer of SiO<sub>2</sub> [36]. This layer has roughness on the order of tens of nanometers [36, 46] and enables a unique thin film deposition process that is responsible for the SERS properties observed in these samples. The rough surface acts as a physical catalyst for silver particle formation by enabling a reduction of the silver/SiO<sub>2</sub> interfacial surface energy during the deposition process [47]. Instead of the smooth continuous film that results during metal film deposition on flat surfaces, we observe discontinuous, particulate film deposition on the nanostruc-

tured silicon substrates. As shown in Figure 3.3(b), the deposited silver does not form a continuous film, but rather a collection of aggregated particles — an architecture which is generally accepted to greatly enhance Raman signals from molecules nearby or adsorbed to the surface [48–51].

### 3.5.2 Calculation of the SERS enhancement factor

The Raman scattering cross-section enhancement factor for the substrate is determined from Equation 3.1, where  $I_{SERS}$  and  $I_{Raman}$  are the integrated intensities of a specific Raman band, normalized to the incident laser photon flux for the cases of the SERS substrate with the self-assembled monolayer applied and the neat molecular dye, respectively. Additionally, the integration of these Raman intensities must not include any background signals that may be present in the spectrum, due to stray light, noise, or sample fluorescence (*i.e.* background correction is applied to each spectrum before taking the integral of the Raman bands). Proper enhancement factor calculations must also account for the number of probed molecules,  $N_{SERS}$  and  $N_{Raman}$ , in each sample. For  $N_{SERS}$ , the benzenethiol self-assembled monolayer density ( $6.8 \times 10^{14} \text{ cm}^{-2}$ ) and the laser spot size give an estimate of the maximum number of molecules on a planar surface that can contribute to the SERS signal [52]. However, the surface of the substrates is not planar, and the effective benzenethiol SAM density must be adjusted by a surface area enhancement factor, which takes into account the morphology of the substrates. The simplest geometric model of the surface is to assume an array of silicon cones with an average period of about 500 nm, as shown in Figure 3.8.

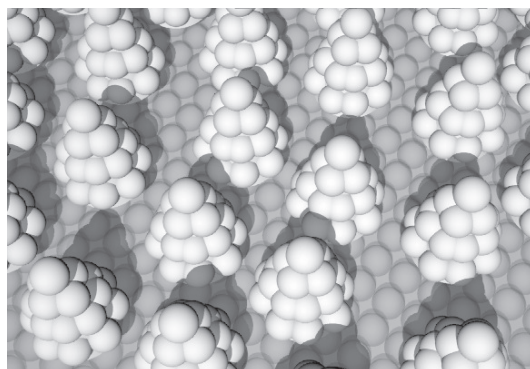


Figure 3.8: Cartoon schematic of the model used to estimate the surface area enhancement of the laser-nanostructured substrates.

The surface is modeled as a quasi-ordered array of cones [53] covered with a layer of spherical silver particles, whose total cross-sectional area is equivalent to the surface area of the cones. This geometrical model results in a surface area enhancement of approximately 10. We have also made attempts to directly measure the surface area enhancement of the substrate using several experimental techniques, such as UV reflectance confocal microscopy and atomic force microscopy using special high aspect ratio probes. Due to the high aspect ratio of the samples combined with their nanoscale lateral dimensions, both of these techniques proves to be extremely difficult and unreliable to obtain accurate results. This aspect of the project is still in need of a good solution, such that a truly accurate measurement of the SERS enhancement factor can be determined. The number of probed molecules in the un-enhanced sample of neat benzenethiol,  $N_{Raman}$ , is approximated using the molecular weight and density of benzenethiol and the effective interaction volume of the Gaussian laser beam with the neat benzenethiol sample. The confocal nature of the micro-Raman spectrometer is incorporated in the determination of  $N_{Raman}$  by accounting for the axial collection efficiency of the microscope, which was rigorously measured using

standard procedures [54,55]. We will outline the measurement procedure here, but the author particularly recommends the supplemental information section in Ref. [54] as a guide to characterizing a confocal Raman microscope for quantitative enhancement factor measurements.

To summarize the results of Ref. [54], the effective scattering volume of the confocal microscope must be obtained through experimental measurement of the coupled spatial excitation and collection efficiencies. Since the focused Gaussian excitation laser beam does not have constant excitation intensity or collection efficiency versus the axial coordinate,  $z$ , or the radial coordinate,  $\rho$ , we must account for these non-uniformities in terms of an effective scattering volume, in order to determine  $N_{Raman}$ . The signal measured using a confocal Raman microscope from a bulk reference sample in space can be expressed as [54]:

$$I_{total} = cN_a\sigma_R \int_{\rho=0}^{\rho=\infty} 2\pi\rho \int_{z=-\infty}^{z=\infty} I(\rho, z)\eta(\rho, z)d\rho dz \quad (3.4)$$

where  $I_{total}$  is the total Raman signal measured,  $c$  is the concentration of analyte molecules in the sample,  $N_a$  is Avagadro's number,  $\sigma_R$  is the Raman cross section of the analyte molecule. Without knowledge of these intensity and collection efficiency functions  $I(\rho, z)$  and  $\eta(\rho, z)$  explicitly, we must experimentally determine the values of these integrals. We can transform this integral into the product of the molecular number density, Raman cross section, and effective scattering volume  $V_{eff}$  (a product of an effective height  $H_{eff}$  and an effective area  $A_{eff}$ ) that has unity excitation intensity and collection efficiency functions across its entire extent:

$$V_{eff} = H_{eff}A_{eff} = \int_{\rho=0}^{\rho=\infty} 2\pi\rho \int_{z=-\infty}^{z=\infty} \frac{I(\rho, z)}{I_0} \frac{\eta(\rho, z)}{\eta_0} d\rho dz. \quad (3.5)$$

$I_0$  and  $\eta_0$ , in this case, are the maximum values of  $I(\rho, z)$  and  $\eta(\rho, z)$ , such that each efficiency function is normalized to a peak excitation and collection efficiency of unity. A measurement of the radial intensity distribution can be used to determine the effective excitation area,  $A_{eff}$ . From Gaussian beam theory [56], it can be shown that this effective area can be expressed as the ratio of the beam's average power to its intensity at the origin:

$$A_{eff} = \frac{P}{I(0,0)} = \frac{\pi w_0^2}{2} \quad (3.6)$$

where  $w_0$  is the beam waist at  $z = 0$ . This beam waist can be measured experimentally, by scanning the Raman excitation laser over the edge of a cleaved silicon wafer. By fitting data points from silicon's  $520 \text{ cm}^{-1}$  Raman band intensity versus linear position  $x$  to the function

$$I(x) = A + \frac{I_{max}}{2} \left[ 1 + \operatorname{erf} \left( \frac{\sqrt{2}(x_0 - x)}{w_0} \right) \right], \quad (3.7)$$

we can determine  $w_0$ , where  $A$  is a constant offset,  $I(x)$  is the measured Raman signal versus position,  $I_{max}$  is the peak signal measured, and  $\operatorname{erf}(x)$  is the error function. For example, data obtained from this measurement using 785-nm excitation and a 0.40 NA microscope objective is shown in Figure 3.9.

To calculate  $H_{eff}$ , we can measure the axial collection efficiency,  $\eta(\rho, z)$ , of the microscope by measuring the Raman intensity of the  $520 \text{ cm}^{-1}$  band from a silicon wafer as a function of the axial coordinate  $z$ . If the entrance slit to the spectrometer is open wide enough to avoid any clipping of the imaged excitation area at all values of  $z$ , the  $\rho$  dependence in  $\eta(\rho, z)$  can be ignored, and the collection efficiency becomes

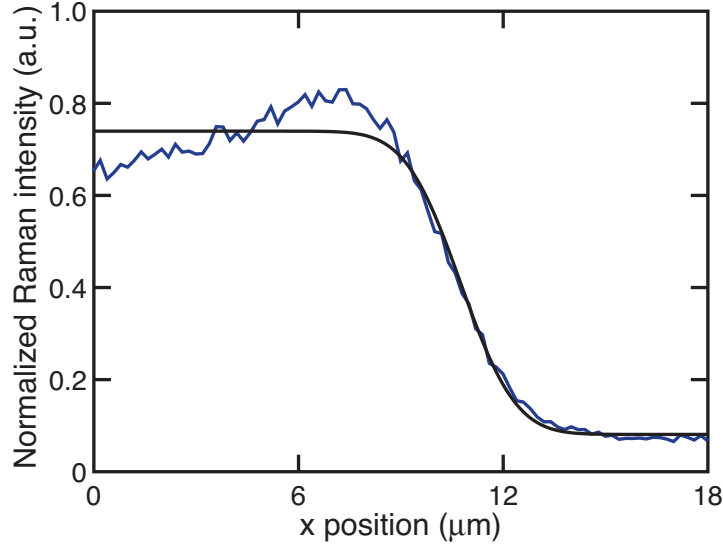


Figure 3.9: Experimental determination of the beam waist,  $\omega_0$  using the knife-edge method. The fit of this particular data yields a waist  $w_0$  of  $2.55\mu\text{m}$  for 785-nm excitation through a 0.40 NA microscope objective lens.

purely a function of  $z$ . The effective height of the scattering volume is defined as

$$H_{eff} = \int_{z=-\infty}^{z=\infty} \frac{\eta(z)}{\eta_0} dz. \quad (3.8)$$

Example data from this type of measurement of  $\eta(z)$  is shown in Figure 3.10. By taking the integral of this function normalized to its peak value  $\eta_0$ , we can find the total effective scattering height.

When calculating the enhancement factor for these substrates, we assume that all molecules on the surface Raman scatter with equal efficiency. However, nanoparticle SERS studies have shown that the relatively few molecules residing in the hot spots between particles contribute predominantly to the SERS signal [33,57]. This observation suggests that these nanostructured substrates exhibit small regions of enormous Raman enhancement, with the average surface enhancement factor being on the order of  $10^7$  (the focused 632.8-nm laser's beam waist of approximately  $1.6\mu\text{m}$  is large

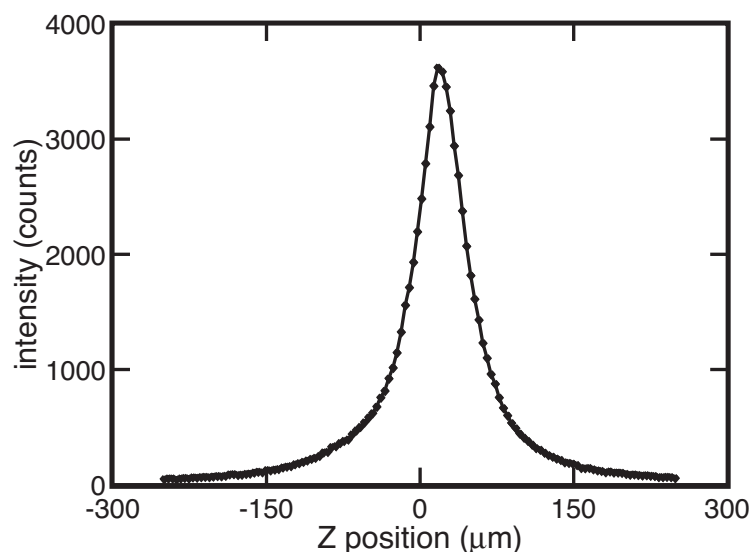


Figure 3.10: Typical axial collection efficiency function of the confocal Raman microscope using a 0.40 NA objective lens and 785-nm laser excitation.

enough to generate intense Raman scattering from many hot spots at once, considering the surface features' size and spacing). This enhancement factor is believed to be sufficient to observe single-molecule SERS using modern Raman spectrometers [54].

### 3.5.3 Silver deposition

Thin film deposition of silver on  $\text{SiO}_2$  substrates presents numerous opportunities from which to control the morphology of the resulting films, and by extension, the resulting SERS activity. Deposition parameters such as substrate temperature, deposition rate, and vacuum pressure can be used to alter a variety of thin film properties (i.e. thickness, grain size, and surface roughness). Keeping other parameters constant, we optimized the signal from these nanostructured substrates by varying the amount (thickness) of deposited silver. Silver is known to follow Volmer-Weber growth processes on oxide surfaces resulting in small silver clusters that grow into

islands on the surface [58]. The deposited film thickness determines the density and size of the silver particles formed on the surface. It should be noted, no special deposition requirements are necessary to generate particles with SERS relevant dimensions (50–100 nm) on the nanostructured substrates, even at film thicknesses that would normally cross far above the percolation threshold to form a continuous silver film on a planar SiO<sub>2</sub> substrate [59]. As shown in Figure 3.5, an 80-nm film of silver creates an optimal distribution of particles on the surface for 632.8-nm excitation. Plasmon resonances of these particle aggregates result in large local field enhancements and thus large SERS signals from adsorbed molecules. The dependence on silver thickness can be explained based on the particulate nature of the silver films: too little deposited silver results in a surface sparsely covered with isolated particles, and a corresponding decrease in SERS signal. Additionally, too much deposited silver forms a near-continuous film on the surface, covering the nanoscale features of the silicon substrate, leading to a decreased SERS signal.

### 3.5.4 Substrate uniformity

In addition to the large enhancement factors observed using these substrates, the SERS signal measured over a large area of a single substrate (Figure 3.6(b)), as well as the signal measured from substrate to substrate (Figure 3.6(c)) is extremely uniform. Statistical analysis of these data indicates that large substrates can be reproducibly fabricated in mass quantities. The uniformity of these substrates is largely a function of the laser fabrication process used to produce the nanostructured surface. During fabrication, the focused femtosecond laser beam (FWHM = 80  $\mu\text{m}$ ) used to structure

the silicon is rastered across the surface with enough overlap between subsequent passes ( $40\ \mu\text{m}$ ) to create a uniformly patterned substrate with no unexposed silicon surfaces, if raster scanning the sample with respect to the laser beam. If using the galvanometric scan mirror system, the uniformity is further improved. The typical spot sizes of the continuous wave lasers ( $632.8\ \text{nm}$  and  $785\ \text{nm}$ ) used to measure SERS signals from these substrates are significantly smaller ( $< 5\ \mu\text{m}$ ) than the structuring laser spot size. The uniform SERS intensities observed in this work using high spatial resolution Raman microscopes implies that the SERS enhancement is free from any spatial periodicity due to the finite size of the structuring laser's beam. We expect the SERS enhancement of these substrates to maintain this level of uniformity over any macroscopic distance, assuming the structuring laser output and silver deposition conditions are consistent across the entire structured area. In principle, these substrates are limited only by the size of the silicon wafer, the travel of the translation stages or size of the scan mirror system's scan field, and the size of the evaporator used to deposit the silver film.

### 3.5.5 Excitation profiling

The broad range of excitation wavelengths over which these nanostructured substrates provide significant enhancement affords great flexibility for use with a wide range of laser excitation sources for SERS or surface enhanced resonance Raman spectroscopy (SERRS). The position and width of the peak in the excitation profile shown in Figure 3.7 indicates there is an optimal excitation wavelength within the probed range. However, the relatively featureless nature of the excitation profile implies that

the substrates may be suitable for operation over a much broader range of excitation wavelengths than probed in this measurement. The enhancement factor at 632.8 nm is more than an order of magnitude greater than the enhancement factor at 785 nm. This difference illustrates that the maximum in the excitation profile is merely a local maximum within the probed wavelength range. This maximum in the near infrared portion of the spectrum is consistent with the typical spectral position of a surface plasmon resonance of aggregated silver nanoparticles [19, 52, 60]. In general, aggregation of silver nanoparticles not only red shifts their surface plasmon resonance, but also broadens this resonance over much of the visible range [61]. This broadening may be responsible for the SERS enhancement observed over the wide range of excitation energies used with these substrates. This broadband operation allows high-frequency (greater than  $3000\text{ cm}^{-1}$ ) Raman bands to be easily observed in SERS spectra without the typical decrease in intensity seen in many SERS substrates [32] (e.g. Figure 3.4(a). In Figure 3.4(b), taken with 785-nm excitation, the measured intensity of the Raman bands at frequencies greater than  $3000\text{ cm}^{-1}$  are limited by the efficiency of the silicon-based CCD detector).

### 3.5.6 Substrate temporal stability

The substrates are stable over long periods of time. We formed mercaptobenzoic acid monolayers on pristine substrates 3 months after initial substrate fabrication, and found no noticeable loss in SERS signal relative to mercaptobenzoic acid monolayers formed on freshly fabricated substrates. Once formed, the monolayers are extremely stable, as their SERS signals remain constant over a period of several months. The

stability of the Raman signal is most likely a function of both the unique mechanical stability innate to these nanostructured substrates as well as the molecular composition of the self-assembled monolayer itself. We chose benzenethiol and mercaptobenzoic acid as SERS reporter molecules as they are known to effectively bind to the silver substrate via thiol moieties [62]. The robust nature of these substrates makes them well suited for integration with highly sensitive spectroscopic devices over long periods of service with little degradation in performance.

## 3.6 Conclusion

In summary, we have presented a simple two-step process for fabricating silicon-based SERS substrates. We described the basic physics and characteristics of the physical formation mechanisms. We outlined the procedure for quantitatively determining the SERS enhancement factor, by characterizing the confocal Raman microscope scattering volume. We have measured the SERS enhancement of these substrates as a function of fabrication parameters, excitation wavelength, as well as the spatial and sample-to-sample SERS signal uniformity. These substrates exhibit extremely large and uniform Raman scattering cross-section enhancement factors over macroscopic areas. The enhancement factor of the substrates depends on the deposited silver film thickness; this parameter determines the spacing and density of silver particles formed on the nanostructured silicon surface. The substrates have an excitation wavelength dependence that is quite flat over the near-infrared range, making them compatible with numerous laser excitation sources. The excellent spatial uniformity, large SERS enhancement, structural stability, and simple fabrication make

these substrates attractive candidates for use in large-area trace detection schemes using Raman spectroscopy.

### **3.7 Acknowledgements**

This work described in this Chapter was primarily supported by the Army Research Office, under contract #'s N00014-03-M-0325 and W911NF-05-1-0341. Portions of this work were done in collaboration with Stephen Doorn and Nathan Mack at Los Alamos National Laboratory. We would also like to thank Horiba Jobin Yvon and X. Sunney Xie for use of their labs' facilities in the earlier phases of this research project.

# Chapter 4

## Isolating SERS hot spots using multiphoton lithography

### 4.1 Abstract

In this chapter, we present a method for improving femtomole-level trace detection ( $10^9$  molecules) using the large-area surface-enhanced Raman scattering (SERS) substrates described in Chapter 3, although this process should be useful for most all SERS substrates based on noble metals. Using multiphoton-induced exposure of a commercial photoresist, we physically limit the available molecular adsorption sites to only the electromagnetic "hot spots" on the substrate. This process prevents molecules from adsorbing to sites of weak SERS enhancement, while permitting adsorption to sites of extraordinary Raman enhancement. For a randomly-adsorbed sub-monolayer of benzenethiol molecules the average Raman scattering cross-section of the processed sample is 27 times larger than that of an unprocessed SERS substrate.

Much of the text in this Chapter is adopted from Ref. [63].

## 4.2 Introduction

Molecular adsorption sites on macroscopic SERS substrates exhibit a high variance in Raman enhancement factors [33]. As a direct consequence of this broad distribution, molecules adsorbed to the extremely small fraction of sites of extraordinary SERS enhancement ( $>10^9$ ) contribute a large percentage of the total Raman signal measured. Random site adsorption over this distribution poses a problem for reliably measuring SERS signals from a number of molecules that form less than a monolayer of surface coverage. In this Chapter, we present a method for isolating hot spots on large area ( $>25 \text{ mm}^2$ ) SERS substrates. We use multiphoton-induced exposure of a commercial photoresist on the substrate to uncover only the electromagnetic hot spots. The electromagnetic enhancement at SERS hot spots and the intensity-dependent nature of multiphoton absorption cause preferential isolated exposure of the photoresist at the hot spots. Removal of the exposed photoresist then yields a substrate for which only hot spots are available as adsorption sites. This process does not require prior knowledge of the location or SERS enhancement of hot spots. Compared to a randomly adsorbed sub-monolayer of analyte molecules on an unprocessed SERS substrate, the same number of molecules adsorbed on isolated hot spots exhibits a 27-fold improvement in average Raman scattering cross-section.

### 4.3 Experimental

The macroscopic SERS substrates used in this work are fabricated using a femtosecond laser-nanostructuring process described in Chapter 3. The resulting substrate surface is comprised of a quasi-ordered array of cones with an average period of 500 nm, as shown on the left of Figure 4.1. The cones are covered with aggregates of silver nanoparticles, formed by thermal deposition. These substrates offer a spatially uniform and large ( $>10^6$ ) average SERS enhancement factor over the visible and near infrared spectral regions. The hot spot isolation (HSI) process is depicted on the right in Figure 4.1. Positive-tone photoresist (Shipley S1805, MicroChem) is diluted 10:1 in resist thinner (Shipley Thinner-P, MicroChem) and spun onto the substrate at 3000 rpm for 1 minute. On a flat silver-coated silicon wafer, this spin speed yields a 30-nm thick layer after a soft bake (120 °C, 1 min). This layer of photoresist prevents analyte molecules from adsorbing to the silver surface of the SERS substrate. We use galvanometric scan mirrors to subject each point on the substrate to one hundred pulses from a regeneratively-amplified titanium:sapphire femtosecond laser system ( $\tau = 60$  fs,  $\lambda_{\text{center}} = 795$  nm, 100-kHz repetition rate). The laser pulses are focused by a single lens placed before the scan mirrors to achieve fluences at the substrate in the range of 0-400 J/m<sup>2</sup>. After fs-laser exposure, a commercial aqueous alkaline developer (Shipley CD-30, MicroChem) is used to remove the exposed photoresist covering the hot spots.

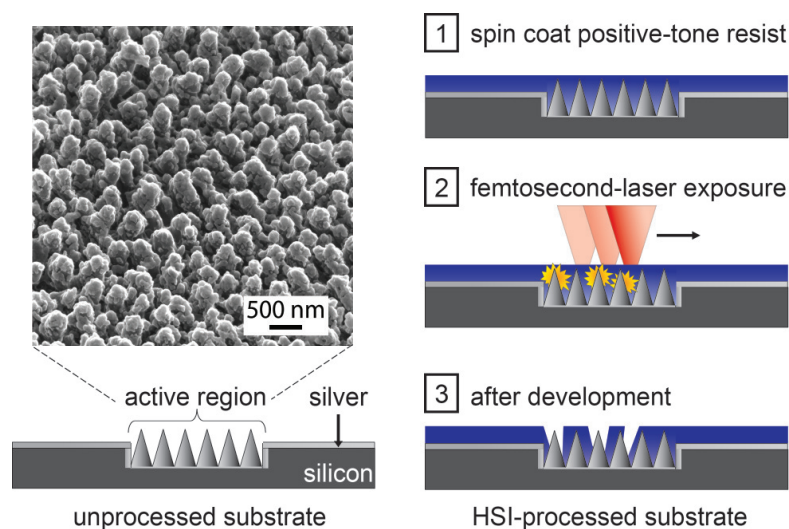


Figure 4.1: Helium ion microscope image ( $45^\circ$ ) and schematic diagram of SERS substrate (left). Hot spot isolation (HSI) process (right): (1) Diluted positive-tone photoresist is spin-coated onto a SERS substrate to cover the surface. (2) A femtosecond laser pulse train is scanned over the surface, selectively exposing the photoresist covering electromagnetic hot spots. (3) The photoresist is developed and the SERS hot spots are uncovered.

## 4.4 Results

To test the improvement of trace detection due to the HSI process, we dosed both an unprocessed SERS substrate and HSI-processed substrates processed at various exposure fluences with a sub-monolayer of benzenethiol molecules. We chose benzenethiol as a test molecule because it has a large non-resonant Raman cross-section, and a strong binding affinity to silver. To ensure sub-monolayer analyte coverage, we incubated each of the substrates in 4 mL of a 1-pM concentration solution of benzenethiol in ethanol (4 femtomoles of benzenethiol) for 24 hours. Considering the dimensions of the substrate and the packing density of benzenethiol on a silver surface [52], this dosage ( $2.4 \times 10^9$ ) represents a surface coverage of approximately 0.001% on the unprocessed sample. We performed micro-Raman spectroscopy on

all substrates using 12 mW of 785-nm excitation through a 0.40-NA microscope objective with an integration time of 30 seconds. We measured the full width at half maximum of the 785-nm laser spot to be 4.2  $\mu\text{m}$ . For each sample we measured the integrated signal-to-baseline intensity of the 998- $\text{cm}^{-1}$  ring-breathing mode of benzenethiol at 10 random locations. The average integrated intensity of the 998- $\text{cm}^{-1}$  ring-breathing mode of benzenethiol from these spectra is shown in Figure 4.2. The average and standard deviations of these values is also shown in 4.2. The unprocessed sample's average integrated intensity is plotted as a dashed line, with the gray area representing the standard deviation of the distribution. We find that exposure of the photoresist using a fluence of 200  $\text{J}/\text{m}^2$  improves the signal intensity relative to the unprocessed substrate by a factor of 27. To illustrate this improvement, averaged spectra obtained from the sample processed at 200  $\text{J}/\text{m}^2$  and the unprocessed sample are shown in 4.3.

## 4.5 Discussion

Qualitatively, the trend of the data shown in 4.2 can be understood as follows. A resist covered sample that has not been exposed to fs-laser pulses exhibits no discernible benzenethiol SERS signal; the molecules are unable to adsorb to the silver surface covered by the photoresist. At low fluences, not enough hot spots are uncovered to generate large signals. At intermediate fluences, we record large improvements in signal relative to the unprocessed sample. Finally, at high fluence values, the photoresist covering areas of weaker enhancement is also exposed and the signal improvement declines, with signal levels approaching those of the unprocessed

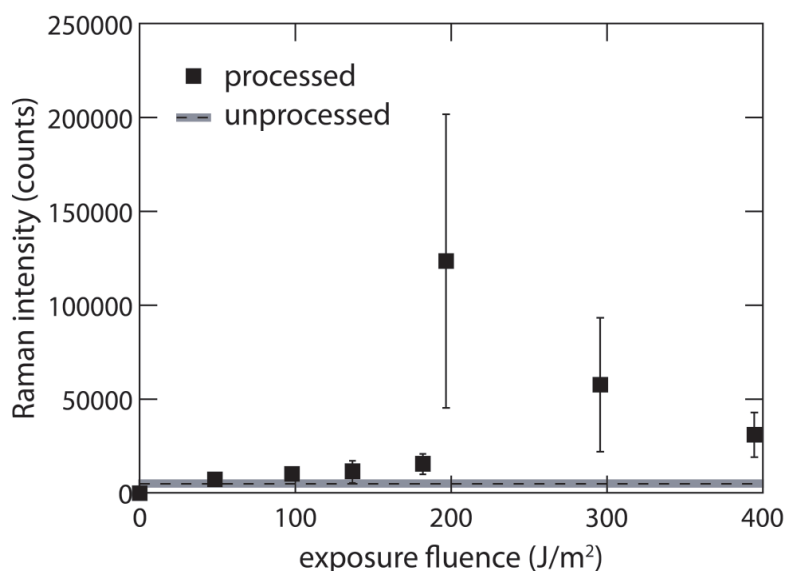


Figure 4.2: SERS signal as a function of exposure fluence. The average signal from the unprocessed sample is represented as the dashed line, with the standard deviations represented by the gray area. Error bars for the first 3 samples are smaller than the data marker. All data points are obtained by integrating the intensity of the  $998\text{ cm}^{-1}$  Raman band of benzenethiol recorded at 10 random locations on each substrate. The signal from the sample processed using an exposure fluence of  $200\text{ J/m}^2$  is 27 times larger than that of the unprocessed sample.

sample.

Given that our photoresist is optimized for G-line exposure (436 nm) and that our exposure laser wavelength is 795 nm, we attribute the selective photoresist exposure to multiphoton-induced luminescence from an interband electronic transition in silver [27]. The overlap of the luminescence spectrum and the absorption band of the photoresist enables its exposure. We rule out that harmonic generation at hot spots plays a significant role in the HSI process as the spectrum of the scattered light in our experiment shows that luminescence from the silver is orders of magnitude more intense. The absorption spectrum of the photoresist and the multiphoton-induced luminescence spectrum of the substrates is shown in Figure 4.4. Additionally, previous

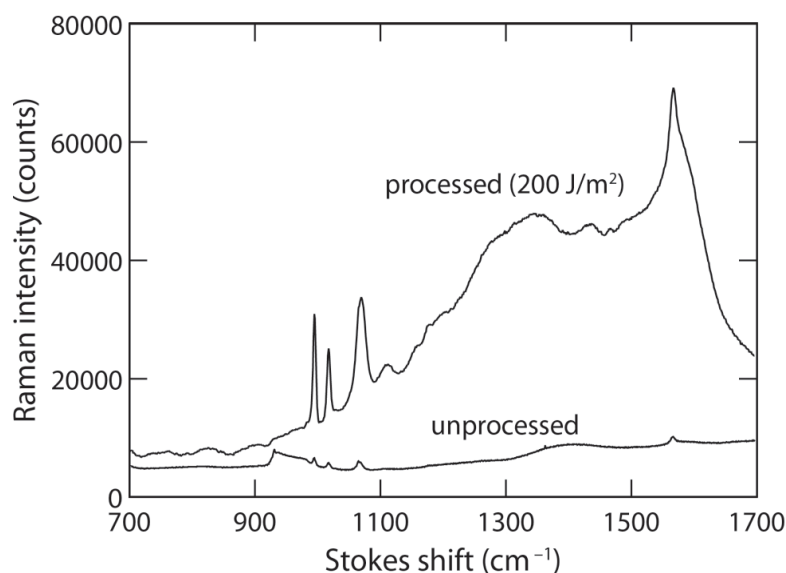


Figure 4.3: Comparison of Raman spectra from HSI-processed and unprocessed samples incubated with 4 femtomoles of benzenethiol. Each trace is the average of 10 spectra taken from the 200 J/m<sup>2</sup> and unprocessed sample. No baseline correction is applied to either spectrum; the background in the HSI spectrum is due to C-H vibrations in the undeveloped photoresist.

studies of polymerization using ultrafast optical excitation of metallic nanoparticle aggregates have ruled out field-enhanced multiphoton absorption in the photoresist as a dominant exposure mechanism [64]. Finally, we conclude that this effect is both intensity-dependent and non-thermal in nature, as no HSI is observed if the process is performed using comparable continuous-wave excitation. For these reasons, we attribute the selective exposure of the photoresist to multiphoton-induced luminescence, which is expected to be greatest near hot spots, due to its intensity-dependent nature.

Several factors influence the improvement obtained with the HSI process. Firstly, the spatial distribution of hot spots in metallic nanoparticle aggregates depends strongly on the excitation frequency [23,24]. Therefore, the Raman excitation wave-

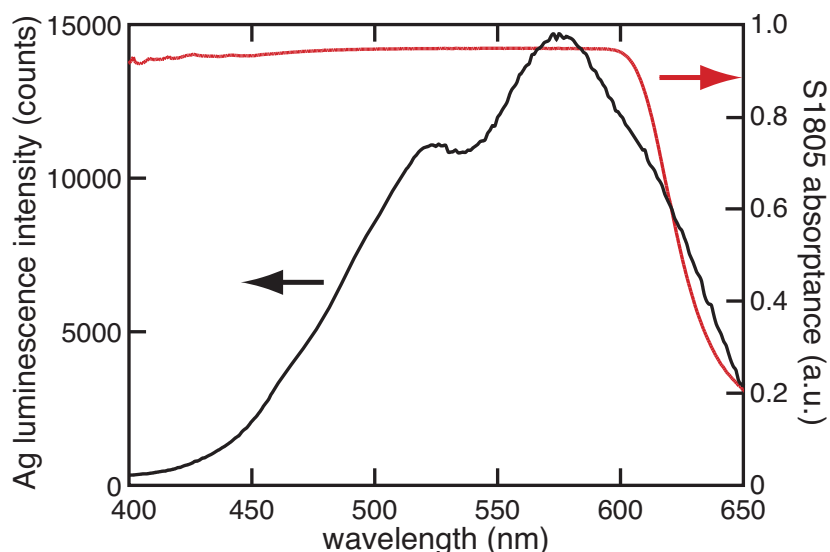


Figure 4.4: Multiphoton induced luminescence spectrum of the silver-coated SERS substrates, and the absorption spectrum of un-exposed Shipley S1805 photoresist. The significant overlap of the two spectra allows us to attribute the resist exposure to the luminescent emission of silver.

length should be chosen to match the femtosecond exposure wavelength. In this work, the femtosecond pulses are centered at 795 nm, with a full width at half maximum of 30 nm. The Raman excitation wavelength of 785 nm is within this bandwidth, allowing excitation of the same hot spots that were isolated by the femtosecond pulses. Figure 4.5 shows the relative overlap of the femtosecond exposure and CW Raman excitation laser spectra.

To confirm the need to match the Raman wavelength to the femtosecond exposure wavelength, we probed the same HSI-processed and unprocessed substrates using 632.8-nm excitation. At 632.8 nm, the maximum HSI improvement over the unprocessed substrate is reduced to a factor of 4. Secondly, the finite resolution of the photoresist influences the HSI performance. The most intense SERS hot spots are often of single or sub-nanometer dimension [65], which is less than the current

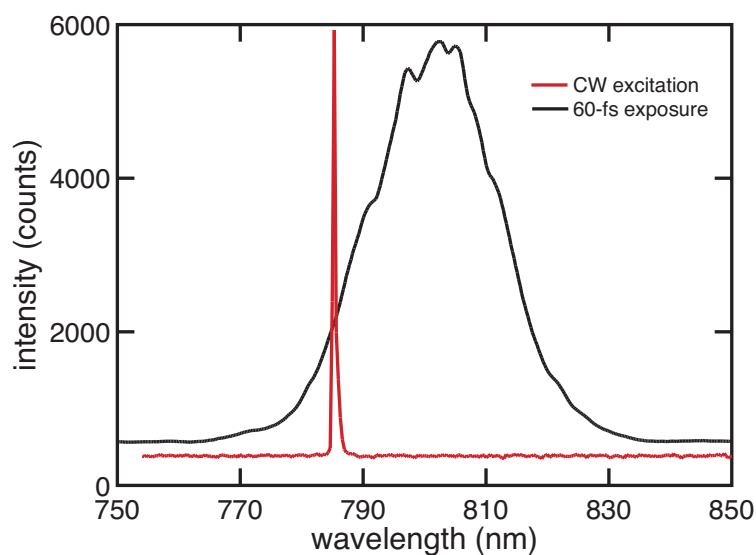


Figure 4.5: Spectra of both the 60-fs exposure laser pulses and the 785-nm continuous wave (CW) Raman excitation laser. The relative overlap of these spectra is critical to the performance of the HSI process.

resolution of most photoresists. This finite resolution causes regions of the surface larger than the hot spots to be exposed during HSI, resulting in analyte adsorption both in and around hot spots. This lack of localization of the analyte adsorption and the range of enhancements associated with different hot spots [33] explain the large variance in the data points in Figure 4.2 at intermediate exposure fluences. Thirdly, the HSI process is useful only for sub-monolayer analyte coverages. Only when there are too few molecules to cover all surface sites on a SERS substrate does the HSI process provide an improvement over an unprocessed substrate. Finally, the thickness of the resist layer covering the surface of the substrate is most likely an important parameter for obtaining the highest improvement factor in this process. If the resist is too thick, higher fluences will be required to expose the resist to its surface. This will result in reduced resolution of the hot spot isolation process, as the multiphoton

induced luminescence is expected to be fairly isotropic [64]. This isotropic emission should cause large areas of the photoresist above the substrate surface to be exposed, resulting in a significant portion of the substrate to become available as adsorption sites after development. A diagram of this expected fluence trend is shown in Figure 4.6.

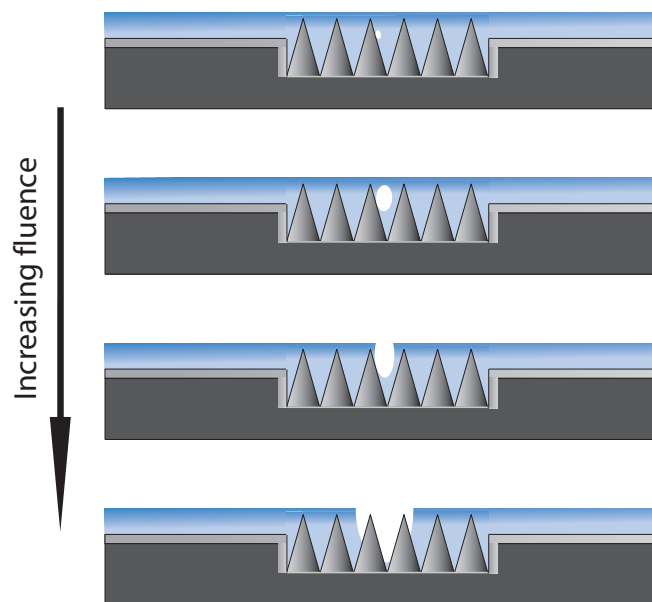


Figure 4.6: Diagram illustrating the effect of increasing femtosecond laser fluence on the region of resist exposed. At a certain point, the exposed region will reach the surface of the resist layer, where it will be removed by the developer. If the fluence is too high, regions of the resist covering areas of the surface besides the hot spots will be exposed and developed away, such that molecules may adsorb to the cold spots on the surface. This will reduce the improvement of the HSI process. Additionally, if the resist layer is too thick, regions of the surface other than the hot spots will likely be exposed after development, due to the near-isotropic nature of the multiphoton-induced luminescence, which is expected to further reduce the improvement of the HSI process.

## 4.6 Conclusion

In conclusion, we have presented a method for physically isolating hot spots on a macroscopic SERS substrate. We have demonstrated its effectiveness using one type of substrate only, but the HSI process can be applied to other metallic SERS substrates as well because most noble metals generate broad multiphoton luminescence [66]. Theoretically, we predict even better hot spot isolation using photoresists with absorption spectra that are confined to the ultraviolet spectral region. Such photoresists would be exposed directly by surface-enhanced multiphoton absorption [67], producing more anisotropic exposure at the hot spots and minimizing the surrounding area that is uncovered during the HSI process. The substrate employed in this work has an optimal excitation wavelength of 632.8 nm, as discussed in Chapter 3, yet we used a 795-nm center wavelength femtosecond exposure laser to perform the hot spot isolation. The enhancement factor of these substrates using 795-nm excitation is approximately 1 order of magnitude smaller than when using 632.8-nm excitation [28, 68]. To optimize the performance of the HSI process using these substrates, the use of a 632.8-nm femtosecond laser would be ideal. However, given the dearth of readily available, high energy femtosecond pulses at 632.8 nm, we were unable to perform this experiment at the current time. The use of an optical parametric amplifier should enable this experiment, and future work in this area should perhaps focus on this type of optimization. Additional studies of hot spot isolation using different resist thicknesses should also elucidate the optimum conditions for this process. Finally, the surface features of the substrate used in this work have very high aspect ratios. Using a more planar SERS substrate, such as those described in [31, 69–71] could be

advantageous for optimizing this process, as the spin-coating step should produce a more uniform layer of photoresist on a planar surface, as compared to a rough surface. Exposure of this uniform resist layer should improve the isolation process, as more hot spots should be uniformly isolated across the substrate at a given exposure laser fluence. Further optimization of the HSI process in this fashion could eventually lead to substrates where every available molecular adsorption site has sufficient enhancement to generate single-molecule SERS.

## **4.7 Acknowledgements**

Eric Diebold and Paul Peng conceived the idea for this work and carried out the experiments described in this chapter. Eric Mazur supervised the research. This research project was supported by DARPA under Contract FA9550-08-1-0285. The authors would also like to thank Ken Crozier for posing the question to which the technique described in this chapter is a potential answer.

# Chapter 5

## Plasmon-enhanced ultrafast laser cell transfection

### 5.1 Abstract

We present a proof-of-concept for transfecting biological cells using plasmon-enhanced ultrafast near-infrared laser pulses. Instead of focusing these laser pulses directly on the lipid membranes of individual biological cells using a high-numerical aperture microscope objective [72, 73], we employ the field enhancement properties of plasmonic nanostructures to generate the requisite optical intensity for producing damage in the cytoplasmic membranes of adherent cells. Plasmonic nano-pyramidal substrates are fabricated over an area greater than  $10 \text{ cm}^2$  by template stripping of gold on KOH-etched silicon wafers, and are used as substrates for cell growth. Using loosely-focused  $\mu\text{J}$ -level femtosecond laser pulses combined with a motorized microscope stage system, we optically perforate the lipid membrane of cells at a rate of

approximately  $10^3 \cdot \text{s}^{-1}$ . Using this technique, we observe loading of human breast carcinoma cells with silence ribonucleic acid (siRNA) molecules. The particular siRNA molecule used in this work is designed to knock down expression of green fluorescent protein (GFP), expressed by these cells. Using image analysis, we observe a spatial anticorrelation of GFP expression and siRNA transfection 24 hours after exposure to plasmon-enhanced femtosecond laser pulses. This technique has potential to serve as a high-throughput, physical method of delivering siRNA or other biomolecules to cells without the use of traditional transfection reagents.

## **5.2 Introduction**

The functional introduction of biomolecules into living biological cells is one of the most widely used techniques in modern cell biology [74]. Known in the cell biology community as “transfection,” the general process of introducing and integrating molecules of DNA (deoxyribonucleic acid) or RNA (ribonucleic acid) into a cell such that they modify its genetic composition or functionality is central to the field of genetic engineering. There have been a variety of techniques developed to accomplish this goal in many different cellular systems, but each is accompanied by specific and unique limitations and drawbacks [75]. Typically, these techniques exhibit a significant tradeoff between the efficiency of biomolecule delivery and either throughput or cell toxicity. While techniques such as cell sorting using flow cytometry have been developed to circumvent the efficiency limitations of modern transfection protocols, improving the overall efficiency of transfection is important for biological applications in which the number of cells available for experiments is small, such as in the case of

embryonic stem cell research.

The first step towards developing a new transfection technique is finding a way for molecules such as DNA and RNA to cross the cell's external phospholipid bilayer membrane. Since healthy cells do not simply endocytose foreign DNA or RNA molecules, something must be done to enable crossing of this barrier. In 1984 [76], an ultraviolet frequency-tripled Nd:YAG laser emitting 5 ns pulses of 355 nm radiation was used to create a sub-micron sized hole in the membrane of cells, such that ambient DNA could enter the cell through diffusion. While this result was very exciting and promising at the time, the thermal stress placed on the cells combined with the potentially harmful ionizing radiation of ultraviolet nanosecond laser pulses prevented this technique from becoming widely applied in biological experiments. However, it did lay the groundwork for other laser-based transfection techniques to be developed. Recently, a similar type of laser transfection technique has been demonstrated using femtosecond lasers [72]. Using multiphoton absorption of near-infrared laser pulses to create sub-micron sized pores in the lipid membrane of mammalian cells, Tirlapur *et al.* transfected chinese hamster ovarian cells with plasmid DNA vectors, causing the cells to express GFP. In the same fashion as [76], the plasmid DNA diffuses into the cytoplasm through these transient pores before they close. This introduction of plasmid DNA into the cell enables incorporation of the DNA vector sequence into the genome after entering the nucleus of the cell (it should be noted that it is not clear at this time how naked DNA plasmids actually cross the nuclear membrane and enter the nucleus). The use of multiphoton (intensity-dependent) absorption acts to confine the damage of the cell's plasma membrane to the focal volume of the high

numerical-aperture microscope objective employed in the work. The use of a femtosecond laser implies that only extremely small amounts of energy are required to generate the intensities required for multiphoton absorption to occur: femtosecond laser pulses reduce the amount of energy deposited in the cell by several orders of magnitude as compared to the case of nanosecond or continuous wave linear (single-photon) absorption [6]. While [72] claimed near 100% efficiency transfection in this system, other reports [73] contend that this technique has a maximum efficiency of approximately  $50\pm 10\%$ , when all cells irradiated by femtosecond laser pulses are accounted for. Regardless of the efficiency debate in the literature, the simplicity and potential widespread applicability of this laser transfection technique has recently given it much interest in the biophotonics community [77–80].

Although femtosecond laser transfection offers the ability to target individual cells for transfection with high spatial resolution, relatively high efficiency, and cell type independence, it can still be classified as a low-throughput transfection technique. In order to transfect individual cells, each must be targeted using a microscope and irradiated individually. In addition, the high-numerical aperture objectives required to generate localized damage in the cell's membrane have a depth of focus of a few microns at most, which imparts very strict focusing requirements on the procedure. Although there have been efforts made to eliminate this focusing requirement by using a non-diffracting Bessel beam to perform transfection [78], the process is still low-throughput compared to traditional transfection techniques, such as electroporation or transfection using lipid-based reagents. To overcome the throughput bottleneck in femtosecond laser transfection, we employ plasmonic nanostructures to replace high

numerical-aperture objective lens focusing. Instead of tightly focusing femtosecond laser pulses on the membranes of individual cells, we focus the pulses on larger areas of a plasmonic substrate which has cells seeded on its surface. The plasmonic substrate acts to focus light to sub-wavelength dimensions confined to the substrate surface, creating the required intensities to generate transient pores in the cell membrane. Ambient molecules such as DNA and RNA can diffuse through these pores before they close, thereby transfecting cells. Although similar experiments have been done using colloidal metallic nanoparticles as a plasmonic nanostructure [81], this approach has a fundamental flaw in that it leaves potentially toxic nanoparticles in and around the cells after the laser exposure. By fabricating large areas of plasmonic substrates and scanning a high average power femtosecond laser beam across the substrate using low numerical aperture focusing, many cells can be transfected in a short period of time, with no side effects due to nanomaterial contamination.

Here, we demonstrate the transfection of human breast carcinoma cells with siRNA molecules. siRNA molecules are double-stranded RNA molecules, which typically are comprised of approximately 20-25 base pairs that, when introduced into a cell, can knock down the expression of a particular gene through the process of RNA interference (RNAi) [82]. Because certain siRNA molecules have complementary nucleotide sequences to the messenger RNA (mRNA) molecules used by the cell to produce proteins, siRNA molecules enable knockdown of specific genes. This process ultimately works as the siRNA molecules degrade specific portions of the messenger RNA used by the cell to produce proteins in translation [83, 84]. By introducing siRNA molecules using plasmon-enhanced femtosecond laser pulses, we demonstrate

the potential use of this technique for high-throughput screening of siRNA molecules for use in gene therapeutics.

## 5.3 Experimental

Plasmonic nanostructures have the unique ability to confine light to subwavelength dimensions, which often results in an enhancement of the local electromagnetic field intensity. For the work presented in this Chapter, we use a derivative of a type of plasmonic substrate that has been developed elsewhere, for use in surface-enhanced Raman scattering [85]. By producing the inverse structure of a pyramidal pit array using template stripping [86], we create an array of gold-coated pyramids, which has desirable properties for localizing the interaction of femtosecond laser pulses with cells for the purpose of transfection.

### 5.3.1 Fabrication of plasmonic substrates for cell transfection

To produce the pyramidal arrays used for the transfection experiments, we rely on the anisotropic etching of silicon using potassium hydroxide. Single crystal (100) silicon wafers are first cleaned in an ultrasonicator using acetone and methanol, and finally rinsed in isopropanol and deionized water. The wafers are spin-coated with a hexamethyldisilazane (HMDS) adhesion promoter, and then Shipley S1805 positive-tone photoresist at 3000 rpm for 45 seconds. The wafers are soft-baked at 105°C for 1 minute, and then loaded into the mask aligner for photolithography. Hard contact photolithography exposure is used, such that a pattern of 2  $\mu\text{m}$  squares is transferred to the wafer. After development with CD-30 photoresist developer, a

35-nm thick layer of chromium is deposited via thermal evaporation at a rate of 0.3 nm/s. Liftoff of the resist is performed in acetone, heated to 50°C, for approximately 1 hour (inspection under an optical microscope is used to confirm successful liftoff). After a final etch in piranha solution (3:1 H<sub>2</sub>SO<sub>4</sub>:H<sub>2</sub>O<sub>2</sub>) to remove any traces of residual photoresist, the native oxide on the silicon is removed by a 30 second etch in 5% hydrofluoric acid. Immediately after rinsing in deionized water, the wafer is immersed for 10 minutes in a 25% w/w aqueous solution of potassium hydroxide, which is constantly stirred and heated to 80°C. KOH preferentially etches the (110) plane of the silicon crystal faster than the other crystal planes of silicon, as it has the most highly corrugated atomic surface of the silicon crystal planes [87]. After the wafer is removed from this solution and rinsed in deionized water, the chromium is removed using a chromium etch (CR-7, Cyantek Corp.), heated to 40°C, for 5 minutes. Pyramidal pits such as those shown in Figure 5.1 are typically observed in an electron microscope after this fabrication procedure.

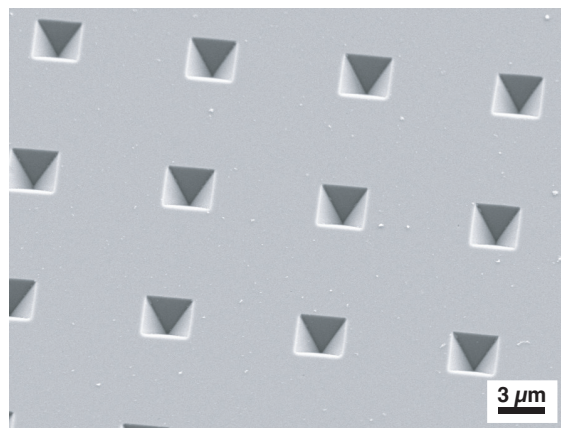


Figure 5.1: Scanning electron micrograph of typical pyramidal pits formed after lithographically-defined etching of silicon using potassium hydroxide. In this sample, the inter-pyramidal pit spacing is 10 μm, and the pit edge length is approximately 2.5 μm.

To fabricate substrates that exhibit plasmonic field enhancement appropriate for cell transfection, we require that the cell membrane be in contact with the region of largest field enhancement. Since the enhancement of these pyramidal pit structures is theoretically predicted by 2-dimensional finite difference time domain (FDTD) simulations to be at their apex [85], we chose to create the inverse structure of these pits. Using this inverse structure, the cells can be in contact with the regions of largest field enhancement during femtosecond laser exposure. By leveraging the low adhesion of gold on the native oxide covering the silicon surface, we employ the technique of template stripping to create gold-coated polymer pyramids [86]. A schematic of the fabrication process is shown in Figure 5.2.

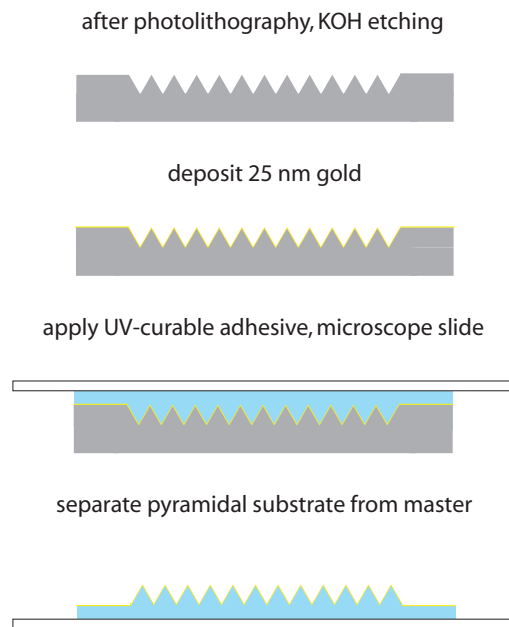


Figure 5.2: Schematic of the template stripping process used to create the inverse structure of the pyramidal pits.

We first evaporate 25 nm of gold onto the pyramidal pit substrate at 0.2 nm/s. By applying a layer of a polyurethane-based UV-curable adhesive (Norland optical

adhesive 73) to the gold coating, we bond a microscope slide to the substrate. After exposure to a 25-W long-wavelength (405 nm) ultraviolet lamp for 1 hour, we carefully separate the microscope slide from the substrate by hand. This results in a gold-coated polymeric pyramidal array, as shown in Figure 5.3.

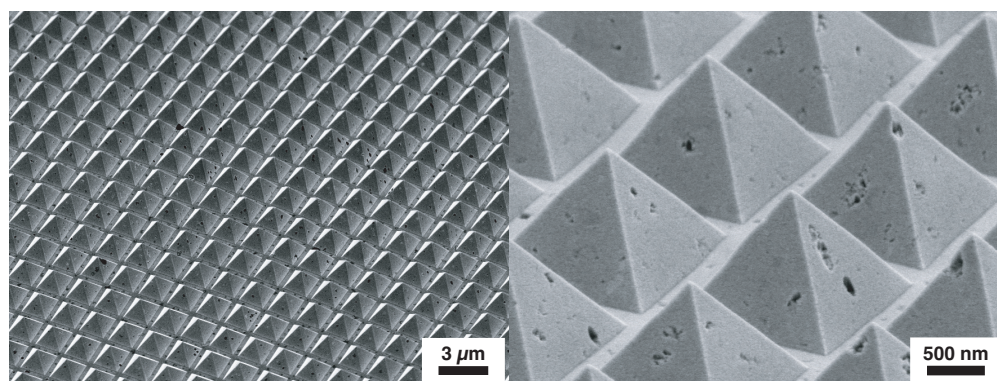


Figure 5.3: Scanning electron micrographs of polymeric pyramids coated with 25 nm of gold, produced by template stripping. The pyramids are spaced by  $2 \mu\text{m}$ , and their edge length is  $1.7 \mu\text{m}$ . The fidelity of replication is excellent, barring a few defects on the sidewalls of the pyramids. The pitch of the pyramids can be controlled via photolithography, but the tip angle is fixed by the crystal structure of silicon.

### 5.3.2 Femtosecond laser system

The femtosecond laser system utilized in these transfection experiments is a RegA 9450 CW-pumped titanium:sapphire regenerative amplifier (Coherent). This system represents a good balance of average power and pulse energy in these experiments, making it nearly ideal for exposing large numbers of cells in a short time period. The seed pulses for this amplifier are provided by a Coherent Mira 900 titanium:sapphire oscillator, operating in femtosecond mode. The RegA is a chirped-pulse-amplification type amplifier, in which femtosecond seed pulses are first stretched in time, amplified, and then re-compressed in time. This system generates 60 fs pulses at a variable repe-

tition rate, from 10 kHz to 250 kHz, with pulse energies up to 10  $\mu\text{J}$ . Pre-compensation of dispersion introduced by optics placed downstream from the output of the amplifier is accomplished by adjusting the external grating compressor. In some cases where lower pulse energies and higher repetition rates are required for transfection, femtosecond pulses from the oscillator are directed through a prism pair for pre-compensation of dispersion introduced by the microscope objective and other optics. The final femtosecond pulsewidth at the sample is minimized by adjusting the compressor while monitoring the intensity of second harmonic generation in a thin (0.5 mm)  $\beta$ -barium borate (BBO) crystal, placed at the focus of the objective lens used in the experiments. A diagram of this system is shown in Figure 5.4.

### 5.3.3 Characterization of plasmonic enhancement of femtosecond laser pulses

Because the resolution of our photolithography system is close to the edge length of these pyramidal structures, we do not have perfect control over the fabrication of these structures. This fact makes it difficult to design a specific size pyramid for operation with our laser wavelength, as these structures are known to exhibit size-dependent plasmon resonances [85]. Ideally, we would simulate the plasmon resonances of specific-sized structures, using numerical finite element or finite difference electromagnetic simulation tools, such that the resonances lie within the bandwidth of our femtosecond laser pulses, and fabricate the designed structures with high resolution. In lieu of this design/simulation/fabrication approach, we can use two photon polymerization to visualize the plasmon-enhanced electric field distribution [64]. Two-

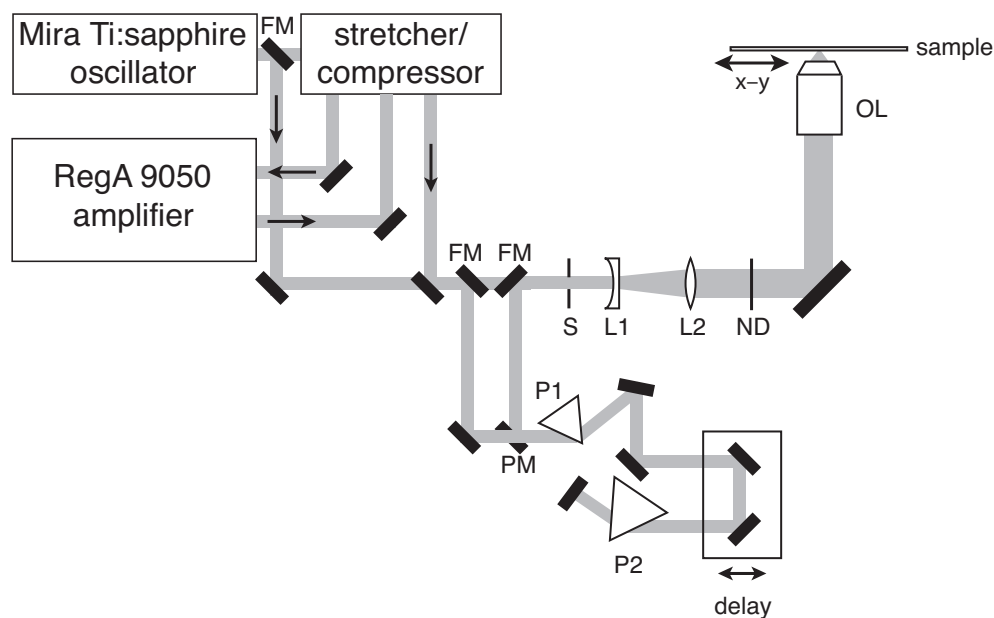


Figure 5.4: Layout of the laser system used to expose cells to plasmon-enhanced femtosecond laser pulses. The system can be used to deliver nano-Joule level ( $\leq 10$  nJ) femtosecond pulses from the oscillator, or micro-Joule level pulses from the amplifier, to the sample. Chromatic dispersion introduced by the lenses and other optics is compensated by either tuning the compressor grating separation (amplifier) or the delay stage in the prism compressor (oscillator). The output of both dispersion-compensation devices is coupled to an inverted microscope (Nikon TE-2000E), which is equipped with a computer-controlled stage. The beam is expanded using a Galilean telescope and attenuated with a neutral density filter before entering the microscope. The distance between the two lenses of the telescope control the spot size of the beam at the sample. (S) mechanical shutter, (L1, L2) lenses comprising the expanding telescope, (ND) neutral density filter, (OL) microscope objective lens, (P1,P2) SF-10 glass prisms, (PM) pickoff mirror, (FM) flip mirror. P2 is significantly ( $2\times$ ) larger in size than P1, in order to account for the width of the spatially dispersed beam at its position.

photon polymerization is an intensity-dependent nonlinear effect [88–90] in which a photoinitiator molecule absorbs two photons “simultaneously” (within the lifetime of an intermediate virtual state) to generate a free radical and induce polymerization of a monomer solution. We use a resin developed by Baldacchini *et al.*, which has been

used for the fabrication of complex three-dimensional structures using two-photon polymerization [89]. This resin consists of 49% ethoxylated trimethylolpropane triacrylate (Sartomer 499), 48% tris(2-hydroxyethyl)isocyanurate triacrylate (Sartomer 368), and 3% acylphosphine oxide radical photoinitiator (Lucirin TPO-L, Ciba), by weight. We mix the three components in the dark for 2 hours before use. Next, we drop-coat the resin onto the gold-coated side of the pyramid array. To induce two-photon polymerization, we illuminate the pyramidal substrate from the UV-curable adhesive side through the microscope slide or coverslip with 800 nm center-wavelength femtosecond pulses from the titanium:sapphire laser oscillator. These pulses are focused on the gold-coated pyramids using a 0.25 NA microscope objective. The sample is scanned back and forth across the focused femtosecond laser pulses, by means of a motorized microscope stage. Due to the fact that the skin depth of gold is approximately 28 nm at an excitation wavelength of 800 nm [91], we expect the enhanced optical fields to “leak through” the gold layer, polymerizing the resin on the other side where the field intensity is largest. Excitation of plasmon modes in the pyramidal structures can further confine the field to their tips [85], preferentially polymerizing the resin. After washing away the unpolymerized resin with ethanol, we observe no polymerization in the area between pyramids; only at the tips of the pyramids where the field is highest do we observe polymerization. An example of this localized polymerization is shown in Figure 5.5.

Other studies [64] of polymerization using plasmon-enhanced two-photon absorption polymerization conclude that polymerization is actually due to the resin’s absorption of single photons generated by multiphoton-induced luminescence of gold,

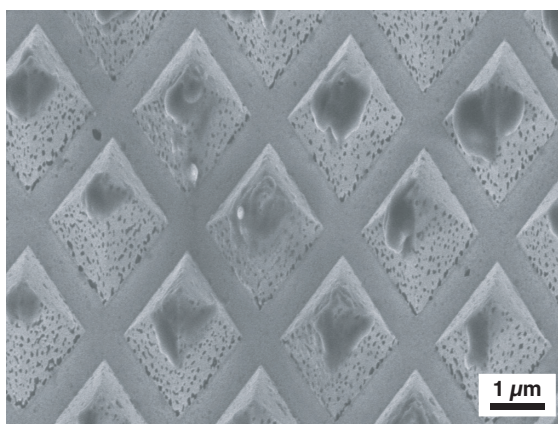


Figure 5.5: Two-photon polymerization of photoinitiator-monomer resin on polymer pyramidal substrate coated with 20 nm of gold. The dark polymer covering the tips of the pyramids is indicative of the spatial distribution of the square of the optical field intensity.

as opposed to direct field-enhanced two photon absorption in the photoinitiator. The former process is likely the case in this experiment as well. However, regardless of the specific cause of polymerization, the result indicates localization of femtosecond laser pulses at the tips of the pyramids, given the intensity-dependent nature of both multiphoton-induced luminescence and direct two-photon polymerization.

### 5.3.4 Cell culture

In this work, human cell lines are used to demonstrate the effectiveness of this transfection technique. Human breast ductal carcinomas transduced to produce GFP (NM2C5 GFP, ATCC) were used in the siRNA experiments, as they are a robust, adherent cell line, which exhibit strong GFP fluorescence. Human thymic epithelial cells (P1.4D6) are used to optimize laser parameters in other experiments, using fluorescent dye molecules. The two cell lines are cultured in Dulbecco's modified eagles medium (DMEM) and Roswell Park Memorial Institute (RPMI) 1640 medium, respectively,

supplemented with 10% fetal bovine serum. 0.25% trypsin with ethylenediaminetetraacetic acid (EDTA) is used to remove the cells from the 75 cm<sup>2</sup> culture flasks for seeding onto the pyramidal substrates. Cells are seeded onto the gold-coated side of the pyramidal substrates 24 hours prior to laser transfection, such that they can adhere to the substrate before laser exposure.

### **5.3.5 Electron microscopy of cells**

The interaction of cells with the pyramidal substrate is imaged using a scanning electron microscope (SEM). We first seed the cells onto the substrate 24 hours before fixation and preparation for imaging in the SEM. Fixation is performed using a 2% paraformaldehyde solution for 15 minutes, followed by a set of dehydration steps in 50%, 70%, 90%, and 100% aqueous solutions of ethanol for 30 minutes each. The substrates are then dried in a CO<sub>2</sub> critical point dryer. Finally, a layer of Pt/Pd is sputtered onto the substrate using 20 mA of current for 30 seconds in an Argon plasma sputter coater. The cells are then imaged at high vacuum in a scanning electron microscope, using a 3-kV accelerating voltage. The best image contrast is obtained from these samples when using the SE2 secondary electron detector. An example image is shown as Figure 5.6 below.

### **5.3.6 Laser parameter optimization**

In order to visualize the effect of plasmon-enhanced femtosecond laser pulses porating the membranes of cells, we used a lipophilic styryl dye (FM1-43, Invitrogen), that fluoresces intensely in the green spectral region when it inserts into the lipid

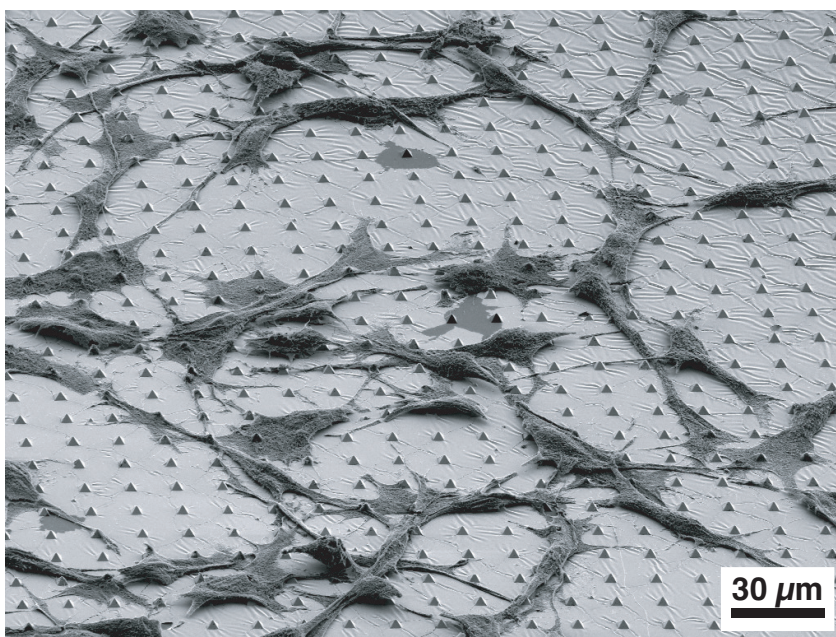


Figure 5.6: Example scanning electron microscope image of human breast carcinoma cells seeded onto a gold-coated pyramidal substrate with  $10\ \mu\text{m}$  pitch. Cell adhesion, spreading, and proliferation on the substrate is indicative of its bio-compatibility.

membranes of cells. This dye has been used to study cell membrane wound healing after nanosecond laser irradiation [92], as it also fluoresces upon entry into the cytoplasm, where it interacts with the membranes of the cell's organelles. An example of this membrane-specific labeling is shown in Figure 5.7.

To perform the laser parameter optimization, we first incubate human thymus epithelial cells in a  $2\ \mu\text{M}$  solution of FM1-43 dye in Hank's balanced salt solution. We then irradiate the cells with femtosecond laser pulses of a variety of repetition rates, focusing conditions, pulse energies, and number of pulses, *through the polymer side* of the pyramidal substrate. This illumination geometry prevents the bulk of the cell from being subjected to the high fields associated with femtosecond laser pulses, such that only the portion of the membrane closest to the gold substrate surface

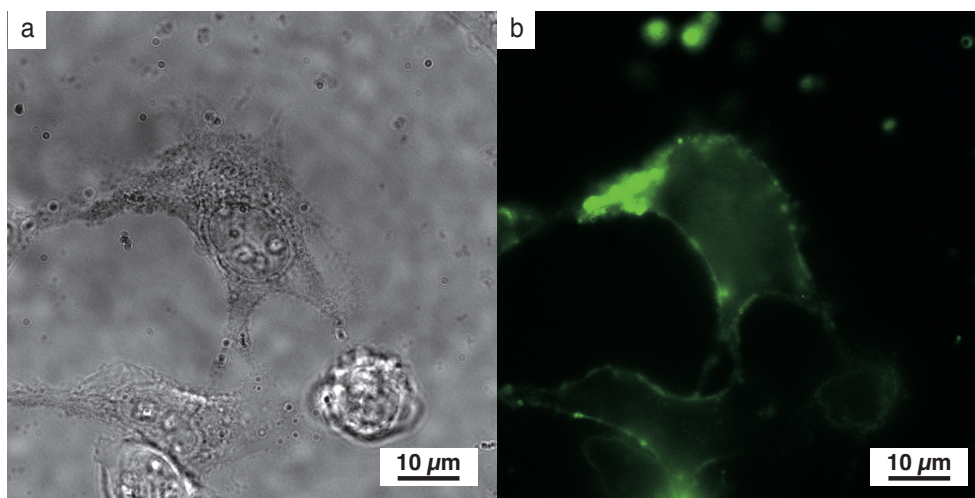


Figure 5.7: (a) Brightfield and (b) green fluorescence images of P1.4D6 human thymus epithelial cells stained with FM1-43. The fact that FM1-43 is membrane impermeable causes only the external side of the cytoplasmic membrane to fluoresce.

will be porated by the plasmon-enhanced laser pulses. By monitoring the FM1-43 fluorescence and viability of the cells after irradiation, we can determine optimal parameters for poration, and later, transfection.

### 5.3.7 Plasmon-enhanced laser cell transfection using siRNA

In order to confirm the introduction of biomolecules into cells and not simply dye molecules, we employ fluorescently-labeled siRNA molecules in our experiments (GFP-22 siRNA-Rhodamine, Qiagen). These specific siRNA molecules are 22 base pairs in length (sense strand sequence GCAAGCUGACCCUGAAGUUCAU, anti-sense strand sequence GAACUUCAGGGUCAGCUUGCCG), and have a tetramethyl rhodamine tag (TRITC) bound to the 3' end of the molecule. This siRNA nucleotide sequence is specific to elicit inhibition of the cell's production of green fluorescent protein (DNA sequence CGGCAAGCTGACCCTGAAGTTCAT) through RNAi. The

rhodamine tag fluoresces in the range of 565 nm, and the cell uptake of these tagged siRNA molecules is imaged in an inverted microscope under 543 nm (green) excitation from either a HeNe laser (laser scanning confocal microscope) or a spectrally-filtered mercury lamp (widefield illumination).

Before exposure to the femtosecond laser pulses, the seeded substrate is placed in a dry petri dish, with no cell culture medium. A 1- $\mu$ M solution of rhodamine-tagged siRNA in culture medium is dispersed on top of the substrate. This petri dish is placed on top of a live-cell microscope incubator stage, held at a constant temperature of 37°C. The heated stage is covered, and a stream of 95% air and 5% CO<sub>2</sub> is flowed into this compartment containing the seeded substrate. After exposure to femtosecond laser pulses focused to a spot size of approximately 30- $\mu$ m diameter (which is larger than the size of the cells in use), we can observe cellular uptake of the rhodamine-labeled siRNA after carefully washing the seeded substrate with fresh medium. The substrates are returned to the incubator, and are left for 24 hours in order to allow the cells to recover. The cells are subsequently imaged in a fluorescence microscope, to determine the effect of the siRNA on gene expression.

## 5.4 Results

### 5.4.1 Laser parameter optimization

To evaluate the effect of a single pyramid on the enhancement of cell membrane poration, we compare the minimum energies required to introduce FM1-43 into a human thymic epithelial cell. Imaging individual cells in a widefield-illumination

fluorescence microscope enables confirmation of poration in the presence of FM1-43. Using a 1.1-NA water-immersion objective lens and 50 ms bursts of an 80-MHz pulse train from a titanium:sapphire femtosecond oscillator, we focus pulses on the pyramidal substrate underneath a single cell. By reducing the average power using a neutral density filter, we can find the minimum pulse energy required to porate a single cell. The typical average power required for poration of a cell using the pyramidal substrate is on the order of 5 mW at the sample. We consider a pore to have formed when, after 30 seconds, the fluorescence intensity of the internal portion of the cell increases to a level significantly higher than that of the surrounding cells which have not been exposed to plasmon-enhanced femtosecond laser pulses. To quantify an enhancement factor of this process, we perform the same experiment on cells seeded onto a flat glass portion of the substrate. Comparing the minimum pulse energy required to generate a pore in the cell membranes, we find that the plasmonic enhancement of the femtosecond laser pulses provides a  $32\times$  reduction of the poration energy threshold.

As a demonstration of the utility of plasmon-enhanced femtosecond laser pulses for cell membrane poration of large numbers of cells, we exposed a large area of a seeded pyramidal substrate by scanning it across a defocused ( $30\ \mu\text{m}$  spot diameter) 250-kHz repetition rate femtosecond pulse train using a computer-controlled motorized microscope stage. As shown in Figure 5.8, cells that have not been exposed to the femtosecond laser pulses (below the dashed line) exhibit weak fluorescence, as their membranes remain intact, and have not taken up any FM1-43. Above the dashed line, where the cells have been exposed to laser pulses, we can see the effect the

pyramidal substrate has on enhancing the intensity of the femtosecond laser pulses. The cells residing on the pyramidal portion of the substrate (upper right) exhibits much brighter fluorescence than the portion of the substrate with no pyramids (upper left).

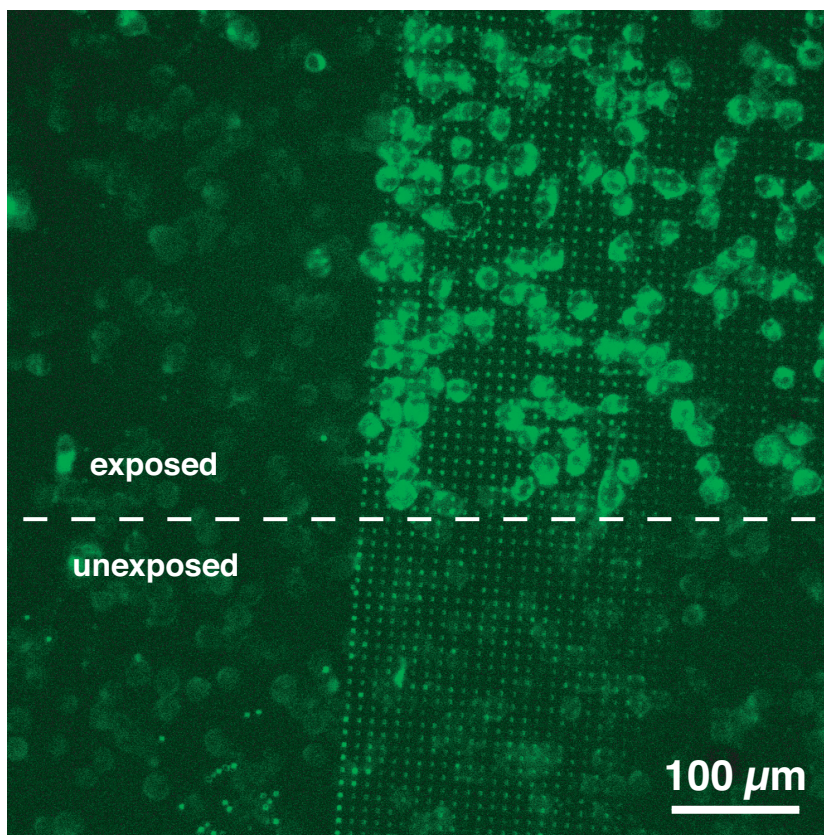


Figure 5.8: Example of human thymic epithelial cells in FM1-43 lipophilic styryl dye 30 seconds after exposure to plasmon-enhanced femtosecond laser pulses. The area above the dashed line was exposed to an average of 1000 pulses, using a spot size diameter of approximately  $30 \mu\text{m}$ . The area below the dashed line shows much weaker fluorescence due to no poration of the cell membrane. The region in the upper left of the exposed region shows similar fluorescence intensity to the unexposed region, indicating that no poration has occurred - this result illustrates the field localization and enhancement effect of the pyramidal substrate.

### 5.4.2 Plasmon-enhanced laser cell transfection using siRNA

An overlaid brightfield and 2-channel fluorescence image of human breast carcinoma cells seeded onto a pyramidal substrate with 10- $\mu\text{m}$  pitch is shown in Figure 5.9.

The region to the left of the dashed line has been exposed to femtosecond laser pulses at a repetition rate of 250 kHz, using a spot size diameter of 30  $\mu\text{m}$ , with an average exposure time of 50 ms per spot. After washing, it is clear that cells in the exposed region have taken up the siRNA labeled with rhodamine (red fluorescence). There is no observable uptake of siRNA in the cells located in the unexposed region. The efficiency of this uptake is approximately 50% (defined as the fraction of all cells who exhibit bright red fluorescence within their cytoplasm within the exposed region).

Examining another portion of the same substrate, shown in Figure 5.10, in which the entire field of view has been exposed to the same laser treatment as in Figure 5.9, we compare the effect of the pyramidal substrate versus a flat region, on the uptake of siRNA. In the lower left corner of Figure 5.10, there is a defect caused by an air bubble in the UV-curable adhesive. After separation from the silicon template, this bubble produced a flat region of polymer (no pyramids present) with no gold coating. Using this region as an example, we can compare the effectiveness of siRNA uptake using a gold pyramidal substrate with that of a flat polymer substrate. Despite the same laser exposure, only the cells on the pyramidal region are observed to uptake the siRNA.

Simply causing cells to uptake siRNA is not sufficient to conclude their transfection. Cells with compromised membranes will also take up siRNA molecules, and

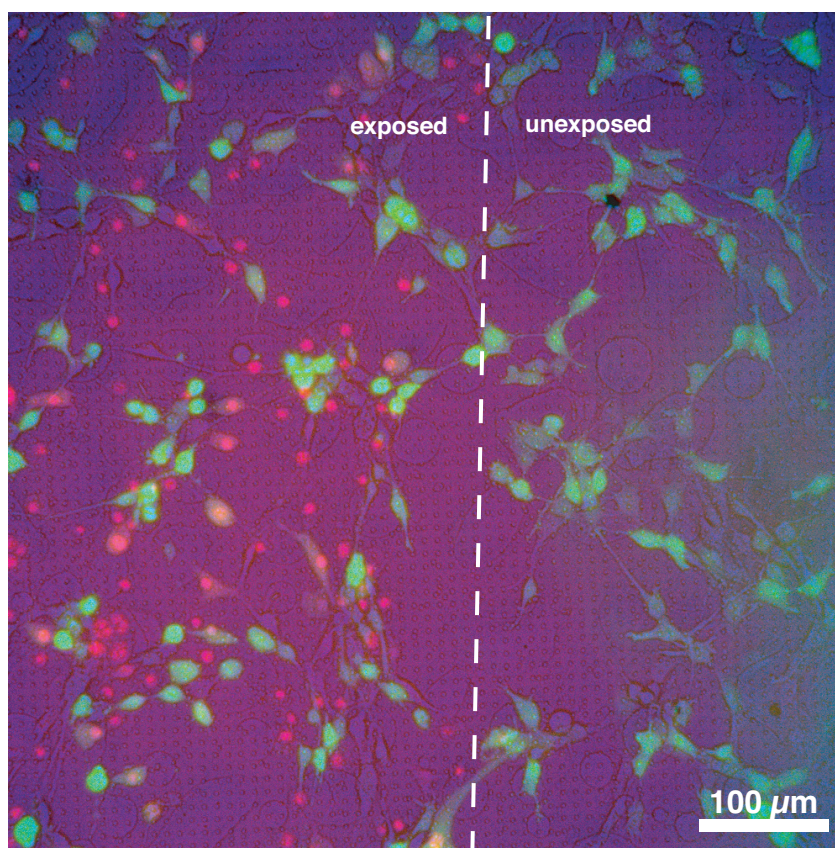


Figure 5.9: Overlaid brightfield and 2-channel fluorescence images of a 10- $\mu\text{m}$  pitch pyramidal substrate seeded with human breast carcinoma cells transduced to produce GFP, exposed to plasmon-enhanced femtosecond laser pulses. The region on the left has been exposed to approximately 1000 laser pulses in the presence of a 1- $\mu\text{M}$  solution of rhodamine-tagged siRNA. After washing with fresh medium, approximately 50% of the cells have taken up appreciable amounts of siRNA.

appear to be healthy, even though they may not be viable. To confirm the viability of cells previously exposed by femtosecond laser pulses, we can observe the fluorescence intensity distribution of cells after several days, when they have had a chance to migrate across the substrate. Figure 5.11 is an image of the same defective portion of the substrate as shown in Figure 5.10, taken 48 hours after laser exposure. Immediately after exposure, there were no cells exhibiting red fluorescence within the boundary of the defect. As shown in Figure 5.11, there clearly are cells that have

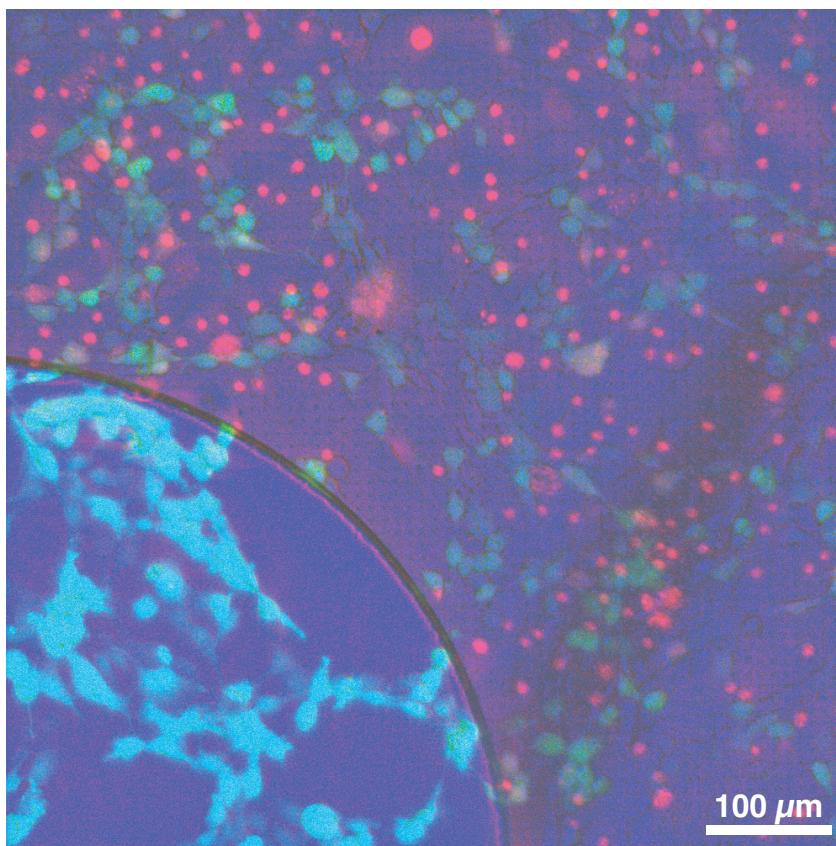


Figure 5.10: Image of a portion of a 10  $\mu\text{m}$  pitch pyramidal substrate near a defect region (lower left), caused by an air bubble in the polymer. The entirety of the region shown in this image was exposed to femtosecond laser pulses in the presence of a 1- $\mu\text{M}$  siRNA solution. Only the cells located on top of the pyramidal portion of the substrate are observed to take up siRNA, indicating the effectiveness of the pyramids at enhancing the laser-plasmon-cell interaction. The brighter green fluorescence in the defect region image is due to the fact that the cells on the pyramidal portion of the substrate are being imaged through a 25-nm thick layer of gold.

taken up siRNA on the pyramidal region, and migrated to the defect region. This migration is indicative of these cells' viability after transfection.

Since the specific siRNA used in these experiments is designed to knock down the expression of GFP in these cells, we must observe a reduction of the GFP expression levels to conclude successful transfection using this technique. Typically, differences

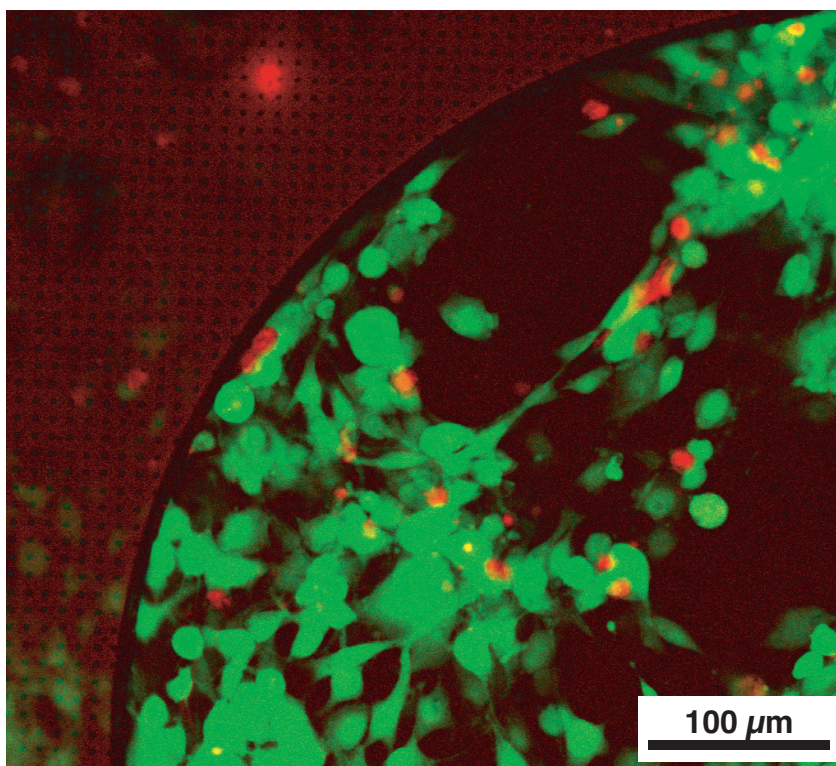


Figure 5.11: Fluorescence image of the same defective region of the substrate shown in Figure 5.10, taken 48 hours after laser exposure.

in average fluorescence intensities across a large population of cells is measured using a fluorescence-activated cell sorting (FACS) system, in which the fluorescence intensity of each individual cell is monitored and recorded. However, this type of measurement typically requires a large number of cells to obtain statistically significant data. Since the microscope-based setup used in these plasmon-enhanced ultrafast laser cell transfection experiments is not well-suited to process a large number of cells, we are not able to make an accurate measurement of the transfection efficiency at this time using a FACS machine. In lieu of this FACS measurement, we analyze a 2-channel fluorescence image to determine the degree of spatial colocalization of red and green fluorescence. By creating a 2-dimensional histogram of the number of pixels with both

red and green fluorescence, we can evaluate the degree to which introduced siRNA molecules are present in cells that still exhibit green fluorescence. Qualitatively, we expect that if rhodamine-labeled siRNA has been introduced to cells, and is causing knockdown of GFP expression, we should observe red, but not green fluorescence from that cell. If the cell has not taken up siRNA, it should fluoresce green, but not red, as GFP will continue to be produced. To perform this analysis, we first acquire a large area, high resolution 2-channel fluorescence image using a confocal laser-scanning microscope with a low-magnification objective (10 $\times$  in this case). Using the colocalization plugin for the software ImageJ [93], we produce a 2-dimensional histogram of the pixel values, indicating the degree of overlap of the green and red pixel intensities. A typical result of this type of image analysis is shown in Figure 5.12.

## 5.5 Discussion

### 5.5.1 Laser parameter optimization

The spatial fluorescence intensity distribution shown in Figure 5.8 confirms that the pyramidal substrate acts to enhance the local optical intensity to levels above the threshold for cell membrane poration. This enables the FM1-43 dye to enter the cytoplasm, causing it to fluoresce more intensely. In a sense, this example of exposing cells on both pyramidal and flat portions of the substrate allows two control experiments to be performed at the same time, as effects due to the laser-plasmon-cell interactions are only observed on the pyramidal portion of the substrate, as

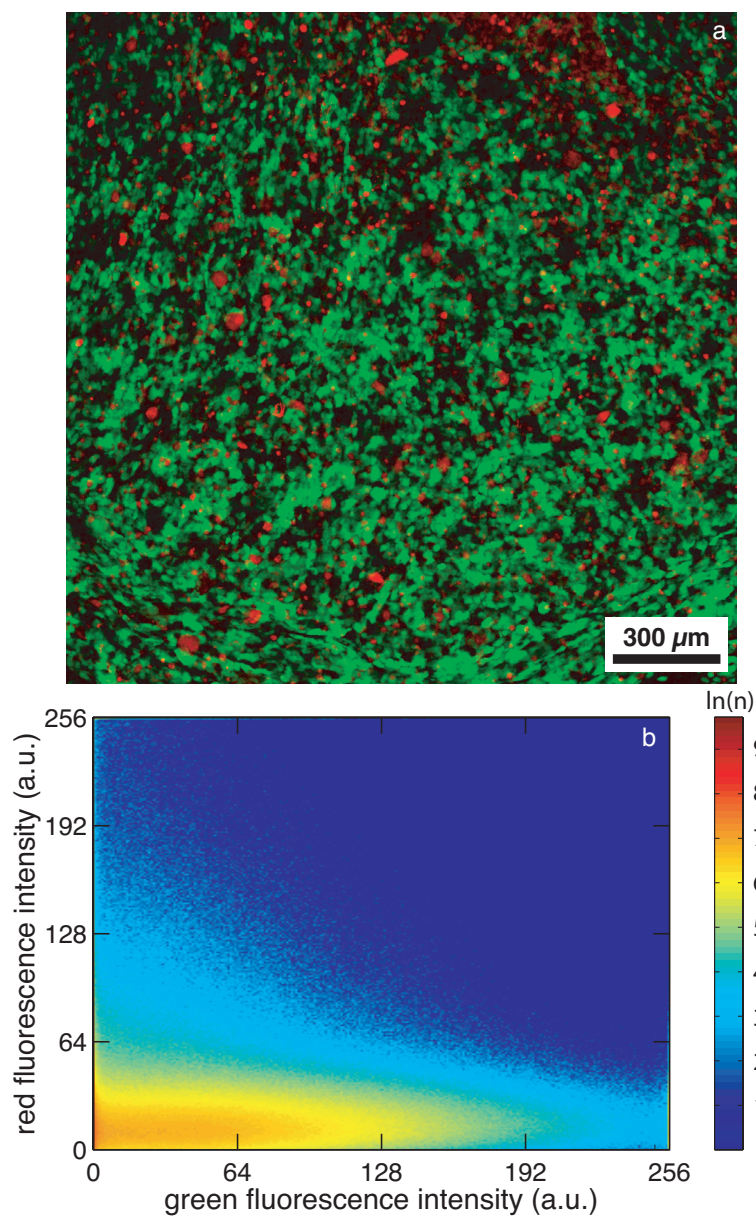


Figure 5.12: (a) 2-channel fluorescence image of human breast carcinoma cells taken 24 hours after exposure to plasmon-enhanced femtosecond laser pulses while in the presence of a 1- $\mu\text{M}$  rhodamine-labeled siRNA solution. (b) 2-dimensional histogram of pixel intensities taken from image in (a). The absence of a large number of pixels in the upper right corner of the histogram and the characteristic “L” shape of the distribution indicates that a very small number of pixels are both intensely red and green, implying a spatial anti-correlation of red and green fluorescence [94].

opposed to simply the laser-cell or pyramid-cell interaction causing any effect. While further increasing the laser intensity will undoubtedly enable poration of the cell membranes of cells on the flat region of the substrate, the fact that this poration is not localized to submicrometer regions will undoubtedly cause cell death. We have verified this fact using femtosecond laser exposure of cells seeded on a flat petri dish in the presence of a fluorescent dye (Lucifer yellow). In this case, the cells' membranes become compromised, and strong cellular uptake of the dye is observed after washing in phosphate buffered saline (data not shown). Approximately 6 hours after exposure of this type, every cell observed to uptake the dye had died. To avoid this result when using the pyramidal substrates, we qualitatively select the appropriate laser intensity by finding the maximum energy at which there is no immediate, observable long-lived ( $> 1$  second) bubble formation or mechanical distortion of the cell upon laser irradiation. All transfection experiments were carried out after performing this type of optimization on a small, test region of the pyramidal substrate.

### 5.5.2 Plasmon-enhanced laser cell transfection using siRNA

Figures 5.8 and 5.10 both indicate the ability of a plasmonic structure to enhance the introduction of molecules into cells using loosely-focused femtosecond laser pulses, as compared to flat regions of either gold or polymer substrates. The efficiency of this introduction is approximately 50%, but larger numbers of cells need to be processed and analyzed quantitatively with a FACS analysis in order to determine this number more accurately. The viability of a small number of cells exposed to plasmon-enhanced femtosecond laser pulses after 48 hours is observed, at least qualitatively,

via cell migration, in Figure 5.11. This indicates that the transfection technique described here has promise as a possible solution for improving the throughput of femtosecond laser cell transfection. Further tests, using either live/dead cell dyes or cell functionality assays, are required to confirm the percentage of transfected, viable cells, to quantify the usefulness of this technique.

The data presented in Figure 5.12 also needs more quantification to fully understand the effectiveness of this transfection procedure on introducing siRNA molecules into cells, such that RNAi results. From the image analysis presented, we find that there is an anti-correlation in the locations of high red and green fluorescence intensities, but the exact values of this anti-correlation are not concluded from the data, given that they change significantly based on the gain settings of the detector used to take the image. A truly quantitative analysis of this data would include a statistical evaluation of fluorescence intensities obtained for each individual cell, as measured by a FACS. Data obtained from samples processed with siRNA should then be compared to those obtained from control samples. Control samples in this case would include cells processed by femtosecond laser pulses on a pyramidal substrate without siRNA, cells unexposed by laser pulses on a pyramidal substrate in the presence of siRNA, and cells processed by femtosecond laser pulses in the presence of a control sequence siRNA (non-specific to any particular gene expression). The differences in GFP expression levels (green fluorescence intensities) across these samples, as measured by FACS, will be able to quantify the effect of plasmon-enhanced femtosecond laser transfection of siRNA into cells. The main difficulty in obtaining this FACS data, as it stands now, is that our experimental setup cannot uniformly expose a

large (approximately 6 cm<sup>2</sup>) substrate to femtosecond laser pulses across the entire area. This would probably require low-numerical aperture focusing optics, combined with either a long-travel 2-dimensional translation stage, or a large working field scan mirror system. Since the range of optical intensities required to generate pores in cells but preserve their viability is fairly small (approximately  $\pm 2\%$ ) for these human breast carcinoma cells, the spot size or average power must not vary by much (less than 2%) across the entire substrate in order to uniformly expose each cell. Factors such as the Rayleigh range of the focusing optics are critically important in this case, as the thickness of the polymer layer in the pyramidal substrate often has non-uniformities which can alter the spot size at the surface where the cells reside. In the case of using a scan mirror system to process the cells, Fresnel losses in the scan lens at high scan angles must be avoided, as well as any focal plane curvature and spot size aberrations.

Another potential way to improve the efficiency of this transfection process would involve optimizing the pitch and geometry of the plasmonic structures that generate the enhanced fields required for localized cell membrane poration. To this point, we have only attempted transfection of cells using pyramidal substrates of 2  $\mu\text{m}$  and 10  $\mu\text{m}$  pitch. This parameter can be varied by simply writing a variety of photolithography masks and fabricating master samples in silicon using the process described in this Chapter. By altering the pitch of the pyramidal substrate relative to the average size of the cell, the area underneath the cell that is in contact with the substrate can be varied. This contact area changes how the cell adheres to the substrate (which influences viability), the ease at which molecules, such as siRNA, can diffuse to regions

near the pyramid-cell contact points, and the total amount of damage that is done to the cell, assuming that equal sized pores form at the tip of each pyramid. All of these factors will contribute to the overall efficiency of the transfection process.

## 5.6 Conclusion

The results obtained from this experiment represent a preliminary step towards proving the feasibility of plasmon-enhanced ultrafast laser cell transfection. We have demonstrated the fabrication of a biologically-compatible plasmonic substrate, that is produced using conventional photolithography, chemical etching, and template stripping. We have demonstrated the field localization feature of this substrate using two-photon polymerization, in which we are able to visualize the regions of largest intensity on the surface after exposure to a femtosecond laser pulses. Utilizing the field localization properties of these pyramidal substrates, we were able to produce transient pores in human thymus epithelial cells with femtosecond laser pulses illuminating a region larger than the entire cell. This is an approach fundamentally different than previous work on femtosecond laser cell transfection [72, 73, 76–79, 95]. This poration was confirmed by observation of entry of a reactive fluorescent dye into the cytoplasm and subsequent observation of cell viability. Using this method to find an acceptable set of laser parameters for cell poration, we were able to introduce siRNA molecules into human breast carcinoma cells with approximately 50% efficiency. While this number represents a reasonable efficiency in comparison with other modern biological techniques [75], the process has not been fully optimized, and higher efficiencies can be expected in the future. The specific siRNA molecules

introduced into these cells is designed to elicit RNAi and knock down the expression of GFP. While we have observed a qualitative spatial anti-correlation of red and green fluorescence in a population of cells processed with this technique, more control experiments must be performed to confirm that this anticorrelation is due to RNAi caused by introduction of a specific siRNA nucleotide sequence. These experiments must be performed in a FACS machine, which will require a large number of cells to be processed with femtosecond laser pulses, in order to sample the fluorescence from enough cells to draw an accurate conclusion.

While we have not yet proven this technique to be useful for *in vitro* biological assays or for clinical use, we have demonstrated that the introduction of biomolecules to living cells is possible on a scale impossible to attain using conventional femtosecond laser cell transfection. With further optimization of the plasmonic substrate and the laser scanning system, it should be possible to transfect cells using femtosecond lasers on an unprecedented scale. While we have demonstrated transfection using siRNA, transfection using DNA should also be possible using this technique. Even though DNA plasmids must cross the cell's nuclear membrane before transfection can occur [73], reports of conventional femtosecond laser transfection using DNA plasmids give hope that plasmon-enhanced femtosecond laser pulses may someday be used on a large scale to transfect arbitrary cell types with biomolecules besides siRNA.

## 5.7 Acknowledgements

We would like to thank Alexander Heisterkamp and Markus Schomaker for helpful discussions and experimental assistance in the beginning stages of this project.

Additionally, we would like to thank Evangelos Gatzogiannis and the Center for Nanoscale Systems at Harvard University for assistance with the cell culture and electron microscopy sample preparation. Finally, we would also like to thank Andrew Koh for providing the P1.4D6 cells and much biology assistance at the beginning of this project.

# Chapter 6

## Conclusions and outlook

In conclusion, we have presented the use of femtosecond laser pulses for several applications which utilize the enhanced optical fields created by plasmonic effects in metallic nanostructures. In this Chapter, we summarize the main results from each of the experimental chapters, and provide suggestions for future research directions for each project.

In Chapter 3, we described the use of the unique surface morphology created by femtosecond laser irradiation of silicon to generate large areas of silicon nanostructures. These surface structures are used as scaffolds for the deposition of silver nanoparticles via thermal evaporation. This nanoparticle formation is a direct result of a silver-silicon dioxide surface energy minimization, aided by surface roughness, which is induced by the fast cooling of the molten silicon after femtosecond laser irradiation. The nanoparticles formed on the surface are well-suited for surface-enhanced Raman scattering, in which molecules adsorbed to these particles experience a large enhancement in their Raman cross section due to the enhanced electric fields and

large polarizabilities associated with surface plasmon excitation. The SERS characteristics of these substrates were measured extensively. A future measurement that needs to be completed is an accurate estimation of the surface area of these substrates. The high aspect ratio of these nanostructures makes them difficult to characterize using physical techniques such as atomic force microscopy, and their structure (silicon covered by silicon dioxide covered by silver) makes them difficult to analyze using electrical (capacitance) measurements. An accurate measurement of the surface area of these substrates will enable us to make a more exact determination of the SERS enhancement factor. Another measurement that ideally would be performed on these substrates is an extension of the excitation profile shown in Figure 3.7 into the visible and infrared ranges of the spectrum. This measurement would require many more laser excitation sources, but such a system, based on either picosecond-pumped optical parametric oscillators or dye lasers and subtractive triple monochromators, has been developed and used in other work for SERS excitation profiling [52, 96, 97]. Using this measurement, we can determine the optimum excitation wavelength for generating the largest enhancement factor from these SERS substrates. However, for potential use in a real-world sensing or analytical application, optimizing the tradeoff between enhancement factor and cost, simplicity and robustness of the laser source will be most practical.

Motivated by recent work [33] which reported a quantitative measurement of the broad distribution of adsorption site enhancement factors on a large-area SERS substrate, we demonstrated a nonlinear optical technique to physically isolate SERS hot spots in Chapter 4. The technique, deemed hot spot isolation (HSI), prevents

molecules from adsorbing to sites of low enhancement on our laser-nanostructured SERS substrate using multiphoton induced exposure of a commercial photoresist. This process leaves a thin layer of resist covering the cold spots on a SERS substrate after removal of the resist covering the hot spots. In this first demonstration of the process, we showed a 27-fold improvement in average SERS enhancement factor compared to an unprocessed substrate. While this process could potentially generate SERS substrates where every available adsorption site has sufficient enhancement to exhibit single molecule SERS, its usefulness is limited to sub-monolayer coverages of molecules. Further, the SERS signals obtained from these HSI substrates have a significant background in the fingerprint region, generated from the resist covering the cold sites. This background is potentially problematic for using this technique in analytical applications. However, due to the relatively broad and featureless nature of the Raman spectrum of the resist, it should be possible to remove this background using post-processing techniques [98]. Another potential issue associated with the layer of undeveloped resist covering much of the substrate surface is the change of resonant frequency associated with each hot spot. Because the undeveloped photoresist has a higher refractive index than that of air, CW excitation (in air) of the same hot spots isolated using the HSI process may not be possible, due to the spatial dispersion of nanoparticle aggregate hot spots with respect to the surrounding refractive index. This mismatch could, however, be rectified by using an index-matching fluid to cover the sample during the Raman measurements, after analyte molecules have adsorbed to the surface. Although this local refractive index change near these hot spots potentially poses a fundamental problem for the HSI process, it is likely that,

on this substrate, the isolation process uncovers entire particle aggregates containing hot spots, leaving more planar areas covered. It is unlikely that the resolution of the hot spot isolation process is sufficient to uncover only the few nanometer-sized hot spots in these particle aggregates, leaving the rest of the aggregate covered with resist. Surface-enhanced multiphoton resist exposure has been shown to exhibit this type of low-resolution behavior in previous work on related nanoparticle aggregate systems [64]. Future research on the HSI process should include testing of its performance on more planar SERS substrates, such that spin-coating of the resist provides more uniform coverage of the surface. Additionally, testing of the refractive index dependence of the SERS signal from HSI-processed substrates will also help to understand which hot spots are isolated.

Finally, in Chapter 5, we presented preliminary results on the high-throughput introduction of molecules into biological cells using plasmon-enhanced femtosecond laser pulses. We described the fabrication of a large-area, bio-compatible plasmonic substrate using photolithography, KOH etching, and template stripping. We verified optical field localization at the pyramidal tips of these substrates using two-photon polymerization excited by illumination through the gold coating. The bio-compatibility of these substrates was confirmed by observation of cell adherence and proliferation over several days. We then verified the introduction of dye molecules into human thymus epithelial cells by creating transient pores in their cytoplasmic membranes using plasmon-enhanced femtosecond laser pulses focused to a spot size larger than the average cell diameter. Using fluorescently-labeled siRNA molecules (designed to knock down cellular expression of GFP), we also confirmed the deliv-

ery of siRNA into the cytoplasm of human breast carcinoma cells which had been transduced to produce GFP. Preliminary statistical analysis of this siRNA delivery experiment yields an efficiency of approximately 50%, measured using a fluorescence microscope. Twenty four hours after siRNA delivery, we observe a spatial anticorrelation of siRNA fluorescence and GFP fluorescence within a population of cells exposed to plasmon-enhanced femtosecond laser pulses. Although this measurement cannot confirm the sequence-specific knock down of gene expression due to RNA interference, it is a promising result nonetheless. Future work on this project should include analysis of a larger population of exposed cells using a FACS machine, such that better statistics on the efficiency of gene knock down can be attained. Control experiments using non-specific siRNA sequences should also be performed, to confirm that RNA interference is responsible for this reduction in green fluorescence intensity. Finally, the system should be optimized, in which a parameter study is done to find the optimal pitch and feature size of the pyramidal substrate, as well as laser shot number and fluence. With this optimization complete, the full potential for *in vitro* use of plasmon-enhanced femtosecond laser transfection can be realized, as the technique combines the best elements of a targeted, physical, high efficiency transfection technique with the high throughput of lower efficiency techniques such as lipid reagent-based transfection and electroporation.

All three of the experiments described in this thesis involve femtosecond laser pulses and metallic nanostructures. The marriage of these two fields has provided a set of tools to generate giant optical field intensities on ultrashort time and nanometer length scales. Using these extreme conditions, we demonstrate physical feats that have

the potential to bring great improvements to the fields of spectroscopy and biology. Only further research in this unique area of physics will enable plasmon-enhanced nonlinear optics to push these fields in new and exciting directions.

# Appendix A

## Soft lithography “replication” of SERS substrates

The following Appendix describes the use of soft lithography to fabricate polymeric replicas of the silicon-based SERS substrates described in Chapter 3 of this thesis.

The laser-nanostructuring process described in Chapter 3 yields excellent SERS substrates, but they are produced at the expense of a relatively long fabrication time (approximately 30 min/cm<sup>2</sup> with a 2.5-W average power, 1-kHz repetition rate titanium:sapphire femtosecond laser system). For mass-production of these laser-nanostructured SERS substrates, a parallel fabrication process must be employed. While scanning several lasers at once is a potential solution to this problem, amplified femtosecond laser systems with high average power are expensive, and currently require significant expertise to operate. We can potentially solve this problem by replicating the “master” substrates that have been fabricated using the laser-nanostructuring process. Since these master substrates are not fabricated using a

photomask, like in conventional photolithography, we must use an alternate method to accurately reproduce copies of the master. Soft lithography has been developed as a viable technique for the accurate replication of many surface structures [99]. Since many of the surface features that comprise these SERS substrates are of nanometer-scale, we require the replication process to have excellent resolution. One such method for reproducing structures of nanometer dimension is to use “hard” polydimethylsiloxane (H-PDMS) to create a negative mold of the surface, and then fill it with another polymer to create a replica of the master.

To replicate the laser-nanostructured silicon substrates, we use the recipe described in the supporting information from Ref. [100] to create the negative mold of the SERS substrate (with no silver deposited). This recipe creates a harder, more brittle layer of polymer than the traditional PDMS recipe (Sylgard 184 silicone elastomer kit, Dow Corning) typically employed in soft lithography. By back-coating the H-PDMS layer with a layer (approximately 3 mm thick) of traditional PDMS, we can separate the H-PDMS layer from the nanostructured silicon master more easily, although it is still somewhat a delicate task. Instead of filling the negative mold with another polymer, such as polyurethane, we have found that using the H-PDMS negative as a substrate for silver deposition actually works best to generate the largest SERS signals. This is likely due to the fact that the H-PDMS has sub-nanometer feature resolution [100], whereas the polyurethane has worse resolution due to its reduced relative hardness. After depositing a SAM of benzenethiol, we obtain SERS signals such as those shown in Figure A.1, using 632.8-nm excitation, and a 0.25 NA objective.

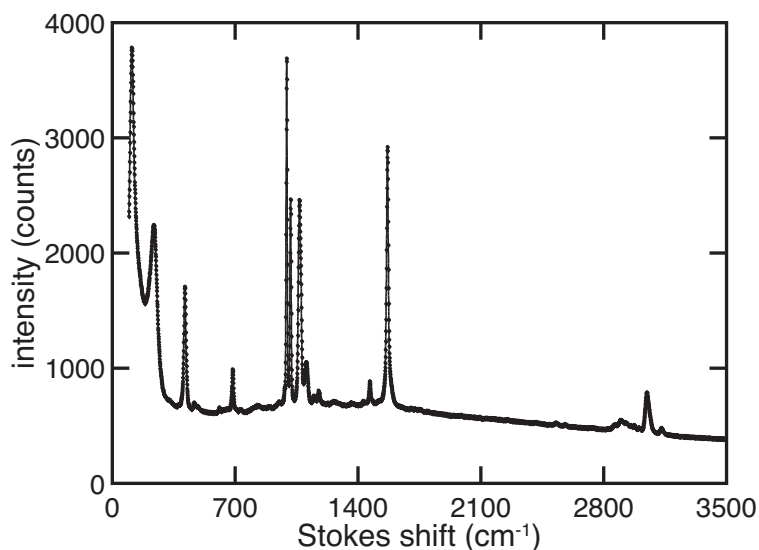


Figure A.1: SERS spectrum taken from a negative mold of a laser-nanostructured silicon wafer, coated with 80 nm of silver, with a SAM of benzenethiol applied. 632.8-nm excitation was used in this case. The enhancement factor is on the order of  $10^6$ , approximately one order of magnitude smaller than the enhancement factor of the original, as measured under the same conditions.

The spectrum is nearly identical to those taken using the original silicon-based SERS substrate, indicating that the H-PDMS adds very little background to the SERS signal. The enhancement factor of the  $1572\text{ cm}^{-1}$  Raman band is approximately  $10^6$ , when normalized to a reference sample of neat benzenethiol. In addition to the large enhancement factor, the H-PDMS-based negative substrate is optically transparent. Experiments illuminating the silver-coated side of the H-PDMS substrate through the transparent polymer and collecting the backscattered light yield a signal only approximately an order of magnitude smaller than front-illuminating the H-PDMS substrate. “Back-illumination” of this type of substrate could be useful in non-invasive spectroscopy applications, where spectroscopy can be performed *through* a transparent physical barrier, into a container, without actually opening the

container. This relatively simple fabrication process, employing soft lithography in combination with laser-nanostructuring, could potentially represent a route to mass production of high performance, inexpensive SERS substrates for use in a variety of new trace detection applications.

# Appendix B

## Custom-built tunable CW titanium:sapphire laser system

A custom-designed and home-built continuous-wave tunable titanium:sapphire laser was used to take Raman spectra in some of the experiments presented in this thesis. The construction of this laser system was based on a mismatched etalon concept, as described in [101], but with several modifications. The main components of this laser were harvested from a KM-Labs titanium:sapphire femtosecond oscillator kit. The pump source is a 5-Watt, 532-nm, frequency doubled, continuous wave Nd:YVO<sub>4</sub> Verdi laser (Coherent, Inc.). As shown in Figure B.1, the layout of the laser is a modified X-cavity, which is almost the same as the original KM-Labs design.

Instead of using a pair of prisms as a dispersion-compensating element, we remove one of the prisms, such that the titanium:sapphire fluorescence is spatially dispersed on the end mirror (M1). Since the end mirror is flat, this spatial dispersion enables feedback and laser oscillation for only a small subset of wavelengths at each angular

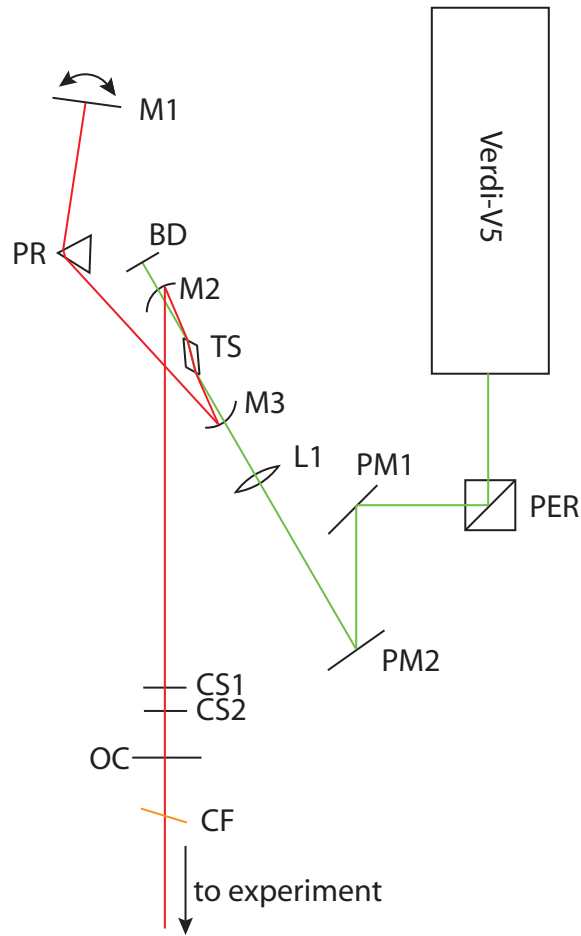


Figure B.1: Cavity layout for the custom-designed tunable CW titanium:sapphire laser used for Raman spectroscopy. (M) Dielectric mirrors (OC) output coupler (PM) pump mirror (PER) periscope (L) lens (TS) titanium:sapphire crystal (BD) beam dump (PR) SF-10 glass prism (CS) microscope coverslip (CF) glass color filter

position. This feedback condition, and thus the lasing wavelength, can be tuned by rotating the end mirror about the vertical axis. The spatial dispersion at the end mirror provided by the single prism alone causes the laser to output fairly narrow laser spectra. However, for the Raman spectroscopy experiments described in Chapters 3 and 4, excitation linewidths less than  $10 \text{ cm}^{-1}$  are required. To further reduce the linewidth of the output, we place two microscope coverslips (CS1, CS2) of different

thicknesses (#0, Gold Seal, and #1, VWR Corp.) near the output coupler, such that the laser mode propagates through them at near-normal incidence. Each coverslip exhibits a set of Fabry-Perot transmission resonances, and due to the coverslip thickness mismatch, these resonances have a different free spectral range. This free spectral range mismatch creates loss in the overall laser cavity at wavelengths besides those where the both transmission resonances overlap. The result is a laser cavity with a mode spacing of approximately 3 nm at a wavelength of 785 nm. The complete tuning range of this laser is approximately 710 nm to 895 nm. The output wavelength is controlled by simply rotating the end mirror about the vertical axis. Adjusting the angle of either of the coverslips fine-tunes the laser wavelength. At a pump power of 5 Watts, this laser is capable of producing more than 700 mW of output at 800 nm, with a linewidth such that the  $520\text{ cm}^{-1}$  Raman band of silicon can be measured at less than  $6\text{ cm}^{-1}$  at room temperature. A glass color filter is placed after the output coupler to absorb stray pump light. To prevent stray fluorescence emitted by the titanium:sapphire crystal from entering the Raman microscope, the beam is dispersed by an external ruled grating, blazed at 770 nm, to spatially disperse the light. The long path length after the grating, combined with a pinhole-based spatial filter, prevents stray fluorescence emission from the laser cavity from entering the microscope.

# References

- [1] T. Maiman, “Stimulated optical radiation in ruby,” *Nature*, vol. 187, no. 4736, pp. 493–494, 1960.
- [2] C. Shank and E. Ippen, “Subpicosecond kilowatt pulses from a mode-locked cw dye laser,” *Applied Physics Letters*, vol. 24, p. 373, 1974.
- [3] A. Zewail, “Femtochemistry,” *The Journal of Physical Chemistry*, vol. 97, no. 48, pp. 12427–12446, 1993.
- [4] P. Saeta, J. Wang, Y. Siegal, N. Bloembergen, and E. Mazur, “Ultrafast electronic disordering during femtosecond laser melting of gaas,” *Physical review letters*, vol. 67, no. 8, pp. 1023–1026, 1991.
- [5] T. Elsaesser, J. Shah, L. Rota, and P. Lugli, “Initial thermalization of photoexcited carriers in gaas studied by femtosecond luminescence spectroscopy,” *Physical review letters*, vol. 66, no. 13, pp. 1757–1760, 1991.
- [6] A. Vogel, J. Noack, G. Huttman, and G. Paltauf, “Mechanisms of femtosecond laser nanosurgery of cells and tissues,” *Applied Physics B: Lasers and Optics*, vol. 81, no. 8, pp. 1015–1047, 2005.
- [7] I. Maxwell, S. Chung, and E. Mazur, “Nanoprocessing of subcellular targets using femtosecond laser pulses,” *Medical Laser Application*, vol. 20, no. 3, pp. 193–200, 2005.
- [8] W. Denk, J. Strickler, and W. Webb, “Two-photon laser scanning fluorescence microscopy,” *Science*, vol. 248, no. 4951, pp. 73–76, 1990.
- [9] E. Ozbay, “Plasmonics: Merging photonics and electronics at nanoscale dimensions,” *Science*, vol. 311, no. 5758, pp. 189–193, 2006.

- 
- [10] W. Barnes, A. Dereux, and T. Ebbesen, "Surface plasmon subwavelength optics," *Nature*, vol. 424, no. 6950, pp. 824–830, 2003.
- [11] J. Jackson, *Classical Electrodynamics*. John Wiley and Sons, Inc., 1998.
- [12] C. Bohren and D. Huffman, "Absorption and scattering of light by small particles," *New York*, 1983.
- [13] N. Ashcroft and N. Mermin, *Solid State Physics*. Saunders College Publishing, 1976.
- [14] C. Raman and K. Krishnan, "A new type of secondary radiation," *Nature*, vol. 121, no. 3048, p. 501, 1928.
- [15] D. Long, *Raman spectroscopy*. McGraw-Hill New York, 1977.
- [16] D. L. Jeanmaire and R. P. Vanduyne, "Surface raman spectroelectrochemistry .1. heterocyclic, aromatic, and aliphatic-amines adsorbed on anodized silver electrode," *Journal of Electroanalytical Chemistry*, vol. 84, no. 1, pp. 1–20, 1977.
- [17] M. Fleischmann, P. Hendra, and A. McQuillan, "Raman spectra of pyridine adsorbed at a silver electrode," *Chemical Physics Letters*, vol. 26, pp. 163–166, 1974.
- [18] H. Metiu, "Surface enhanced spectroscopy," *Progress in Surface Science*, vol. 17, pp. 153–320, 1984.
- [19] K. Kneipp, H. Kneipp, I. Itzkan, R. R. Dasari, and M. S. Feld, "Surface-enhanced raman scattering and biophysics," *Journal of Physics-Condensed Matter*, vol. 14, no. 18, pp. R597–R624, 2002.
- [20] K. Kneipp, H. Kneipp, I. Itzkan, R. R. Dasari, and M. S. Feld, "Ultra-sensitive chemical analysis by raman spectroscopy," *Chemical Reviews*, vol. 99, no. 10, pp. 2957–+, 1999.
- [21] K. Kneipp, Y. Wang, H. Kneipp, L. T. Perelman, I. Itzkan, R. Dasari, and M. S. Feld, "Single molecule detection using surface-enhanced raman scattering (sers)," *Physical Review Letters*, vol. 78, no. 9, pp. 1667–1670, 1997.
- [22] S. M. Nie and S. Emory, "Probing single molecules and single nanoparti-

- cles by surface-enhanced raman scattering,” *Science*, vol. 275, no. 5303, pp. 1102–1106, 1997.
- [23] V. A. Markel, V. M. Shalaev, P. Zhang, W. Huynh, L. Tay, T. L. Haslett, and M. Moskovits, “Near-field optical spectroscopy of individual surface-plasmon modes in colloid clusters,” *Physical Review B*, vol. 59, no. 16, pp. 10903–10909, 1999.
- [24] S. Gresillon, L. Aigouy, A. C. Boccara, J. C. Rivoal, X. Quelin, C. Desmarest, P. Gadenne, V. A. Shubin, A. K. Sarychev, and V. M. Shalaev, “Experimental observation of localized optical excitations in random metal-dielectric films,” *Physical Review Letters*, vol. 82, no. 22, pp. 4520–4523, 1999.
- [25] J. Lombardi, R. Birke, T. Lu, and J. Xu, “Charge-transfer theory of surface enhanced Raman spectroscopy: Herzberg–Teller contributions,” *The Journal of Chemical Physics*, vol. 84, no. 8, p. 4174, 1986.
- [26] R. Loudon, *The quantum theory of light*. Oxford University press, USA, 2000.
- [27] T. Kempa, R. A. Farrer, M. Giersig, and J. T. Fourkas, “Photochemical synthesis and multiphoton luminescence of monodisperse silver nanocrystals,” *Plasmonics*, vol. 1, pp. 45–51, 2006.
- [28] E. D. Diebold, N. H. Mack, S. K. Doom, and E. Mazur, “Femtosecond laser-nanostructured substrates for surface-enhanced raman scattering,” *Langmuir*, vol. 25, no. 3, pp. 1790–1794, 2009.
- [29] M. G. Albrecht and J. A. Creighton, “Anomalously intense raman spectra of pyridine at a silver electrode,” *Journal of the American Chemical Society*, vol. 99, no. 15, pp. 5215–5217, 1977.
- [30] R. P. Van Duyne, J. C. Hulteen, and D. A. Treichel, “Atomic-force microscopy and surface-enhanced raman-spectroscopy .1. ag island films and ag film over polymer nanosphere surfaces supported on glass,” *Journal of Chemical Physics*, vol. 99, no. 3, pp. 2101–2115, 1993.
- [31] R. G. Freeman, K. C. Grabar, K. J. Allison, R. M. Bright, J. A. Davis, A. P. Guthrie, M. B. Hommer, M. A. Jackson, P. C. Smith, D. G. Walter, and M. J. Natan, “Self-assembled metal colloid monolayers - an approach to sers substrates,” *Science*, vol. 267, no. 5204, pp. 1629–1632,

- 1995.
- [32] A. Campion and P. Kambhampati, "Surface-enhanced raman scattering," *Chemical Society Reviews*, vol. 27, no. 4, pp. 241–250, 1998.
- [33] Y. Fang, N. H. Seong, and D. D. Dlott, "Measurement of the distribution of site enhancements in surface-enhanced raman scattering," *Science*, vol. 321, no. 5887, pp. 388–392, 2008.
- [34] S. Chan, S. Kwon, T. W. Koo, L. P. Lee, and A. A. Berlin, "Surface-enhanced raman scattering of small molecules from silver-coated silicon nanopores," *Advanced Materials*, vol. 15, no. 19, pp. 1595–+, 2003.
- [35] S. N. Sharma, R. K. Sharma, G. Bhagavannarayana, S. B. Samanta, K. N. Sood, and S. T. Lakshmikumar, "Demonstration of the formation of porous silicon films with superior mechanical properties, morphology and stability," *Materials Letters*, vol. 60, no. 9-10, pp. 1166–1169, 2006.
- [36] M. Y. Shen, C. H. Crouch, J. E. Carey, and E. Mazur, "Femtosecond laser-induced formation of submicrometer spikes on silicon in water," *Applied Physics Letters*, vol. 85, no. 23, pp. 5694–5696, 2004.
- [37] T. H. Joo, M. S. Kim, and K. Kim, "Surface-enhanced raman-scattering of benzenethiol in silver sol," *Journal of Raman Spectroscopy*, vol. 18, no. 1, pp. 57–60, 1987.
- [38] D. Hulin, M. Combescot, J. Bok, A. Migus, J. Vinet, and A. Antonetti, "Energy transfer during silicon irradiation by femtosecond laser pulse," *Physical Review Letters*, vol. 52, no. 22, pp. 1998–2001, 1984.
- [39] J. Goldman and J. Prybyla, "Ultrafast dynamics of laser-excited electron distributions in silicon," *Physical Review Letters*, vol. 72, no. 9, pp. 1364–1367, 1994.
- [40] J. Goldman and J. Prybyla, "Ultrafast hot-electron dynamics in silicon," *Semiconductor Science and Technology*, vol. 9, pp. 694–696, 1994.
- [41] E. Palik and G. Ghosh, *Handbook of optical constants of solids*. Academic press, 1985.
- [42] M. Winkler, *Non-Equilibrium Chalcogen Concentrations in Silicon: Physical Structure, Electronic Transport, and Photovoltaic Potential*.

- PhD thesis, Harvard University, Cambridge, MA, 2009.
- [43] D. Lide, ed., *CRC handbook of chemistry and physics*. CRC press, 1993.
- [44] L. Landau and E. Lifshitz, *Hydrodynamics*. Nauka, Moscow, 1988.
- [45] M. Y. Shen, C. H. Crouch, J. E. Carey, R. Younkin, E. Mazur, M. Sheehy, and C. M. Friend, "Formation of regular arrays of silicon microspikes by femtosecond laser irradiation through a mask," *Applied Physics Letters*, vol. 82, no. 11, pp. 1715–1717, 2003.
- [46] C. H. Crouch, J. E. Carey, J. M. Warrender, M. J. Aziz, E. Mazur, and F. Y. Genin, "Comparison of structure and properties of femtosecond and nanosecond laser-structured silicon," *Applied Physics Letters*, vol. 84, no. 11, pp. 1850–1852, 2004.
- [47] D. L. Smith, *Thin-film deposition: principles and practice*. New York: McGraw-Hill, 1995.
- [48] A. M. Michaels, J. Jiang, and L. Brus, "Ag nanocrystal junctions as the site for surface-enhanced raman scattering of single rhodamine 6g molecules," *Journal of Physical Chemistry B*, vol. 104, no. 50, pp. 11965–11971, 2000.
- [49] C. H. Munro, W. E. Smith, M. Garner, J. Clarkson, and P. C. White, "Characterization of the surface of a citrate-reduced colloid optimized for use as a substrate for surface-enhanced resonance raman-scattering," *Langmuir*, vol. 11, no. 10, pp. 3712–3720, 1995.
- [50] M. Kerker, O. Siiman, and D. S. Wang, "Effect of aggregates on extinction and surface-enhanced raman-scattering spectra of colloidal silver," *Journal of Physical Chemistry*, vol. 88, no. 15, pp. 3168–3170, 1984.
- [51] J. G. Bergman, D. S. Chemla, P. F. Liao, A. M. Glass, A. Pinczuk, R. M. Hart, and D. H. Olson, "Relationship between surface-enhanced raman scattering and the dielectric properties of aggregated silver films," *Optics Letters*, vol. 6, no. 1, pp. 33–35, 1981.
- [52] A. D. McFarland, M. A. Young, J. A. Dieringer, and R. P. Van Duyne, "Wavelength-scanned surface-enhanced raman excitation spectroscopy," *Journal of Physical Chemistry B*, vol. 109, no. 22, pp. 11279–11285, 2005.

- [53] B. Tull, J. E. Carey, E. Mazur, and S. Yalisove, "Surface morphologies of silicon surfaces after femtosecond laser irradiation," *Materials Research Society Bulletin*, vol. 31, pp. 626–633, 2006.
- [54] E. C. L. Ru, E. Blackie, M. Meyer, and P. G. Etchegoin, "Surface enhanced raman scattering enhancement factors: a comprehensive study," *Journal of Physical Chemistry C*, vol. 111, no. 37, pp. 13794–13803, 2007.
- [55] W. B. Cai, B. Ren, X. Q. Li, C. X. She, F. M. Liu, X. W. Cai, and Z. Q. Tian, "Investigation of surface-enhanced raman scattering from platinum electrodes using a confocal raman microscope: dependence of surface roughening pretreatment," *Surface Science*, vol. 406, no. 1-3, pp. 9–22, 1998.
- [56] B. Saleh and M. Teich, *Fundamentals of Photonics*. Wiley, 2007.
- [57] K. Kneipp, Y. Wang, H. Kneipp, I. Itzkan, R. R. Dasari, and M. S. Feld, "Population pumping of excited vibrational states by spontaneous surface-enhanced raman scattering," *Physical Review Letters*, vol. 76, no. 14, pp. 2444–2447, 1996.
- [58] J. A. Venables, G. D. T. Spiller, and M. Hanbucken, "Nucleation and growth of thin-films," *Reports on Progress in Physics*, vol. 47, no. 4, pp. 399–459, 1984.
- [59] S. Yoshida, Yamaguchi, T., and A. Kinbara, "Optical properties of aggregated silver films," *Journal of the Optical Society of America*, vol. 61, no. 1, 1971.
- [60] N. Felidj, J. Aubard, G. Levi, J. R. Krenn, A. Hohenau, G. Schider, A. Leitner, and F. R. Aussenegg, "Optimized surface-enhanced raman scattering on gold nanoparticle arrays," *Applied Physics Letters*, vol. 82, no. 18, pp. 3095–3097, 2003.
- [61] U. Kreibig and L. Genzel, "Optical-absorption of small metallic particles," *Surface Science*, vol. 156, no. JUN, pp. 678–700, 1985.
- [62] C. D. Bain, E. B. Troughton, Y. T. Tao, J. Evall, G. M. Whitesides, and R. G. Nuzzo, "Formation of monolayer films by the spontaneous assembly of organic thiols from solution onto gold," *Journal of the American Chemical Society*, vol. 111, no. 1, pp. 321–335, 1989.

- [63] E. D. Diebold, P. Peng, and E. Mazur, "Isolating surface-enhanced raman scattering hot spots using multiphoton lithography," *Journal of the American Chemical Society*, vol. 131, no. 45, pp. 16356–16357, 2009.
- [64] S. Nah, L. J. Li, and J. T. Fourkas, "Field-enhanced phenomena of gold nanoparticles," *Journal of Physical Chemistry A*, vol. 113, no. 16, pp. 4416–4422, 2009.
- [65] J. P. Camden, J. A. Dieringer, Y. M. Wang, D. J. Masiello, L. D. Marks, G. C. Schatz, and R. P. Van Duyne, "Probing the structure of single-molecule surface-enhanced raman scattering hot spots," *Journal of the American Chemical Society*, vol. 130, no. 38, pp. 12616–12617, 2008.
- [66] G. T. Boyd, Z. H. Yu, and Y. R. Shen, "Photoinduced luminescence from the noble-metals and its enhancement on roughened surfaces," *Physical Review B*, vol. 33, no. 12, pp. 7923–7936, 1986.
- [67] A. Sundaramurthy, P. J. Schuck, N. R. Conley, D. P. Fromm, G. S. Kino, and W. E. Moerner, "Toward nanometer-scale optical photolithography: Utilizing the near-field of bowtie optical nanoantennas," *Nano Letters*, vol. 6, no. 3, pp. 355–360, 2006.
- [68] R. L. Aggarwal, L. W. Farrar, E. D. Diebold, and D. L. Polla, "Measurement of the absolute raman scattering cross section of the 1584-cm(-1) band of benzenethiol and the surface-enhanced raman scattering cross section enhancement factor for femtosecond laser-nanostructured substrates," *Journal of Raman Spectroscopy*, vol. 40, no. 9, pp. 1331–1333, 2009.
- [69] C. L. Haynes and R. P. Van Duyne, "Nanosphere lithography: A versatile nanofabrication tool for studies of size-dependent nanoparticle optics," *Journal of Physical Chemistry B*, vol. 105, no. 24, pp. 5599–5611, 2001.
- [70] R. Van Duyne, J. Hulteen, and D. Treichel, "Atomic force microscopy and surface-enhanced raman spectroscopy. i. ag island films and ag film over polymer nanosphere surfaces supported on glass," *The Journal of Chemical Physics*, vol. 99, no. 3, p. 2101, 1993.
- [71] D. Weitz, S. Garoff, and T. Gramila, "Excitation spectra of surface-enhanced raman scattering on silver-island films," *Optics Letters*, vol. 7, no. 4, pp. 168–170, 1982.

- [72] U. K. Tirlapur and K. König, “Cell biology - targeted transfection by femtosecond laser,” *Nature*, vol. 418, no. 6895, pp. 290–291, 2002.
- [73] D. Stevenson, B. Agate, X. Tsampoula, P. Fischer, C. Brown, W. Sibbett, A. Riches, F. Gunn-Moore, and K. Dholakia, “Femtosecond optical transfection of cells: viability and efficiency,” *Optics Express*, vol. 14, no. 16, pp. 7125–7133, 2006.
- [74] L. Bonetta, “The inside scoop-evaluating gene delivery methods,” *Nature Methods*, vol. 2, no. 11, pp. 875–883, 2005.
- [75] D. Luo and W. Saltzman, “Synthetic dna delivery systems,” *Nature Biotechnology*, vol. 18, pp. 33–37, 2000.
- [76] M. Tsukakoshi, S. Kurata, Y. Nomiya, Y. Ikawa, and T. Kasuya, “A novel method of dna transfection by laser microbeam cell surgery,” *Applied Physics B: Lasers and Optics*, vol. 35, no. 3, pp. 135–140, 1984.
- [77] C. Brown, D. Stevenson, X. Tsampoula, C. McDougall, A. Lagatsky, W. Sibbett, F. Gunn-Moore, and K. Dholakia, “Enhanced operation of femtosecond lasers and applications in cell transfection,” *Journal of Biophotonics*, vol. 1, no. 3, 2008.
- [78] X. Tsampoula, V. Garcés-Chávez, M. Comrie, D. Stevenson, B. Agate, C. Brown, F. Gunn-Moore, and K. Dholakia, “Femtosecond cellular transfection using a nondiffracting light beam,” *Applied Physics Letters*, vol. 91, p. 053902, 2007.
- [79] X. Tsampoula, K. Taguchi, T. Čižmár, V. Garces-Chavez, N. Ma, S. Mohanty, K. Mohanty, F. Gunn-Moore, and K. Dholakia, “Fibre based cellular transfection,” *Optics Express*, vol. 16, no. 21, pp. 17007–17013, 2008.
- [80] A. Uchugonova, K. König, R. Bueckle, A. Isemann, and G. Tempea, “Targeted transfection of stem cells with sub-20 femtosecond laser pulses,” *Optics Express*, vol. 16, no. 13, pp. 9357–9364, 2008.
- [81] M. Schomaker, J. Baumgart, A. Ngezahayo, J. Bullerdiel, I. Nolte, H. Escobar, H. Lubatschowski, and A. Heisterkamp, “Plasmonic perforation of living cells using ultrashort laser pulses and gold nanoparticles,” in *Proceedings of SPIE*, vol. 7192, p. 71920U, 2009.

- [82] A. Fire, S. Xu, M. Montgomery, S. Kostas, S. Driver, and C. Mello, "Potent and specific genetic interference by double-stranded rna in *caenorhabditis elegans*," *Nature*, vol. 391, no. 6669, pp. 806–811, 1998.
- [83] S. Elbashir, J. Harborth, W. Lendeckel, A. Yalcin, K. Weber, and T. Tuschl, "Duplexes of 21-nucleotide rnas mediate rna interference in cultured mammalian cells," *Nature*, vol. 411, no. 6836, pp. 494–498, 2001.
- [84] P. Ahlquist, "Rna-dependent rna polymerases, viruses, and rna silencing," *Science*, vol. 296, no. 5571, p. 1270, 2002.
- [85] N. M. B. Perney, J. J. Baumberg, M. E. Zoorob, M. D. B. Charlton, S. Mahnkopf, and C. M. Netti, "Tuning localized plasmons in nanostructured substrates for surface-enhanced raman scattering," *Optics Express*, vol. 14, no. 2, pp. 847–857, 2006.
- [86] P. Nagpal, N. Lindquist, S. Oh, and D. Norris, "Ultrasmooth patterned metals for plasmonics and metamaterials," *Science*, vol. 325, no. 5940, p. 594, 2009.
- [87] K. Bean, "Anisotropic etching of silicon," *IEEE Transactions on Electron Devices*, vol. 25, no. 10, pp. 1185–1193, 1978.
- [88] S. Kawata, H. Sun, T. Tanaka, and K. Takada, "Finer features for functional microdevices," *Nature*, vol. 412, no. 6848, pp. 697–698, 2001.
- [89] T. Baldacchini, C. LaFratta, R. Farrer, M. Teich, B. Saleh, M. Naughton, and J. Fourkas, "Acrylic-based resin with favorable properties for three-dimensional two-photon polymerization," *Journal of Applied Physics*, vol. 95, p. 6072, 2004.
- [90] L. Li and J. Fourkas, "Multiphoton polymerization," *Materials Today*, vol. 10, no. 6, pp. 30–37, 2007.
- [91] E. Palik and G. Ghosh, *Handbook of optical constants of solids*. Academic press, 1985.
- [92] P. McNeil and T. Kirchhausen, "An emergency response team for membrane repair," *Nature Reviews Molecular Cell Biology*, vol. 6, no. 6, pp. 499–505, 2005.

- [93] "<http://rsbweb.nih.gov/ij/>."
- [94] S. Bolte and F. Cordelieres, "A guided tour into subcellular colocalization analysis in light microscopy," *Journal of microscopy*, vol. 224, no. 3, pp. 213–232, 2006.
- [95] A. Uchugonova, K. K. "onig, R. Bueckle, A. Iseemann, and G. Tempea, "Targeted transfection of stem cells with sub-20 femtosecond laser pulses," *Optics Express*, vol. 16, no. 13, pp. 9357–9364, 2008.
- [96] J. Dieringer, K. Wustholz, D. Masiello, J. Camden, S. Kleinman, G. Schatz, and R. Van Duyne, "Surface-enhanced raman excitation spectroscopy of a single rhodamine 6g molecule," *J. Am. Chem. Soc.*, vol. 131, no. 2, pp. 849–854, 2009.
- [97] C. Allen, G. Schatz, and R. Van Duyne, "Tunable laser excitation profile of surface enhanced raman scattering from pyridine adsorbed on a copper electrode surface," *Chemical Physics Letters*, vol. 75, no. 2, pp. 201–205, 1980.
- [98] C. Lieber and A. Mahadevan-Jansen, "Automated method for subtraction of fluorescence from biological raman spectra," *Applied Spectroscopy*, vol. 57, no. 11, pp. 1363–1367, 2003.
- [99] Y. Xia and G. M. Whitesides, "Replica molding with a polysiloxane mold provides this patterned microstructure," *Angew Chem Int Ed Engl*, vol. 37, pp. 550–575, 1998.
- [100] Q. Xu, B. Mayers, M. Lahav, D. Vezenov, and G. Whitesides, "Approaching zero: using fractured crystals in metrology for replica molding," *J. Am. Chem. Soc.*, vol. 127, no. 3, pp. 854–855, 2005.
- [101] C. Zimmermann, V. Vuletic, A. Hemmerich, L. Ricci, and T. Hansch, "Design for a compact tunable Ti: sapphire laser," *Optics Letters*, vol. 20, no. 3, pp. 297–299, 1995.